Unconventional Nanomanufacturing on a Substrate

Dissertation

zur Erlangung des akademischen Grades

Doktor der Ingenieurwissenschaften

(Dr.- Ing.)

der Technischen Fakultät

der Christian- Albrechts- Universität zu Kiel

Mady Elbahri

Kiel

2007

1. Gutachter Prof. Dr. Rainer Adelung

2. Gutachter Prof. Dr. Volker Abetz

3. Gutachter Prof. Dr. Andrei Kolmakov

Datum der mündlichen Prüfung 07.01.2007

I dedicate this thesis to the memories of my parents.

Philosophy of Science:

" Observing of an effect, seeking to explain the concept that is entwined with, and making use of it, is simply science"

Preface

Nanostructured materials may be defined as those materials whose structural elements (clusters, crystallites or molecules) have dimensions in the 1- to 100-nm range. The explosion in both academic and industrial interest in these materials over the past decade arises from the remarkable variations in fundamental electrical, optical and magnetic properties that occur as one progresses from an 'infinitely extended' solid to a particle of material consisting of a countable number of atoms.

Nanoscience and nanotechnology cover many different areas, but one key set of methods for both concerns nanofabrication. There is a growing interest specifically in manufacturing methods allowing more efficient processes, minimising energy usage/cost and simplifying up-scaling requirements.

In the drive for device miniaturization, considerable research is presently directed towards fabricating one-dimensional (1D) nanostructures, especially nanowires or nanorods, which is considered a second hot topic in physics in recent years (1).

"Nanofabrication" of 1D structures is mainly established either by top-down approach (a bulk material is reduced in size to nanoscale pattern: lithography), bottom-up approach (larger structures are built or grown atom by atom or molecule by molecule: self-assembly), or a combined top-down/bottom-up approach (templated self-assembly) that often uses top-down strategies to fabricate components that direct the bottom-up assembly of the particles (2).

Microelectronic devices and information technology have improved and will continue to improve as a result of large-scale, commercial implementation of nanofabrication. The motivation for these improvements is to increase the density of components, lower their cost, and increase their performance per device and per integrated circuit. But conventional techniques (lithography, printing) have a relatively high cost or low throughput or both; they are also largely restricted to a planar fabrication on very special and clean semiconductor materials and are incompatible with many problems in non-standard fabrication (e.g., fabrication on polymer substrates, large areas, and low-cost fabrication). Conventional microfabrication techniques also expose substrates to corrosive agents or high-energy radiation. The limitation of these conventional approaches is the principal motivation behind exploration and development of new "Nonlithography" nanofabrication techniques (3).

Self-assembly/organization techniques for nanofabrication provide simple methods for research communities in a broad range of disciplines to investigate nanoscience and nanotechnology. Their variety, low cost, operational simplicity, and broad collective applicability open the door to surveying and developing many areas for future applications. These techniques for nanofabrication are being widely accepted and developed in this investigative spirit and are thus a key part of nanoscale research and development, especially for green technology.

Self-organization routes to nanofabrication are often followed in research; they may also offer alternatives to photolithography in manufacturing in the future. Self-organization is omnipresent and vitally important but in fabrication mostly limited to 2D-3D structures where 1D-horizontal (lateral) structures of wires, rings and dots arrays is rare (4). However, self-organization of nanowires is achievable by using a template.

In the framework of this thesis some novel processes of nanomanufacturing are established that are based on self-organization, with and without templates to from a large scale of 1D-horizontal nanostructures like wires and rings directly onto a substrate in a simple and cost-effective manner. The examination of these processes deals with the identification and control of the relevant growth and ordering parameters. This examination is done during the formation of ordered structures as well as after the growth process, so that the formed structures do not get distorted.

This thesis is divided into four sections:

- Section 1 introduces the state of art of the fabrication of 1D nanostructures by means of self-organization.
- Section 2, Fracture Approach, shows a novel templated self-organization approach where thin film fracture is employed as a mould for guiding the self-organization of sputtered material to form nanowires.
- Section 3, Drop Approach, concerns an unconventional self-organization approach using a drop on hot plate. The building block is utilized by direct chemistry on the surface (localized chemistry) and the patterning is stimulated by external force like capillary and/or hydrodynamic instability.
- Section 4 provides a general conclusion and outlook that combines both the Fracture and Drop Approaches from Sections 2 and 3, respectively.

Three appendices are presented at the end of this thesis. Appendix A includes the theory behind the experimental equipment used here, which is, sputtering and evaporation, atomic force microscopy (AFM), scanning electron microscopy (SEM), optical microscopy, UV/VIS spectroscopy, X-rays diffraction (XRD) and spin coating. Appendix B includes the publications and patents of the author that were written in the context of this thesis. Appendix C includes the references.

Table of Content

1 State-of-the-Art in Nanowires Fabrication based on Guided Self Assembly

Human activity is versatile and concerned with different fields, like learning, watching TV, eating, and researching, among others. Building things and manipulating materials at different length scales can be considered as one of the most important activities for human beings. Building things could be enfolded in two broad categories, things achieved with the help of a guiding hand and others without the help of any guiding i.e., self-assembly.

Self-assembly is a concept that has existed since the beginning of life. It is the autonomous organization of components into patterns of structures without human intervention (5,6).

Nanoscale self-assembly is an old concept in science. Phase separation in block copolymers (7,8), noncovalent syntheses (9,10) and micelle formation (11) are of central importance in self-assembly. However, it is only recently that its potential for gaining better control on material fabrication has been realized.

Moving beyond observation, scientists are now interested in making exciting advances in nanotechnology based on the creation of materials, devices and systems through the control of matter at the atomic level. By understanding and controlling the way molecules organize into nanoscale patterns, scientists are discovering new phenomena and learning to design materials with vastly different sets of properties. A new “art” of guiding self-assembly, i.e. self-organization, was developed. Hence, self-assembly is an assembly process in which only the constituents of the final structure take part; that is, get incorporated into the resulting structure, also known as “formation”. Self-organization, in summary, is defined as a mechanism for building patterns, processes, and structures at a higher level through multiple interactions among the components at the lower levels, where the components interact through local rules that do not explicitly code for the pattern. The collective interaction between system components under external driving forces, e.g., capillary, electrostatic, optical, and fluidic shear drive the system far from equilibrium, resulting in the self-organization of its constituents. This type of self-assembly represents the core part of building things in nanometer range, i.e. nanoscience and technology.

Based on guiding self-assembly, an overwhelming amount of fabrication methods for the formation of nanocluster arrangements on surfaces are found. A special issue on these methods has been recently published (12).

The fabrication of such structures may be discussed in terms of two processing steps (independent of the actual process sequence). At first, nanocomponents have to be formed which can be done in various ways from precursors in the liquid, solid, or gas phase employing either chemical or physical

deposition processes. In the second step, the challenge is to organize the segregated and deposited nanoparticles into structures or patterns on a surface.

Thanks to their unique photonic, electronic, magnetic and catalytic properties, zero dimensional (0D) nanoparticles have been attending an active research area for many decades. The largest activity in this field at this time has been in the synthesis of nanoparticles with different sizes and new shapes (13a-c). Readers can refer to several reviews (14 a-f) to obtain further information about the syntheses of nanoparticles.

Our interest here aims at the second step of the fabrication, i.e. organization. As previously mentioned, self-organization of atoms, molecules or even nanoparticles as the building units is vitally important but limited in the kind of structures it can make.

Nanoparticulate thin films based on self-organization have become routine in the last decade by use of methods such as Langmuir-Boldgett transfer techniques (15) that are producing assemblies of monolayer or layer-by-layer (16). Readers interested in these topics can refer to several reviews (17,18). Also, recently, electric (19) and magnetic fields (20) as well as shear forces (21) and solvent evaporation (22) of passivated NP at the water/air interface have been used to direct the assembly of the thin film.

1D-based self-organization is limited to seeding based growth of vertical wires by vapor deposition or by wet chemistry. Vapor phase synthesis techniques, especially Vapor-Liquid-Solid (VLS) growth, are probably one of the most extensively used and studied methods for the formation of 1D semiconductor nanostructures such as whiskers, nanorods and nanowires (23). In a typical process, nanosized catalyst particles (seed) are formed on a substrate. Vapor species are first generated by evaporation, chemical reduction and gaseous reaction. These species are transported and condensed onto the surface of the catalyst placed in a zone with a temperature lower than that of the source material. With proper control over the supersaturation factor (eutectic alloy), one can obtain 1D nanostructure in large quantities. Reader can refer to a recent extensive review (24).

In contrast to high temperature processes, wet chemical deposition routes have recently attracted more attention because of the interest in developing low-temperature, large-scale production of nanostructured ZnO rods onto substrates. ZnO growth onto substrates was initiated by L. Vayssieres during his PhD (25). Leading the way is the two-step solution-based route, where an initial seed layer of ZnO nanocrystals is first formed on the substrate. This can be done in many ways, for example beginning with ZnO nanoparticles dispersed in water or by the hydrolysis of a very low concentration zinc acetate solution. The seeded substrate is then introduced into fresh solution. Upon thermal decomposition in solution phase, vertically aligned ZnO nanowires are synthesized. A review that is highlighting the recent advances in the field is also available (26).

The essential growth in semiconductors has encouraged other groups to pursue solution-phase synthesis of metallic wires in solution (27). For the growth of lead nanorods and nanowires, an inexpensive solvent, ethylene glycol, when heated, also acts as a reducing agent while polyvinylpyrrolidone (PVP) prevents aggregation and guides anisotropic growth.

The limitations of the solution method are: a) long time duration, b) restriction to some special material, c) transfer onto substrate, and d) difficulty in obtaining horizontal wire.

However, recently, a new technique for assembly of nanocomponents based on drop evaporation has received a large interest. One of the novel and interesting 1D structures is a " Ring", which, being often only quasi-1D, also provides a transition to 2D.

It is well known that during the drying process of a coffee droplet on a solid substrate, a ring-like deposit remains along the perimeter. These rings are manifestly macroscopic and formed at the pinned contact line of evaporating droplets. Three conditions are necessary for ring formation in an evaporating drop: pre-existing particles, contact line pinning, and the evaporation at the edge of the droplet. Drop evaporation was used to form quasi-1D as well as 2D structures (28). In contrast to this multi-step approach occurs at RT, our group has very recently utilised an all-in-one approach where the nanoparticle synthesis and organization in wires or rings that occurs simultaneously on a hot plate (29). Structuring-based drop evaporation will be discussed thoroughly in Section 3.

As mentioned above, self-organization leading to horizontal 1D nanostructure is seldom reported. Nevertheless, nanowire-based self-organization is achievable by using a template. Soft template approaches have become especially important. One potential application of DNA nanotechnology is the use of self-assembled DNA lattices to scaffold assembly of nanoelectronic components, especially metallic nanoparticles. Au (30,31), Ag (32,33), Pt (34), and Pd (35) can be precisely positioned periodically on the self-assembled DNA array. The use of biomolecular templates for fabrication of metal nanowires has been recently reviewed (36).

Linear polyelectrolyte in solution can also provide a scaffold for the adsorption of metal ions with opposite charges. Thereafter, the ions can be transformed to 1D assembly by reduction reactions (37).

Electrospinning is an elegant process to fabricate 1D-composites via solution route (38,39,40). The process involves the addition of a metal salt precursor to the polymer solution, where the solution is subsequently electrospinned and the resulting composite is subjected to an additional step of either thermal, chemical or radiolytic (UV and microwave irradiation) reduction process to transform the incorporated metal salt to metal in the fiber nanocomposite. Linear pores and channels inside polymers, alumina and silicate are also used as templates to make 1D assemblies (41, and references therein).

Surfactant molecules have been found to spontaneously organize in 1D structure, i.e. rods, when their concentration reaches a critical value (42). These structures are exploited as a soft template for the production of Au nanorods with different aspect ratios (43,44).

Indeed, templated self-organization of horizontal nanostructures often uses top-down strategies to fabricate components that direct the bottom-up assembly of the particles. Lithography templates have been used to direct the assembly of building blocks, which is done by chemical means, into different configurations (45,46). Furthermore, building blocks prepared by sputtering means have been used to decorate a V-groove etched on a silicon substrate to form 1D metal (47) and semiconductor (48) arrays. Assembly of metallic building blocks have also been initiated at the edge of lattice-plane terraces by chemical and electrochemical reduction of the corresponding metal ions (49, references therein).

In general, it appears to be the tendency that the higher the degree of self-organization, the more special are the materials and the less freedom is in the choice of materials. In order to overcome these limitations, a strategy to form a mould on a wide variety of material for the direct assembly of the building blocks using thin film fractures as a template is proposed (50). Ordered parallel arrays as well as side-by-side nanowires can be easily fabricated (51). Thin film cracks follow strain fields and can be controlled in width, length, and density; therefore, they are considered to be ideal templates for nanowire deposition (52). This part also is discussed thoroughly in the next chapter.

2 Nanowires using the Fracture Approach

2.1 Introduction

Structuring photoresist on surfaces in a fast parallel process on the nanoscale, below 100 nm, is nowadays a standard process in microelectronic device fabrication. This conventional process is routinely used as template for the fabrication of nanowires. But even with this big progress in the "top down" approach there are still significant open tasks remaining in surface structuring on the nanoscale. Optical lithography is used for the fabrication of submicron structures and reaches because of diffraction limits a feature sizes on the order of~200 nm. Current semiconductor nanofabrication photolithography can pattern 37 nm wide features with 193 nm wavelength light. The microelectronics industry plans to pattern even smaller features below 37 nm using photolithography (53).

Another potential route to features with sub-50 nm resolution using 193 nm light is “immersion lithography” (54,55). Imaging resolution for immersion microscopy is improved by increasing the refractive index of the medium between the imaging lens and the imaging plane thus improving the depth of focus and also allowing lenses with larger numerical aperture to be used. Changing the immersion medium from air (n = 1) to water (n =1.47 at 193 nm) allows a lens systems to be designed with numerical apertures approaching 1.3, thus significantly improving the imaging resolution (56). However the technical challenges of contacting the photoresist-coated substrate and mask with water (or another solvent) must be solved before immersion lithography can be implemented.

To pattern smaller features, photolithography will require further advances, such as decreasing the imaging wavelength to 157 nm (57,58). Further decrease can be obtained by using soft X-rays (13.5 nm) known in the microelectronics industry as extreme ultraviolet (EUV) light (59,60). However, the shift to shorter wavelengths of light requires new photoresists to alter the wavelength sensitivity and resolution of the resist (61,62) as well as new light sources and, especially, new types of optics based on reflection rather than transmission to focus the light (63,64).

Electron beam lithography (EBL) (65,66) and X-ray Lithography (XRL) (67) are considered as the leading nanotechnologies for suboptical (~10–200 nm) fabrication. XRL has parallel processing capabilities that permit simultaneous fabrication of large numbers of nanostructures. Even though, resolution in this case is limited by the photoelectron range and diffraction effects to 20 – 50 nm. Moreover, EBL has outstanding resolution yielding features of 1–2 nm in the most favourable cases, but its serial processing format limits its throughputs.

Other technique such as scanning tunneling microscope (STM) has received considerable attention for nanolithography (68) since it can image and manipulate matter on the atomic scale (69). In analogue to EBL the application of STM lithography, is also limited by serial processing speeds.

Additionally the microelectronic approach is typically limited to silicon and requires extreme investments. Consequently relatively simple and cost-effective nanopattering processes have been developed to address these inherent limitations.

Molding and embossing are examples of this processes which are widely used for nanofabrication. There are a number of molding and embossing techniques that can pattern nanometer features over large areas. These techniques have been used to pattern functional structures for inorganic- and organic-based microelectronics and optics (70). The formation of these structures requires a high-resolution master, typically generated by lithography.

Molding techniques, which are also known as soft lithography, are characterized by casting a liquid polymer precursor against a topographically patterned master (71). A number of elastomer polymers could be used for molding. The most widely implemented and successful elastomer for nanofabrication is polydimethylsiloxane (PDMS) (72,73). Other elastomers tested as pattern transfer elements include polyurethane (PU), polyimide, and cross-linked Novolac resins (a phenol formaldehyde polymer) (74).

Embossing techniques, also known as Nanoimprint lithography (75), refer to the pressure- induced transfer of a topographic pattern from a rigid mold (typically silicon) into a thermoplastic polymer film heated above its glass-transition temperature. For instance, to transfer the pattern from a mold onto a thin polymer film of PMMA requires heating the polymer film above 110 °C.

However, nanofabrication by using molding and embossing is primarily limited by several factors like: the tendency of the system to trap bubbles of gas, the ability of a material to mold with high accuracy (76), the distortion of features in the transferred pattern, and the ability of the molded material to fill the mold completely.

Nanosphere lithography (77,78) represents another simple approach, which is also used in nanopattering. However, the approach is only applicable to a certain geometries and also limited to special sort of materials.

In summary finding an approach that works with many different materials in a cost effective, time conserved manner and allowing the structures to be aligned down to the nanoscale in a different geometry is still a challenge.

Cracks have a bad reputation due to the fact that they occur during mechanical failure of materials. Additionally destructive phenomena, like fracture or delamination, are well known in material science since a long time, too. Predictions are made under which circumstances and where failures occur and how to avoid them mainly; the negative consequences of these effects are described and nowadays well characterized in thin film technology (79,80).

“Dry mud” is found to be the most characteristic crack pattern in thin films (81).The patterns formed by a network of cracks tend to look very similar regardless of the scale; from the crack network of the basalt lava flows that form the Giant's Causeway in Ireland to the crazing of glazes on pottery or even to Namib desert texture shown in Figure 1.

Figure 1: Dry mud Namib desert textures.

Moreover, the appearance of the pattern does not depend on the area of the film. This suggests two things: firstly, the same basic mechanism is responsible for all the cases of cracking whatever the scale and secondly, that the appearance of the crack network does not depend on the number of cracks present in it. A physical mechanism that has these characteristics is said to display statistical self-similarity.

On the other hand, Cracks are a hierarchical phenomenon and found in nature in a wide variety of scales even in a nanoscale. Furthermore fracture is a well adjustable phenomena, prediction to align cracks is also possible, e.g., by introducing predetermined breaking points. Figure 2 illustrates just three possibilities to control fracture. Although, applying stress on a film in the form of a bow tie, a crack will form in the middle at its weakest point as seen in Figure 2b.

A variation in the thickness of the thin film leads to points or lines where stress concentrates and results in a fracture of the material. Figure 2c illustrates this. The thickness gradient in the film can be realized during the deposition by the use of a shadow mask. Additionally, there is freedom to choose the material, cracks can occur in wide range of material combinations. Therefore they form an ideal template for nanowires by shrinking the structures down to the nanometer size and offering a non restricted and cost effective way for designing a template on the nanoscale.

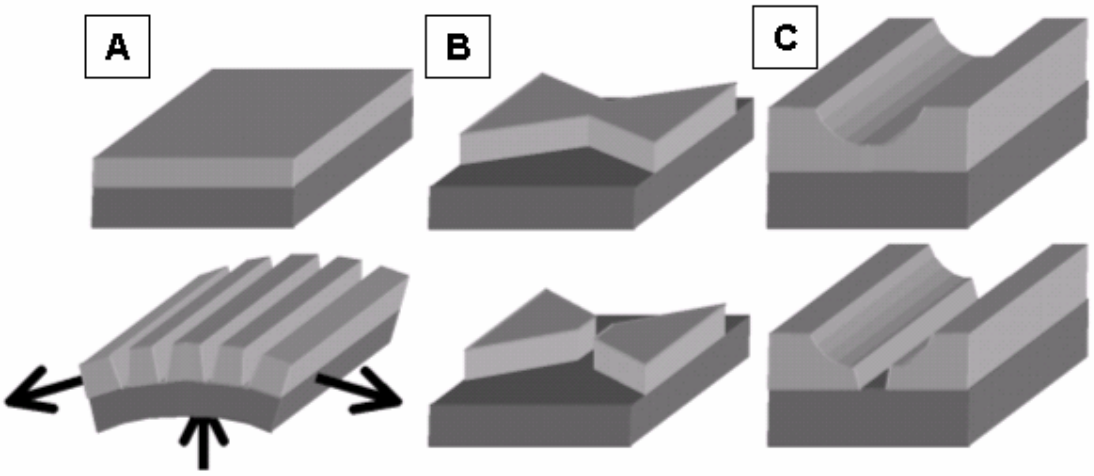

Figure 2: Sketch showing some possibilities to align cracks as nanowire templates, first row shows the film before the application of stress, the last row shows crack structures as a result of applied stress: A) A uniform thin film can be used to create parallel cracks by uniaxial stress. B) A film in the form of a bow tie will crack in the middle at its weakest point. C) A film of variable thickness tents to crack at the weakest point, here found at the middle of the channel.

2.2 Basic Aspect of Brittle Fracture

2.2.1 Origin of Brittle Fracture

The fracture behavior of brittle thin films on substrates differs from the bulk due to the small film thickness and the presence of the substrate. In contrast to the bulk where a propagating crack of a critical length leads to fracture and total failure, a cracked thin film may still remain bonded to the substrate. If a brittle film is under tension a possible failure mode is film cracking. The cracks elongate laterally in the film until they meet the film edge or another crack. The lateral crack length can be many times the film thickness. This kind of crack is called a channel crack. Since the film may have many pre-existing flows under a large stress, many channel cracks can form. This leads to multiple crack formation since a single crack reduces the stress in the film only locally as result of the constraining effect of the substrate.

The elastic energy reduction associated with the crack advancing per unit area is known to be the crack driving force. The crack resistance is the energy needed to advance the crack per unit area. A crack cannot grow when the driving force is below the resistance and continuous to grow when the driving force is equal to the resistance. The three locations of the crack resistance that is in the film, in the substrate, and on the interface have different values. The crack resistance also depends on the crack velocity and on the environment.

Generally, channel cracks can be explained by the well known Griffith model (82). In this model the crack does not penetrate into the substrate and the fracture stress, σ, normal to the crack plane is given by:

$$\sigma^2 = 2E\,\gamma/h \tag{2.1}$$

Where, E is Young's modulus and γ is the surface energy and h is the crack length, Note that in the equations, the poison ratio, ν, which is defined as the ratio of the contraction strain normal to the applied load divided by the extension strain in the direction of the applied load, is neglected, since its omission will not significantly affect the discussion.

Rearrangement the terms in the above equation, the critical energy for fracture is therefore,

$$U_c = \sigma^2 h / E = 2\gamma \tag{2.2}$$

The right hand defines the surface energy for film fracture, where two new surfaces are formed which is directly related to the stored elastic energy in the film. Further, for cracks as shown in Figure 3, where the crack reaches the substrate, it is intuitively plausible that, h is the film thickness, S. Substituting S for h in eq. (3.2) yields

$$U = \sigma^2 S / E \geq U_c \tag{2.3}$$

Equation (3.3) demonstrates the criterion $U \geq U_c$ for film fracture to occur. Moreover, there is, then, for U, when σ is constant and independent of S, a critical film thickness Sc at which U exceeds U_c and S_c is given by the following equation:

$$S_c = 2E\,\gamma/\,\sigma^2 \tag{2.4}$$

Film fracture will occur when $S \geq Sc$.

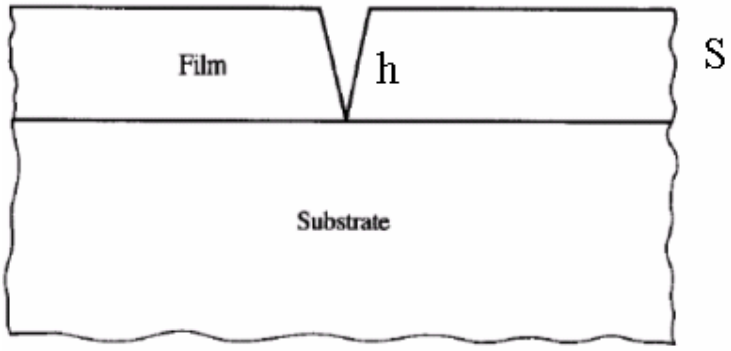

Figure 3: A typical "channel" crack. The crack terminates at film/substrate interface, but does not penetrate the substrate and h is equal to the film thickness, S.

2.2.2 Brittle Fracture and Delamination

Delamination is also a fracture phenomenon, but in contrast to the above described one turned by 90°; however, here, the Barenblatt (83) rather than the Griffith model is more appropriate. In contrast to the Griffith model where the crack tip has a small but finite radius of curvature, in the Barenblatt picture the crack has a "cusp-like" shape and is very much like that of the delamination "crack" shown in Figure 4a.

The basic parameter in the Barenblatt model is a modulus of cohesion K and is defined by the energy required to initiate separation of the two surfaces by delamination crack formation.

$$U_c = K^2\,(1-\nu^2)/\,E \tag{2.5}$$

the constant K is approximately defined by;

$$K^2 \sim 2E\,\gamma/\,(1-\nu^2) \tag{2.6}$$

Again here the poison ratio is neglected. By substituting γ by γd in the delamination case,

where γ_d defines the surface energy gained by delamination and given by;

$$\gamma_d = \gamma_s + \gamma_f - \gamma_i \tag{2.7}$$

The subscripts refer to delamination, substrate, film and interface respectively.

The criterion for delamination is found to be;

$$U = \sigma 2S / E \geq U_{cd} \tag{2.8}$$

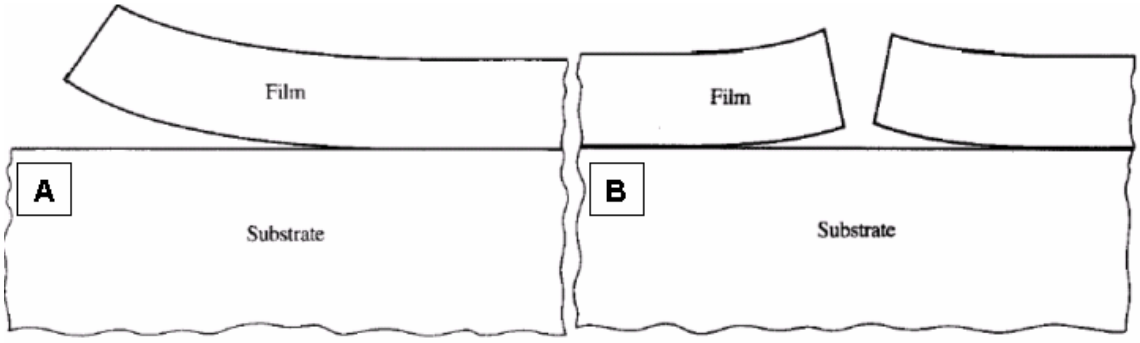

Figure 4: Sketch of delamination and fracture of thin film: A) Delamination of a film from a substrate; a "Barenblatt" crack, B) Simultaneous fracture and delamination.

This means, the probability of film delamination becomes greater as elastic energy of the film U approaches and exceeds U_{cd}. This equation is analogous to the one above (2.3) which allows some general inferences with regard to film fracture and delamination.

If $U \geq (U_c, U_{cd})$, then film fracture and delamination could occur simultaneously as seen in Figure 4b. Fracture before delamination will occur if $U_c < U_{cd}$ and for $U_c > U_{cd}$ delamination will probably occur before fracture. The last case is well known for films under compression that exhibit "blistering", where γ_d must be smaller inside the blister areas than outside, meaning that $U > U_{cd}$ inside but $U < U_{cd}$ outside. The lack of adhesion in the interior can be caused by the presence of a foreign substance, substrate imperfection, etc.

2.2.3 Stress Generation by Thermal Expansion

During heat transfer, the energy that is stored in the intermolecular bonds between atoms changes. When the stored energy increases, so does the length of the intermolecular bond. As a result, solids typically expand in response to heating and contract on cooling. This response to temperature change is expressed as its coefficient of thermal expansion: if thin film is deposited on a substrate of different material a change in the temperature will result in thermal strain on both. However a thick substrate will acquire a thermal strain, but remain stress free. The film also acquires a thermal strain, which differs from that of the substrate by

$$\varepsilon_T = (\alpha_f - \alpha_S)\, dT \tag{2.9}$$

Thin films on a substrate are usually in a biaxial stress state, especially in the case of thermal stresses induced by differences in thermal expansion coefficient between the film and the substrate. This thermal effect provides important contributions to film stress. When the film and the substrate are well bonded, the net in-plane strain in the film must be the same as the thermal strain of the substrate.

Consequently, the mismatch strain equation needs to accommodate the elastic and inelastic deformation in the film. If the film remains elastic during the temperature change, this mismatch strain induces a biaxial stress in the plane of the film, σ_T, given by:

$$\sigma_T = E_f \varepsilon_T / (1-\nu) \tag{2.10}$$

Where E_f is Young's modulus and ν is Poisson's ratio of the film. Stress can also be generated by applying a bending moment to the film-substrate composite in which the ductile substrate remains unfractured while the brittle thin film fractures. So the total stress in the film is the sum of the gross stress, the thermal stress, and the applied stress.

2.2.4 Stress Generation by Swelling

The swelling behavior of polymer membranes has been studied in several groups (84). It was found that the sample pretreatments and the type of the functional group have a strong effect on the swelling properties of these membranes. The swelling of sulfonate membrane is higher than that of the carboxylate membrane. Also, the membrane swelling can be increased by quenching the sample and increasing the solvent temperature (85).

A perfluorinated ionomer (trade name Nafion, DuPont chemicals) was found to be the most effective membrane. It shows a high ability to swell even if only exposed to the humidity in air. Structurally, Nafion consists of a hydrophobic region, constituted by tetrafluoroethylene (TFE) segments and hydrophilic ionic backbone formed by pendant side chains of perfluorinated vinyl ethers terminated by ion-exchanged groups. These allow Nafion to work as a proton transport membrane in fuel cells. The chemical structure of Nafion is shown in Figure 5.

If a brittle material is covering the Nafion membrane, swelling and shrinking can introduce a multiaxial stress that eventually causes cracks in the brittle mask. Analogue to thermal strain mentioned above the stress here is a result of the swelling strains (ε_s) which is given by;

$$\varepsilon_s = (\beta_f - \beta_s)(C-C_0). \tag{2.11}$$

Where β is the swelling expansion coefficient due to moisture absorption for film and substrate and C is the relative humidity, C_0 is the reference value for C.

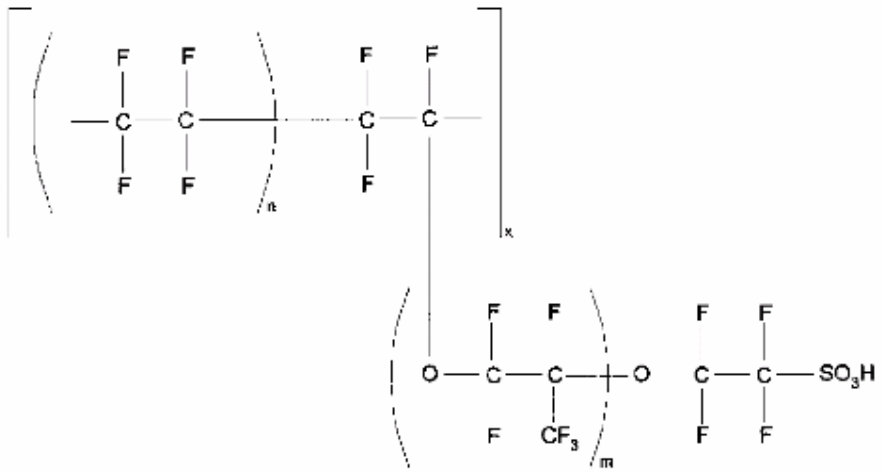

Figure5: Chemical structure of Nafion.

2.2.5 Fracture in Polymer

Brittle fracture of polymer has been widely examined (86,87). Fracture initiation, crack propagation, and termination, have been also investigated (88,89). It has been established that cracks appear in disordered, amorphous parts of the polymer and involve chain dissociation of stressed macromolecules by sequential thermal fluctuation.

In elastic materials Griffith's analysis predicts a stable crack growth for stress below the critical limit of failure and uncontrolled accelerated growth above the limit, due to the permanent excess of the released strain energy over the required surface free energy. As the polymer is neither elastic nor linear under the conditions near the failure, Griffith's approach which is based on linear elasticity theory become questionable even for brittle polymers like polystyrene (PS) and polymethyl methacrylate (PMMA) (90).

Polymeric materials show a specific feature characterized by the existence of a range of stationary slow growth known as "subcritical crack growth", which is characterised by the role of the flow process (15). Intrinsically, in the polymer, the appropriate mode describes a detailed picture of the flow process controlling the crack growth starting from a macroscopic notch or being initiated somewhere near to the flaw (91). At this mode, a crack is formed within a so called craze where the subcritical crack growth starts. At a distance (r) from the crack tip the classical fracture mechanics predict a stress singularity at $\sigma \sim r^{-1/2}$. At larger distance this relation will break down and the discussion of the crack-tip process zone is more relevant (92,93). The crack propagation energy will, in general, depend on the nature of the process occurring in the crack tip zone. The stress intensity factor, K, or the energy release rate, G, at the onset of crack growth is then determined as a parameter that controls fracture initiation. However, a more detailed investigation is required since most polymers generally undergo some viscoelastic deformation in regions of high stress concentration.

Deformation of polymer in this zone occurs generally by crazing (94,95) or shear flow (96,97). Mostly, one of these two mechanisms dominates the deformation behavior. For thin films, plane stress conditions near the free surfaces often lead to shear flow, whereas the plane strain condition in the interior favors craze formation. Moreover, lower temperatures favor craze growth where at higher temperatures cause shear deformation.

However, there are specific situations, where both mechanisms occur simultaneously on an almost equal level (98). In these cases, fracture is noted to proceed via multiple crazes prior to crack propagation. The event of fracture instabilities involving the formation of multiple crazes have been rationalized as the interplay of shear deformation with crazing in the crack-tip plastic zone. The presence of multiple crazes increases the toughness and complicates the fracture process, as indicated in several research efforts (99,100). The results indicate that below a critical temperature multiple crazes form ahead of the crack and fracture toughness increases. Above this critical temperature a transition from multiple crazes to a single craze takes place and the fracture toughness decreases.

Models used to describe the crack tip zone and subsequently the craze mode cracks in polymer are derived from Barenblatt model as well as the classical Lake-Thomas (101). In the Barenblatt model the crack has a “cusp-like” shape with crazed matter in front of the tip. The craze growths radially and is followed by the crack tip within the craze region. According to this model fracture occurs by chain elongation in front of the crack tip followed by chain scission as described in the ”Lake-Thomas picture”: Polymer segments crossing the fracture plane are stretched out until they store an elastic energy per monomer that of the order of the covalent binding energy. However, the actual fracture and deformation process is very complicated and involves cavity formation, chain pull-out, etc. As the elongation step mentioned above requires some time where the polymer chains can rearrange themselves, i.e., disentangling (e.g. by thermally activated flipping of polymer segments) a slow crack velocity as well as a low molecular weight cause rapid fracture. Indeed, the intramolecular covalent forces, intermolecular van der Waals forces, the heterogeneous microscopic structure, and the presence of chain slippage and chain scission complicate the mechanisms significantly.

Other factors such as a decrease of the polymer glass temperature and reduction of surface energy by the influences of environmental gases or liquids, i.e., swelling, and plastization have a significant effect on crazing and failure of a polymeric material by facilitating chain mobility and reducing the barrier for crazing and fracture. Furthermore UV radiation leads to a sharp acceleration of fracture by means of degradation. Degradation is reflected in changes of material properties such as changes in the molecular weight by fragmentation of the main chain, splitting off of low-molecular weight species, cyclization, branching and cross-linkage. Even more, crazing, cracking, erosion, discoloration, phase separation or delamination can occur.

2.3 Fabrication Technique

In general, to fabricate nanowires using fracture, several steps are necessary as sketched in Figure 6. These steps are: mask deposition, crack generation, deposition of the nanowire material and a mask lift off. Each step associated with this approach will be discussed individually. However, apart from the advantages there are also some challenges during the fabrication process. Those will be elucidated during the results and discussion section.

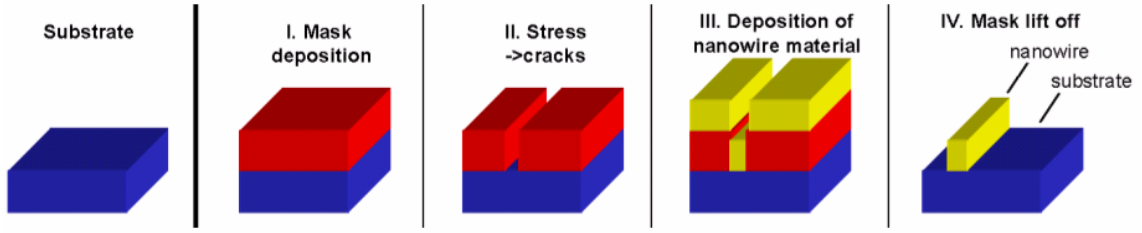

Figure 6: An illustration of the crack induced nanowire formation process.

2.3.1 Choice of the Substrate

The choice of the substrate is limited only by its ability to withstand the applied stress. According to the type of stress, different substrates are selected. In case of biaxial stress, substrates like silicon and glass are used. For flexible substrates like commercial polymer foil (102), and stainless-steel foil, uniaxial stress is applied. Biaxial stress is introduced by means of membrane swelling in Nafion. A cleaning step freeing the substrate from dust or grease is usually done.

Commercial silicon or glass samples approximately (1-2 x 1-2 cm^2) are typically purified by air-blower and then cleaned with isopropanol by ultrasonication for 30 minutes and subsequently dried in air. Foil species of Nafion (Nafion 107, DuPont, 2 x 2 cm^2) or stripes of commercial polymer foil (3 x 1 cm^2) commercial inkjet transparency film, Canson, Annonay, France) and stainless steel foil was grease free and used without any cleaning other than air-blower.

2.3.2 Choice of the Thin Film "Mask"

The choice of the thin film that can be used is only limited by its ability to be fractured. Consequently a brittle material is most desirable. Amorphous films are used to avoid constraints arising from perforated growth of cracks along specific crystal directions in the crystalline materials.

Experimentally, amorphous carbon or polymers like PMMA, PS, as well as a commercial Photoresist, Trade name "POSITIV 20" (103) whose main ingredients are Diazonaphthaquinone/Novolac polymer are used. The chemical structures of the polymers used are sketched in Figure 7.

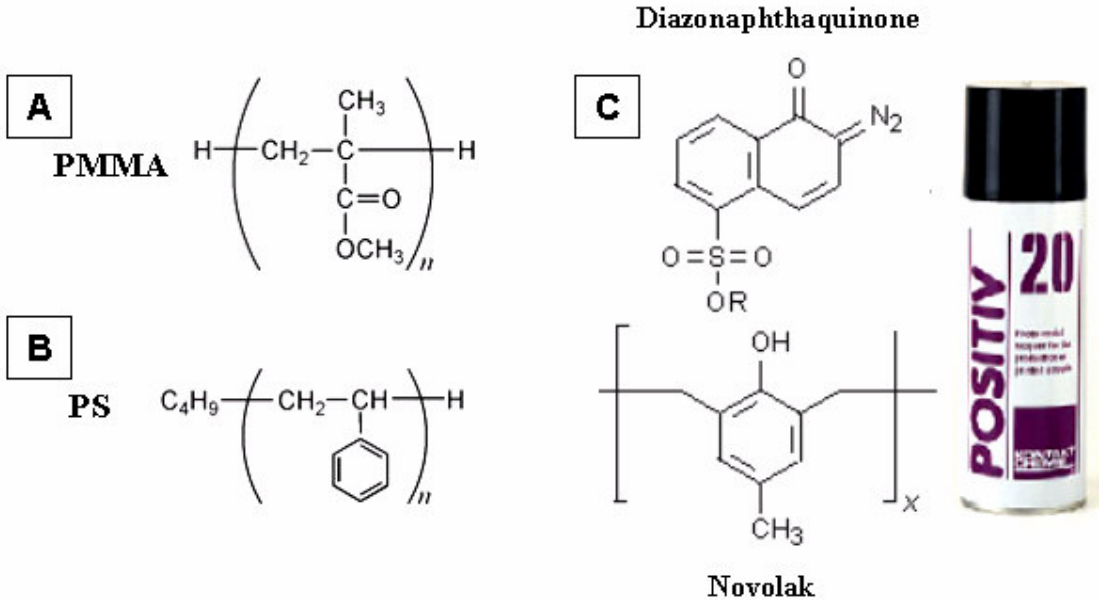

Figure 7: Chemical structures of the mask used; A) PMMA, B) PS, C) Positive 20.

Deposition of the mask varied depending on the nature of the material. The carbon thin film was deposited in a "Balzers Bal-Tec SCD 050" carbon coater under pre-vacuum conditions by flash evaporation (sublimation of a carbon thread by ~200 W, 20 A) on a Nafion substrate. The film thickness is tailored by varying the number of the deposited layers. Generation of nanocracks was observed after a deposition of three layers corresponding to a film thickness of ~ 400 nm.

Among the possible ways of depositing polymers, spin-coating is simple, cost-effective and can be easily handled. In our experiment, the spin-coater "P-6708D" from Specially Coating Systems (USA) with rotational speed up to 3000 rpm is used. PMMA can be dissolved in many solvents such as toluene, methylene chloride, methyl ethyl ketone, acetone etc. and its solubility parameters of various solvents have been studied (104). In our experiment, PMMA with a molecular weight of 35,000 g/mol was used as bought from Scientific Polymer Inc. It was dissolved in toluene by keeping in an ultrasonic bath for 25 minutes. PMMA solution was deposited on silicon wafer with a rotational speed of 1000 rpm. A different film thickness is obtained with 0,5 g of PMMA and changing the amount of toluene solvent as illustrated in Figure 8. A film thickness, measured with a profilometer after complete drying, in the range (400-600 nm) is used.

In order to simplify the procedure, Photoresist is simply sprayed on to the substrate at room temperature, solvent evaporates and film dries up. Spray-coating with an aerosol can is easiest for small production runs.

Mask materials based on polymers are degenerated by exposure to UV light using a commercial UV lamp (Conrad) over night. It is well known that irradiation of polymers lowers their average molecular weight by chain scission and thereby decreases the strength of the intermolecular interaction

(105). As a result of irradiation, the strength of intermolecular interaction becomes less than the strength of the basic chain bond, consequently breakage occurs mainly at intermolecular bonds.

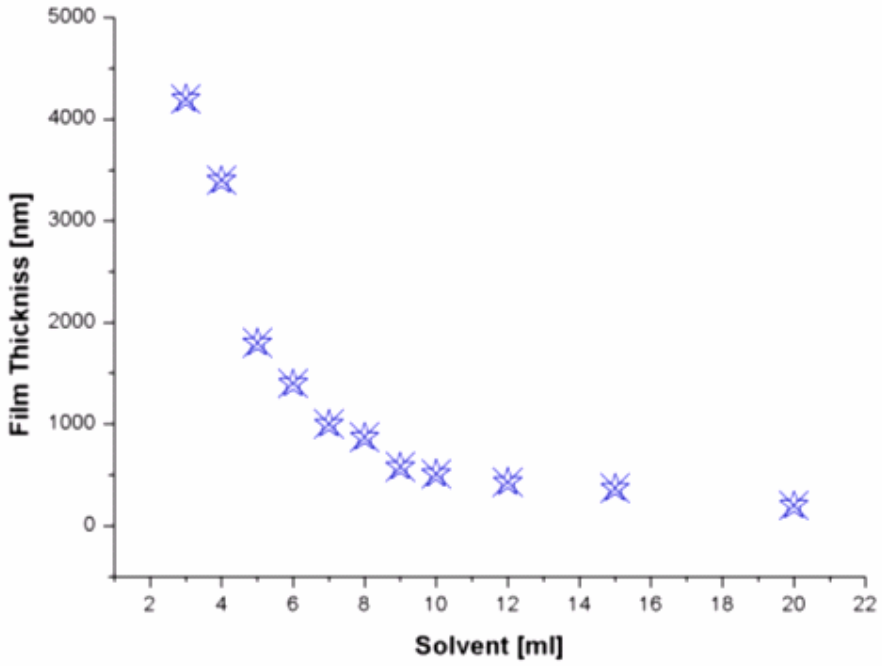

Figure 8: Variation of PMMA film thickness.

2.3.3 Cracks

In this work cracks are formed by inducing mechanical stress in the thin film, either by thermal cycling, swelling of the substrate or simply by mechanical bending.

In the experimental work, cracking of polymers i.e. PMMA on substrates like silicon or glass was based on thermal stress. The sample is heated to 90 °C for 30 min. and then exposed to liquid nitrogen.

In case of stainless steel or commercial foil, photoresist is used as a mask. Cracks are generated simply by bending the substrate. Here, the film is fixed at one side and bending initiated at the other free side. Sketch in Figure 9 illustrates this approach and depicts the effect of proper bending and improper bending on the alignment of cracks in the film.

When Nafion is used as substrate and is covered with an amorphous carbon thin film cracks are observed directly after the film deposition

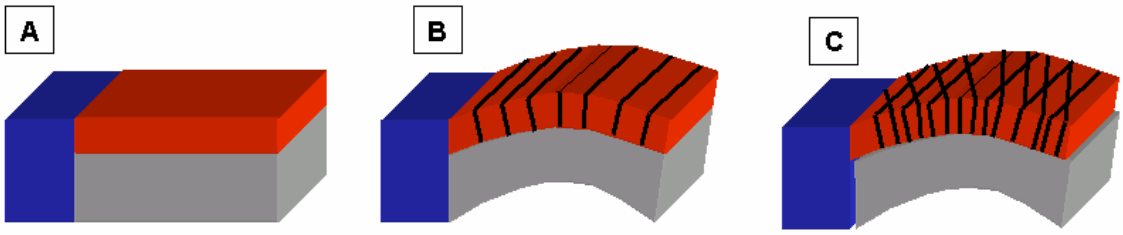

Figure 9: An illustration of the crack induced by bending: A) the film covered the substrate fixed in one end, B) Align cracks by proper bending, C) Random cracks by improper bending.

2.3.4 Choice of the Wire Materials

As the wire material is grown by physical deposition techniques the choice of the wire material is only limited by its ability to be sputtered or evaporated. So a wide variety of metallic, polymeric, composite, magnetic wires, etc can be formed.

A typically used deposition condition is as follows: After cracks are formed by the steps discussed above, 2 nm of chromium were deposited by thermal evaporation in an ultra high vacuum under a pressure of 10^{-6} mbar at a rate of ~19.7 Å/min, using a current of 3.9 A and a voltage of 17.8 V. the chromium is used for adhesion enhancement of the metal on the substrate. Sputtering, which gives better adhesion as compared to thermal evaporation, was used to deposit a layer of 20-40 nm nominal thickness of the wire material (typically gold or silver) . The sputter process was done at a power of around 16 W and a rate of 1.5 Å/min. Sputtering was carried out in an ultra high vacuum chamber for all the samples using an Ar ion beam under a pressure of 10^{-3} mbar.

2.3.5 Mask Lift-Off

The next step is removing the excess metal layer by removal of the mask. Mask lift-off was done using acetone as a solvent and keeping the sample in an ultrasonic bath for a few seconds. In this way, only the material which was deposited directly on the substrate in the cracks remains on the surface, resulting in nanowires. However there are some challenges during the mask lift-off process like;

a) complete removal of the nanowires is observed by exposing them for a long time to acetone in an ultrasonic bath, indicating weak adhesion properties between the deposited metal and substrate, b) incomplete mask lift-off which occurs after insufficient exposure as is shown in Figure 10a. To circumvent these problems, chromium is used as an adhesion promoter and exposures to acetone in ultrasonic bath is done for about a second at a time with several repetitions. This procedure shows a high efficiency as seen in the SEM image shows in Figure 10b.

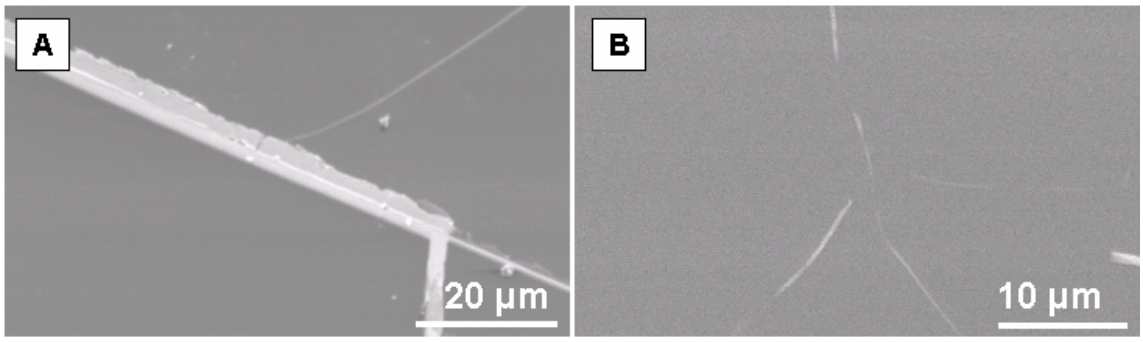

Figure 10: SEM images illustrating the effect of the mask lift-of on the wire width, A) an incomplete mask lift- off, B) complete mask lift-off.

2.4 Results and Discussion

2.4.1 Characteristic Fracture Pattern and Unorganized Nanowires Network

Random thin film crack patterns in several systems have been widely studied (106, 107 and references therein). The pattern shows a distinctive hierarchical structure (108). Common features noted in the crack pattern in various samples are cracks meeting each other at right angles. This is due to the fact that a crack propagates in the direction which most efficiently relieves the stress. Since the stress near a given crack is parallel to its surface, other cracks tend to approach and meet it at right angles, this leads to a connected network pattern. A famous pattern for such a cracked film is a field of dry mud, as showed in (Figure 1), which is also found for PMMA on silicon substrate under thermal cycling as shown in Figure 11. However, a similar pattern was found for other stress types like swelling and scratching as well.

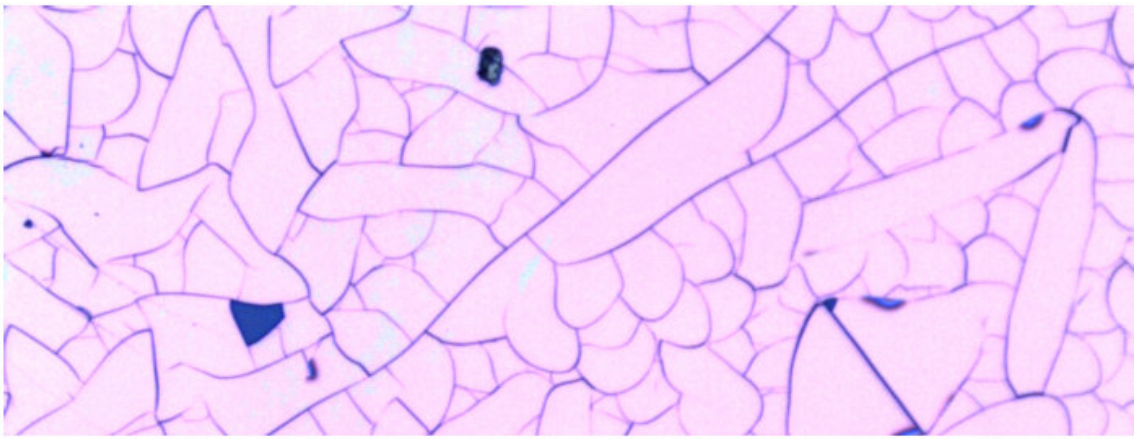

Figure 11: A cracked PMMA film looks like a field of dried mud.

2.4.1.1 Network by Thermal Cycling

On a constrained brittle film cracks can grow laterally in the film until they meet the film edge or another crack. The lateral crack length can be several times the film thickness. Thin films on a substrate are usually in a biaxial stress state. This especially holds for thermal stresses induced by differences in the thermal expansion coefficients between film and substrate.

Using the pattern above as a template and depositing material on it, a large area of wires can easily be fabricated as shown for the case of gold on a silicon substrate in Figure 12a. As expected the wires show a network of intersected structures as can also be seen in the dried mud pattern. Intersecting wires on different scales are observed as illustrated in Figure 12b. It is difficult to achieve a monodisperse crack width distribution as the fracture mechanics for the dried-mud structure suggest a hierarchical sequence. The hierarchical nature of the cracks, which results in complex and intersecting structures, was found in various samples and on different scales. Figure 12c,d show mesowires of “Y”

structure on a printer foil substrate and “T” nanowires on a silicon substrates, respectively. in both cases photoresist ”Positiv 20” is used as a mask.

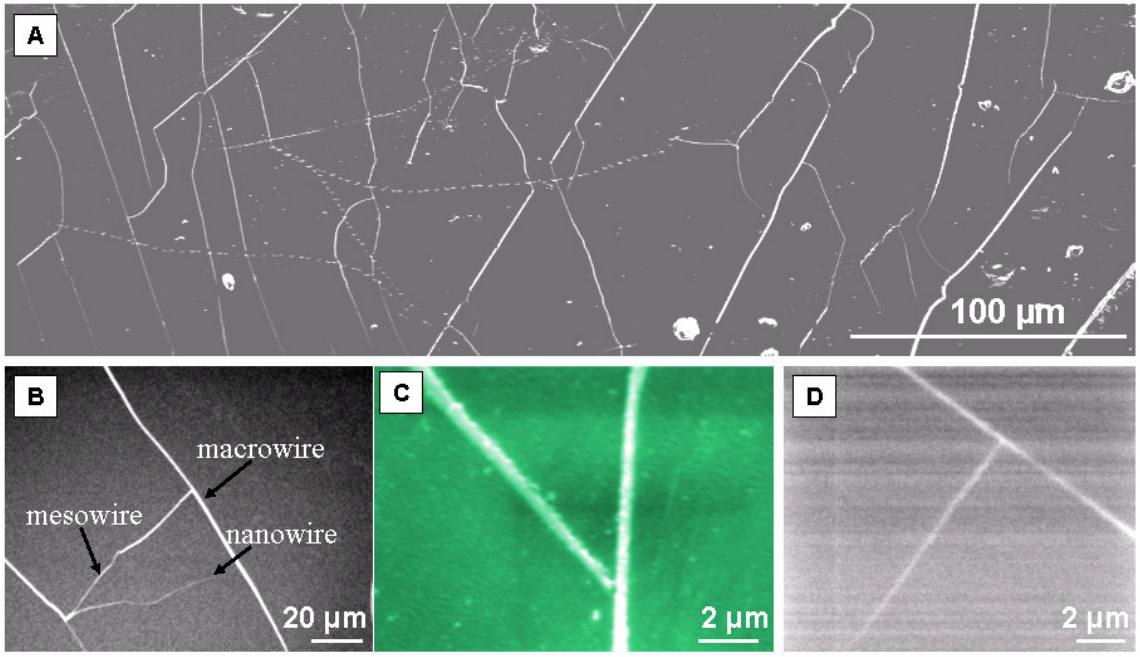

Figure 12: SEM showing gold nanowires on silicon after template lift-off: A) The wires cover a large area on the substrate. B) Different wire diameters as a result of different cracks opining width. C,D) show the hierarchy nature of the cracks causing a formation of meso and nano intersected wires on different substrates.

As cracks are used here as moulds for a nanowires production by filling them with a second material, mainly two challenges must be met: I) Crack openings should be on the order of nanometers and II) Cracks should propagate all the way to the interface and arrest there to facilitate the filling process.

In order to form nanocracks in a controllable and reproducible manner in the polymer/Si system by thermal cycling, several parameters like film thickness, heating temperatures, cooling time, and the way of exposure to LN_2 are examined.

The film thickness plays an essential role for the mechanical behaviour, the thinner the thickness of the film the less the stress develops in the mask-film and the less probable it is to get cracks. There is a critical thickness below which no cracks will be formed (see eqn 2.4 above). This behaviour was observed here, as no cracks are observed for film thickness of ~100-300 nm. Sub-micron cracks are observed for a film thickness of ~ 1-2 µm. Cracks in the range of nanometers are obtained by film thickness with 300-700 nm.

Backing the polymer solution until hardened is done to drive out all the solvent that can result in film fracture (109). The predominant factor behind the formation of these cracks is the rearrangement and relaxation of the polymer chains to relieve residual stress resulting from shrinkage (i.e. loss of

solvent). Heating and cooling as well as a fast alternation between them are examined as a fracture generating source. Experimentally, no cracks are observed to arise by only heating of PMMA, PS, and Photoresist at temperature range of 60-200 °C for an hour. It turns out, that the residual stresses developed here by the loss of solvent are insufficient to caused fracture. As the polymer-modulus varies by increasing the temperature with a high loss tangent slightly above the glass temperature, the stress developed could be reduced by the viscoelastic deformation, and consequently the yield strength will be decreased and no cracks will be formed. Additionally, no fracture can be observed only by cooling, i.e., dipping in liquid nitrogen LN_2. It shows that the thermal strain and subsequently the resulting stress is not high enough to break the stiffened chains, however the lack of disentanglements can also hinder the crack formation. A combined effect of heating followed by rapid cooling is found to be the most effective way for cracks generation. Long term heating (60-90 min at 90 °C) and dipping in LN_2 is observed to cause film flaking as seen in Figure 13a, which can be explained by a lack of adhesion upon long time heating. Mostly submicroscopic cracks are obtained by heating for short time (20-30 min) followed by dipping in LN_2 (Figure 13b). Nano cracks were found after the following optimized procedure: The mask is heated up to temperature close to the glass temperature of the polymer and kept for 30 min. on hot plate. Exposure to vapor of liquid nitrogen VLN_2 causes a thermal stress on the composite which latter released via nano cracks on the photoresist as shown in Figure 13c.

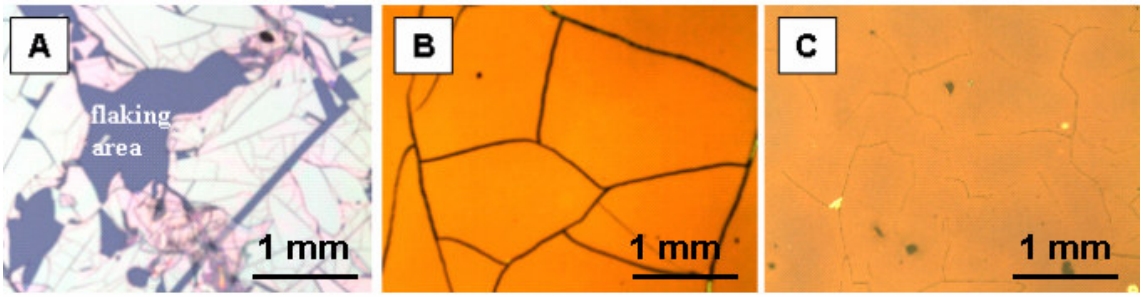

Figure 13: Cracks under several conditions: A) Worse condition leading to flaking and delaminated areas: Heating for an hour at 90 °C than dipping onto LN_2, B) Heating for 30 min. at 90 °C than dipping onto LN_2. results in wide openings, C) Good conditions: Heating for 30 min. at 90 °C than exposure to VLN_2. The scale bar in all images is 0,1 mm.

Indeed, Figure 13b,c show the main role of the exposure way to LN_2 on the cracks diameter. To visualize this effect two identical samples are prepared by the procedure mentioned above where one of them is dipped into LN_2 and the other one is exposed to VLN_2. As shown in the AFM image in Figure 14, the crack width in case of VLN_2 treatments is five times smaller than LN_2. In contrast to the LN_2 method where a submicron crack of 540 nm is obtained, a nanomould of ~110 nm is realised by VLN_2. These dimensions are reflected in the wire diameters. Figure 15a shows an AFM image of sub-micron gold wires with a “T” structure, the cracks are fabricated by dipping in LN_2.

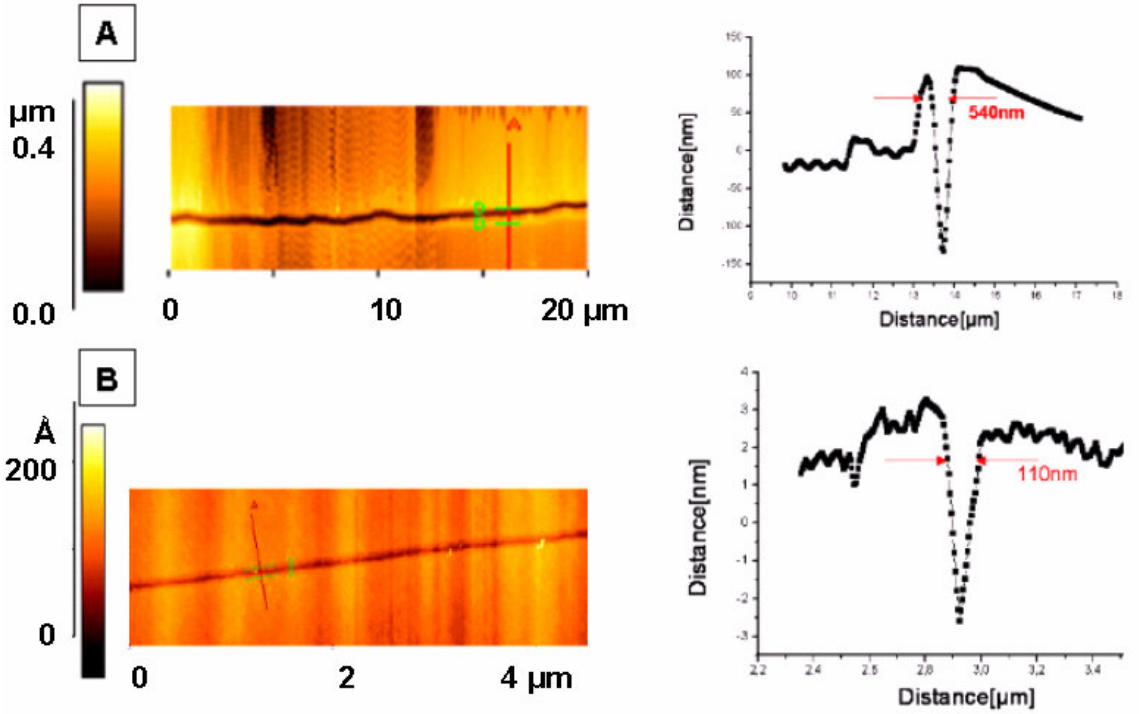

Figure 14: AFM analysis along the crack showing the effect of the exposure way on the cracks width: A) Sub-micron cracks ~ 540 nm, by dipping in LN_2, B) Nanocracks ~110 nm by VLN_2 procedure.

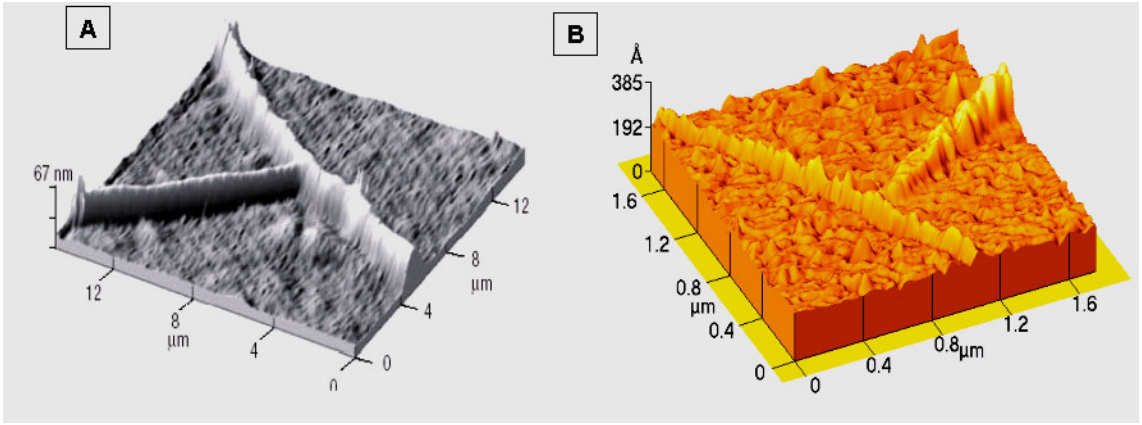

Figure15: AFM showing the the effect of the exposure way on the wires diameter: A) T structure of sub-micron wires by LN_2. B) Nanoscale-T intersection by VLN_2.

In contrast the same "T" structure but with one order of magnitude size reduction, only 60 nm is realized by using VLN_2 as shown in Figure 15b.

It is worth to mention that the crack was not observed in PS using the above method described above. Under the harsh condition of thermo-cycling only holes are observed. Consequently that system was abandoned.

Reduction of the wire size which is typically comparable to the crack width can be achieved by using deposition under an angle. Figure 16 show AFM images of crakes with 85 nm width and a resulting 50 nm Gold wire after the deposition. However this part will discussed later in more detail.

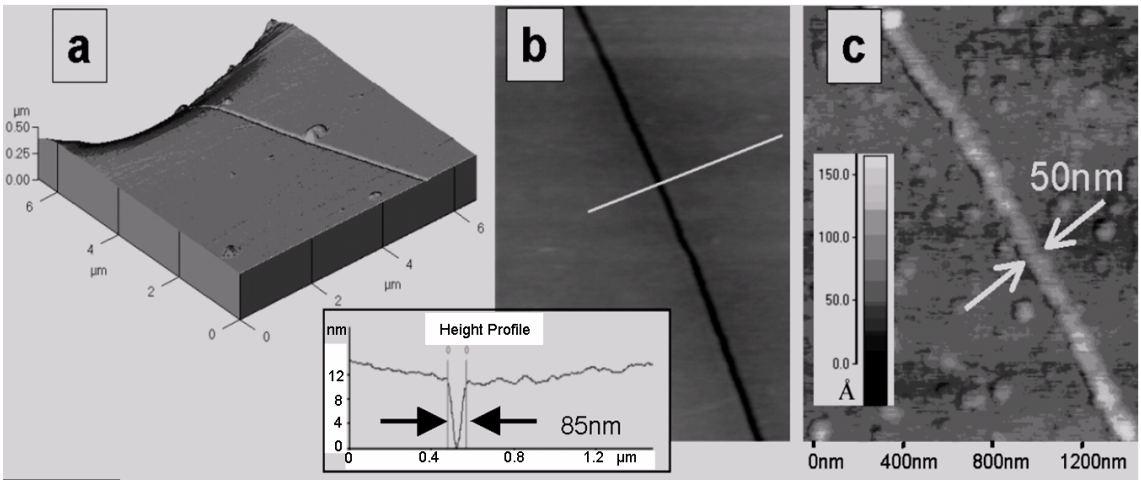

Figure 16: Images of nanostructures. A) AFM image of a thin film containing a nanosized crack, B) magnification from a, the structure is 85 nm in width. C) 50 nm Au-nanowire on Si by using the mask from A).

2.4.1.2 Network by Scratching Technique

Contact problems between the wires are a severe disadvantage of many techniques problems not solved yet (110,111). Here, realization of a one step forming device approach is developed by employing a hand-made macro-scratching technique. A 500 nm thick PMMA film on a silicon substrate is kept on a hot plate at a temperature of 90 °C for 35 min. Cracks are obtained by simple scratching using sharp utensils. After gold deposition, that filled the cracks as well as the scratched areas, mask lift off is done.

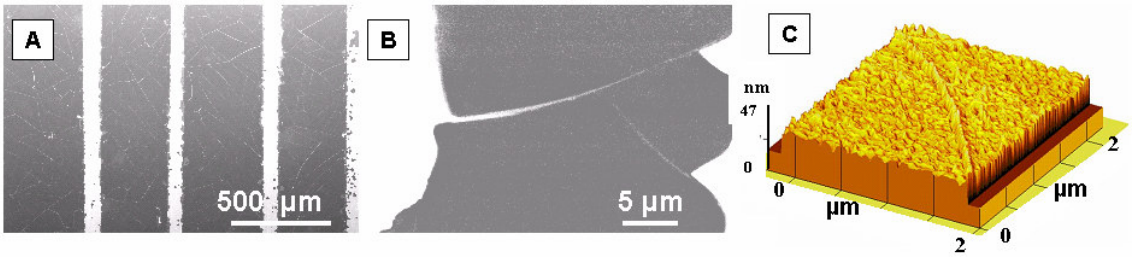

Figure 17: SEM images showing the resulting gold nanowires on Si based on hand-made-scratching of microchannals: A) the wires are suspended on both sides of the scratched area. B) One step device, the wires connected the scratch area, which act as contacts. C) AFM shows a 37 nm wire fabricated by scratching approach.

High densities of gold nanowires were suspended between the gold contacts as seen by SEM Figure 17a. A higher magnification in Figure 17b provides evidence for a one step commercial device fabrication and depicts the gold contact and the suspended gold nanowires. The advantage of this particular structure is that the wire forms simultaneously with the macroscopic contacts. Furthermore, wires with diameters below 40 nm can be generated by scratching approach as seen by AFM Figure 17c.

2.4.1.3 Network by Swelling

A particularly simple way to provide stress is if Nafion serves as substrate utilizes its natural ability to swell by soaking up water (112). For this method amorphous carbon is used as thin film material. Tailoring the crack density and diameter was done by varying the number of deposition layers. In case of one layer deposition, where a thin film of 100 nm is formed, no crack is observed and only film buckling takes place. Nano-cracks are found in the case of three layers with a 250-300 nm film thickness, while increasing the deposition to five layers with a 500-600 nm film thickness, leads to submicroscopic cracks. AFM, Figure 18a,b, illustrates the difference between the three and five layers, respectively. Cracks organize themselves in the carbon film by the water uptake that occurs if the Nafion is set off the air humidity after deposition of carbon in vacuum (113).

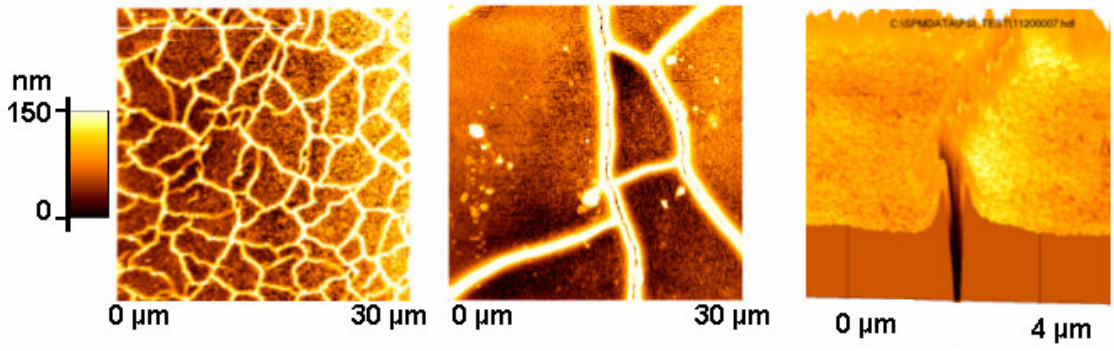

Figure 18: AFM showing cracks in carbon thin film on Nafion by swelling. A) High density of smaller cracks by 3 layers deposition. B) Low density of broader cracks by deposition of 5 layers. C) 3D image of a crack.

For catalytic purposes in fuel cell membranes, platinum (Pt) particles are distributed on the surfaces of Nafion. Therefore, an interesting approach is the decoration of Nafion with Pt nanowires which will facilitate the electron transport in the membrane beside their catalytic activity (114). A network of Pt nanowires on Nafion is shown in SEM, Figure 19a, a higher magnification in Figure 19b provides evidence for wires below 100 nm. Figure 19c shows an EDX map demonstrating the platinum signal as seen in Figure 19d. Broad wires were chosen to be able to perform a chemical analysis of the Pt wires on the insulating polymer, as thinner nanowires were burned away immediately together with the charged substrate by the electron beam. This is also the reason why a sample area is chosen where an incomplete mask lift off was performed. But even this amount of material is close to the detection

limit of the EDX detector. Beside the noise, the EDX line scan shows the good isolation of the platinum wire from the surrounding area.

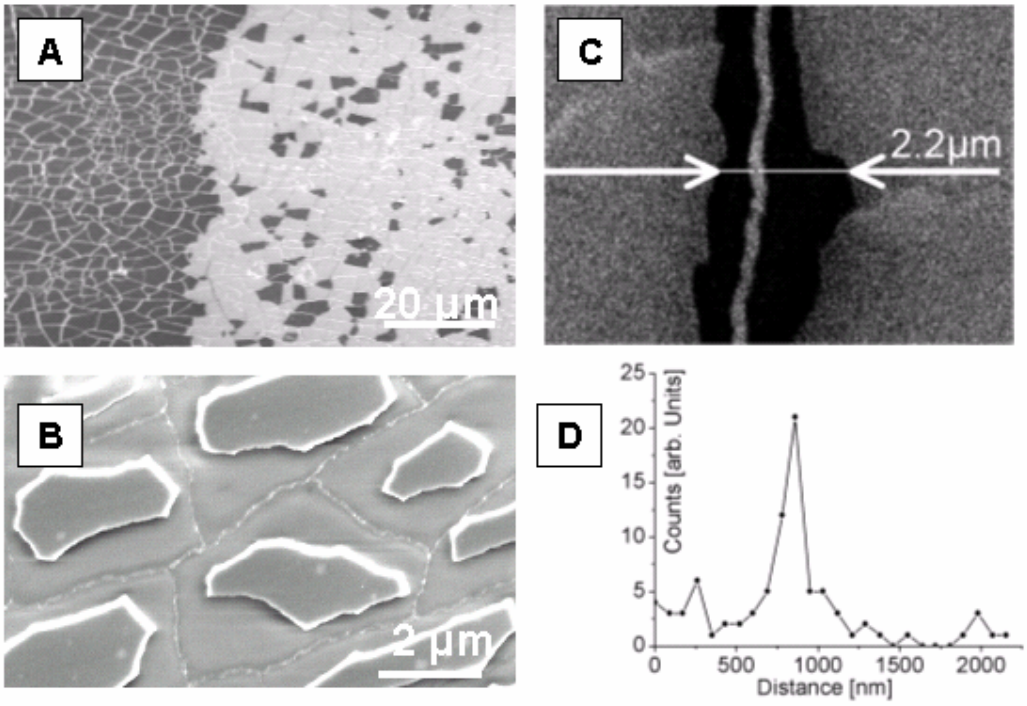

Figure 19: SEM showing network of Pt. nanowires on Nafion membrane: A) Pt nanowires formed in cracks of amorphous carbon on a Nafion substrate with partially mask lift off, B) high magnification of the nano wires with some mask islands between them, C) The mask is only partially removed around the wire, allowing to prove the composition of the wires with the EDX detector, D) EDX line scan along the line marked by the arrows in C).

2.4.2 Alignment of Nanowires

Even though fracture is a well controllable phenomenon, only very recently a systematic employment of thin film fracture is performed to create structures. Thin film cracks follow strain fields and can be controlled in width, length and density. Alignment of cracks can be achieved in many different ways as illustrated above in Figure 2. Simply bending is one of these ways. If a homogeneous, brittle thin film is used as template, a bunch of parallel cracks can be produced by applying uniaxial stress, e.g., by bending. The Optical image in Figure 20a shows such simple alignment using this approach. Here, in order to show the flexibility as well as to apply more customary in the fracture approach, widely available materials like Standard inkjet printer foil is used as a substrate. The foil was coated with photoresist and dried in air. The photoresist thickness was determined to be approximately in the range of 1 µm. The film was then exposed to UV light for 15 hours to effect an embrittlement by photo degradation.

Bending of the elastic substrate foil leads due to the above mentioned "bending beam" to tensile stress in the brittle photoresist thin film. The stress is uniaxial and leads to cracks that can be down to the nanoscale with a quasi well defined quasi periodicity, as known for the case of fracture under constriction (115).

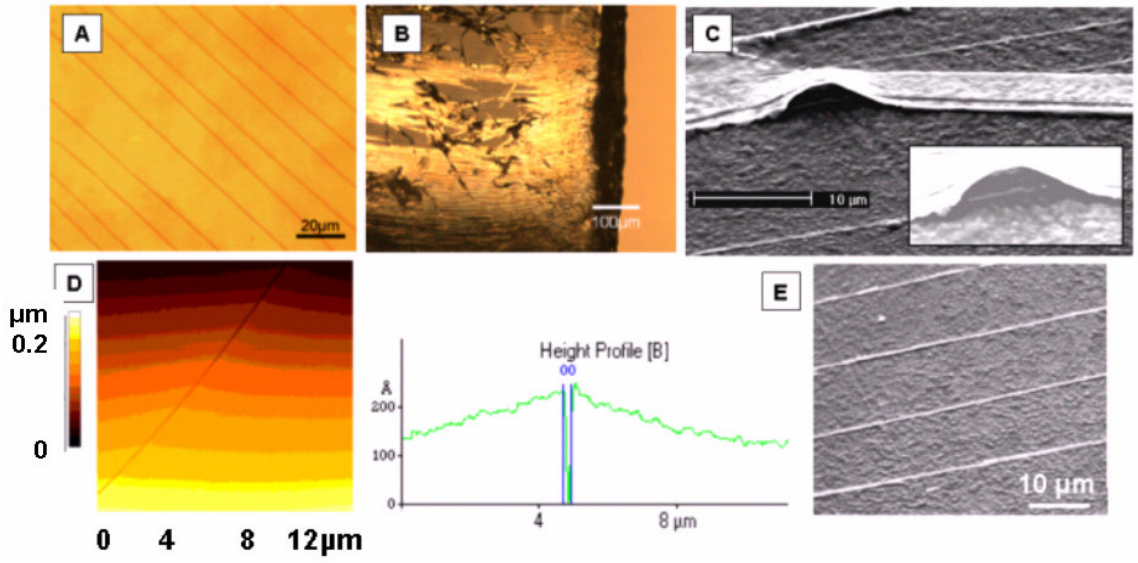

Figure 20: Images of aligned wires: A) Optical image showing a parallel cracks on a printer foil by bending. B) Optical image showing the strips and the wire on the foil during the mask lift off. C) SEM to clarify fig c and showing also the continuity of the wire underneath the strip. D) AFM illustrates the delamination of the cracks. E) Parallel arrays of gold wires after complete lift off.

Each crack under constriction will relax only a limited area, which explains that neighbouring cracks keep a well defined distance between them. By controlling the amount of stress, e.g., by the amount of bending, the wire density can be controlled.

After gold deposition, the photoresist was removed by a subsequent mask lift off with acetone. Here, the mask including the excess metal is removed as stripes; see optical image Figure 20b, where the wire underneath still adheres to the substrate as seen clearly in the SEM illustration in figure 20c. The part on the lower right of Figure 20c shows the continuity of the nanowire under the mask. The obtained cracks are mainly delaminated as observed by AFM Figure 20d. This occurs if the stress at the bottom of a crack is large enough that it can overcome the adhesion of the thin film with substrate. Such delaminated cracks have several advantages as will be illustrated later. Figure 20e shows parallel alignment, achieved on a polymer substrate by bending after complete mask lift off. Such polymer films can be used as transparent asymmetric conductors.

Not only gold but also silver wires can be fabricated. Figure 21a, shows an optical image “dark field” of parallel wires. The wire diameter is found to scale down to 100 nm as seen on the SEM image, Figure 21b. Due to the low signal, a Gaussian fit was done for EDX line scan of the silver wire, which

is shown as onset in Figure 21b. As we mentioned above the wire materials are only limited to their ability to sputter, parallel arrays of nanocomposite, here Ag/Teflon can be also achieved as seen in Figure 21c. Also here a Gaussian fit for the line scan to identify the flour signal by Teflon is seen in Figure 21d.

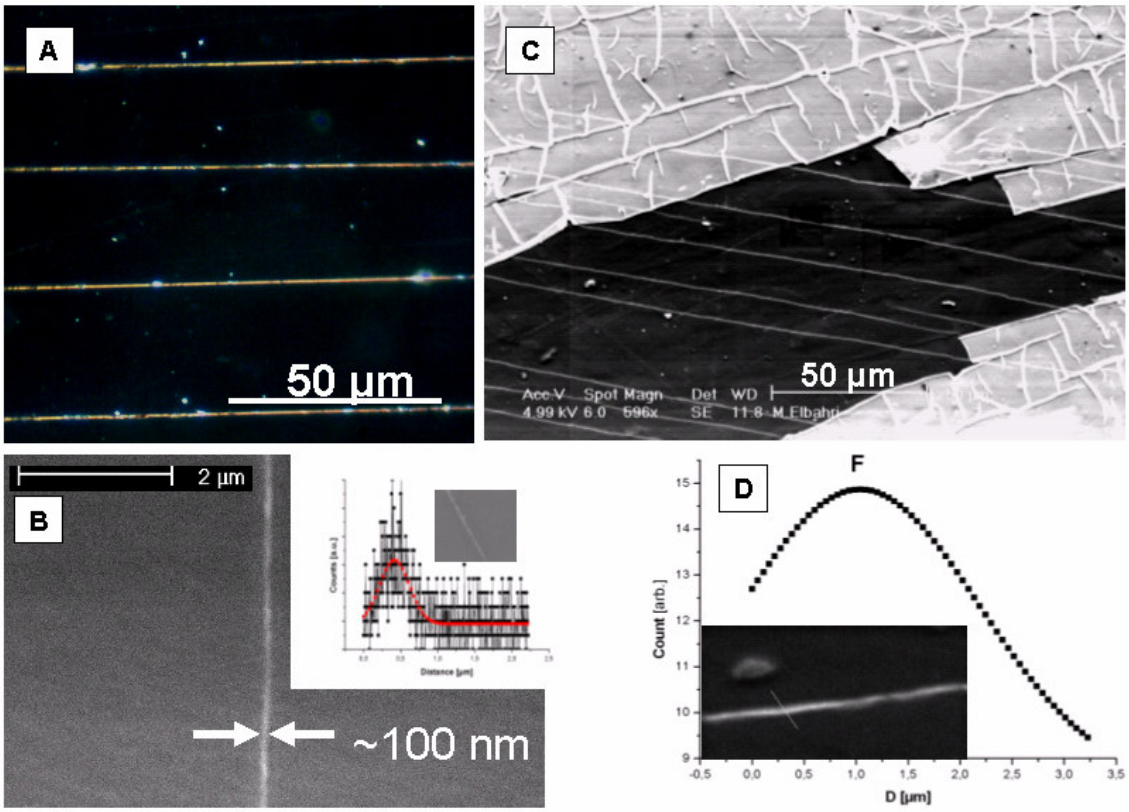

Figure 21: Wires of various materials: A) Dark field of Silver arrays, B) SEM of 100 nm wires with an EDX line scan on the side of it. C) Ag/Teflon Composite nanowires illustrated by SEM during mask lift off, D) Gaussin fit of an EDX line scan indicating the flour by Teflon.

Evaporation of a carbon thin film onto the polymer substrate was done to prevent charging effects. This standard procedure for non conductive SEM samples ensures that the scanning electron beam will not be deflected by an insulator like our polymer substrate. Without covering, the polymer it will charge up and the e-beam will be partially deflected, causing an intensity change. Charging can be also suppressed by leaving some low gas pressure in the sample chamber rather than to work under high vacuum. An example is Figure 22a showing a 60 nm gold wire taken with an SEM backscatter detector at high resolution by M. Schossig (GKSS).

Alternatively, such charging effects can be used to visualize the conductivity of the wires. This can be observed in Figure 22b, between two wires, a broad area of enhanced intensity shows the charging and thus the isolation between the wires. Directly next to the wire, no charging can be observed, meaning the electrons will be able to reach the wire before they charge significantly.

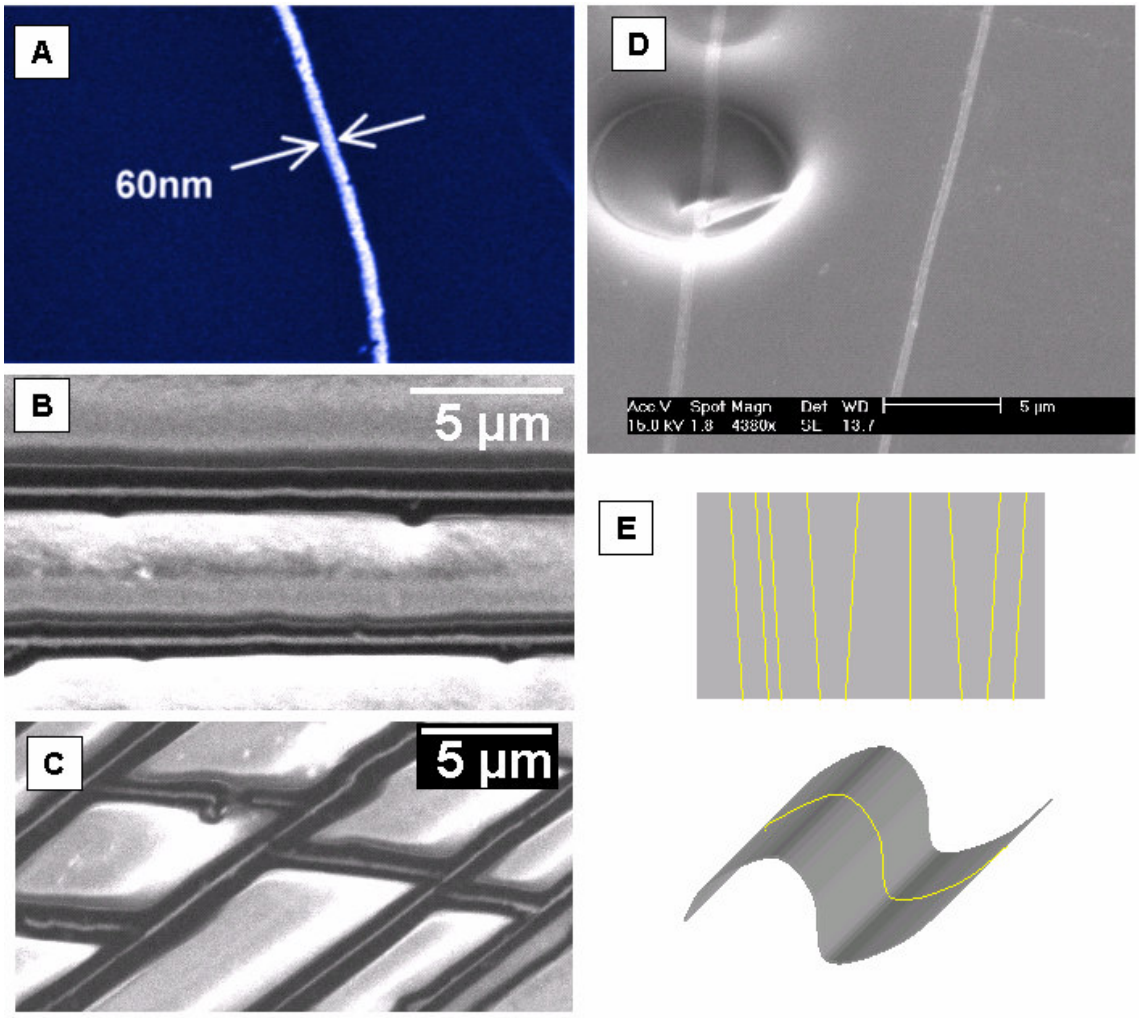

Figure 22: Visualization of some properties of the wires: A) 60 nm wires with Back scattering-SEM (GKSS) under high pressure to prevent charging. B) SEM shows the charging effect at a parallel wires and C) in a crossed wires "grid". D) SEM illustrates the mechanical stability of the wire during foil impression, E) Making use of the mechanical stability and the conductivity of the wires for a broadband cable.

In contrast, Figure 22c shows a grid of crossing wires, such a complex pattern can be formed if stress is applied a second time from another direction. Turning the substrate by 90° and applying stress will lead to a crossbar network of cracks and subsequently wires. The grid is able to provide conductivity in both directions and contains insulated islands instead of insulated stripes. Figure 22d gives a hint for the mechanical properties of the wires. It shows how a wire can be bent without braking under foil impression which is formed in the polymer due to a high acceleration voltage (15kV) applied in a particular area. Recently it was shown that, Young's modulus of metallic materials is essentially independent of the dimension, but the yield strength of nanowires is 100 times greater than that of bulk material (116). The detailed mechanism is still not proven, it is likely that the finite material volume and grain size in nanowires have a strong impact, making the nanowires more elastoplastic-like than bulk. This behavior of the wire on the plastic foil allows in principle the fabrication of transparent

electrode with a broadband cable just by clipping multi-conductor plugs to both ends of the wires arrays: If all wires are well insulated against each other, an individual contact on one plug should just lead to only one at the plug on the other side. That is simply sketched in Figure 22e.

2.4.3 Shadow Mask-Delamination Approach

As described so far this "fracture approach" has been limited to nanowires consisting of a homogeneous material. Also the patterning of the nanowire network is restricted to the boundaries of fracture mechanics. For example, to fabricate two parallel cracks with a separation on the nanoscale appears to be a difficult task. This is because, when strain fields around two parallel cracks are too close, there is a driving force uniting both cracks. These mechanisms for thin film fracture are well understood; e.g., see review (117). To overcome this deficiency, we combine the approach based on thin film fracture with the nano shadow mask approach (118). Nanostructures formed by shadow masks can be deposited with only a few nanometer separation by changing the angle of the evaporation source, see Figure 23a.

It is also possible to manipulate material through the mask, e.g., by sputter etching. Structures of different sizes can be piled on top of each other in a much more elegant way than it is possible when using only cracks. Apparently, as there is no contact of the shadow mask with side walls well-defined structures are possible. Figure 23b illustrates the negative influence of side-walls, which provide a further deposition zone, and thus make the mask lift-off difficult.

Furthermore, there are also severe disadvantages when using the shadow mask technique if it is not applied in combination with the thin film fracture approach. A typical problem is to find a good alignment of the mask. The schematic drawing of a shadow mask setup is shown in Figure 23c. The size of the nanostructure calculated from the simple geometry of the setup is given by (118);

$$s \approx d + \frac{w}{l} h \tag{2.12}$$

The broadening of the structure represented by the second term in this equation points out the difficulty in working with the shadow mask approach. Generally, for the commonly available vacuum chambers the source width w and sample source distance l are fixed (e.g., l = 0.2 m, w = 2 mm). These considerations imply that the distance h of the shadow mask above the surface should be less than a micrometer, if broadening of the desired structures is to be kept below 10 nm. Further disadvantage posed by the shadow mask approach is in the form of the costly nanostructuring involved in the fabrication of such a mask. This often limits the shadow mask approach to small areas.

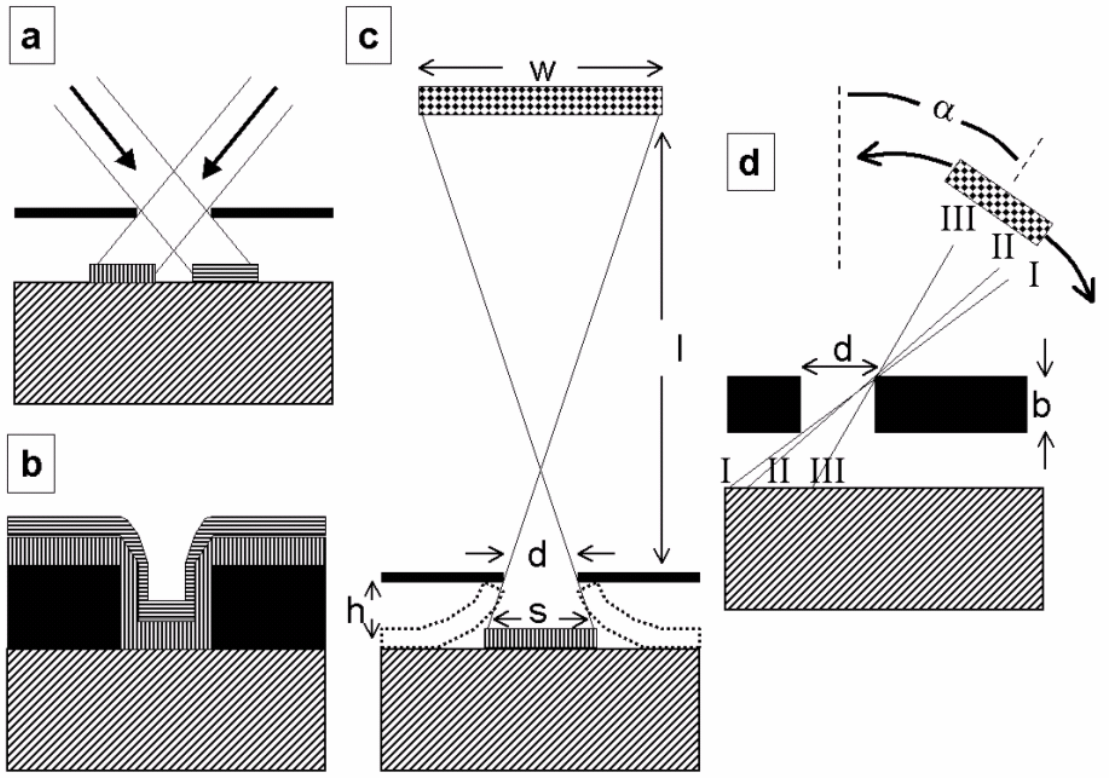

Figure 23: Sketch illustrating the principle of the shadow mask approach. a) Aperture effect of a pinhole to deposit different materials next to each other. b) Deposition of material in thin film channels creates the difficulty of side wall deposition which might hinder a proper structuring and mask lift off. c) Path of the deposited material for the shadow mask approach. A deposition source of the width w in the distance l from a shadow mask with an opening of the size d and the high h above the surface will create a deposition area on the surface of the size s. d) The effect of angular deposition under angle a through a shadow mask of thickness b. Lines I, II and III illustrate different incident angles for the material. If the source is around line I, the obtained structure width on the substrate is significantly reduced and can be smaller than the width d of the opening.

The above mentioned disadvantages of the two individual techniques can be overcome by combining both approaches into a new approach where the individual advantages of both are retained. Such a combination can be done by going beyond thin film fracture and being even more "destructive". Adding delamination at the crack sides produces an arrangement which can be used as a shadow mask (shown by dashed lines), see Figure 23c. A film under tensile stress may debond from the root of a channel crack. In general, crack debonding occurs at the interface when the driving force G equals the crack resistance at the interface Γi. On this basis, design rules exist to prevent delamination. However, a universal formula which can describe the delamination completely appears difficult to reach, as real materials can exhibit local inhomogeneity, plastic deformations and very complex microstructures. Experimentally, the thickness of the thin film and the amount of stress has to be adjusted individually in order to create a suitable opening and a sufficiently wide delaminated zone. The combination of both approaches allows depositing nanowires with diameters smaller than the opening d of the

delaminated crack. This is possible by employing angular deposition, as illustrated with the help of a simplified sketch in Figure 23d. In this case, the thickness of the delaminated thin film mask is also considered, which is shown schematically as a shadow mask of thickness b and opening d. The three lines I-III show possible pathways of incident matter at different angles. If the whole source (width w) is tilted to a large angle such that its left end passes line I, no material can reach the substrate. By tilting to slightly smaller angles with the left end of the source at the end of line II, structure widths, much smaller than the opening d can be realized (see separation between line I and II on the substrate). Further tilting of the left end towards the end of line III leads than to a significant broadening of the deposited structure. The angle of line I, around which the size reduction takes place, is approximately $\alpha=\arctan(d/b)$. Around this critical angle, the source size has little influence on the width of the resulting structure. Hence, usually experiments mentioned below were performed by positioning the sputter source at an angle of typically 45° to the sample normal.

The combination of delamination and cracking can be illustrated as follows: A typical delaminated photoresist thin film is shown in Figure 24a .

Here, the delaminated cracks have been generated by uniaxial bending of the substrate, which is a stainless steel foil. A further widening of the crack was done subsequent to metal (Ag) sputter deposition. This was realized by further bending and a partial removal of the photoresist thin film by acetone. The condition that the walls of the crack do not touch the wire directly as illustrated before has been beneficially employed. Accordingly, the nanowire that was formed in the delaminated crack could be seen through the widened opening. Figure 24b illustrates an application of the combined fracture shadow mask process (shown earlier schematically in Figure 23d) during deposition. Parallel gold nanowires are deposited on the silicon substrate within a separation distance of just 150 nm. The magnification in Figure 24c shows the tiny dimensions of the ensemble with a gap of 150 nm. Au deposition was carried out twice, under different angles of 45° and -45° with respect to the surface normal. The obtained wires are parallel even on macroscopic dimensions.

This approach can be used further to form parallel wires of different materials, as demonstrated in Figure 25a. To visualize the flexibility of such an approach, a polymer substrate has been used , and two wires of different material, Cu and Au, have been deposited with a nanoscale gap of less than 50 nm between them (as determined by calibrating the SEM at step edges) .

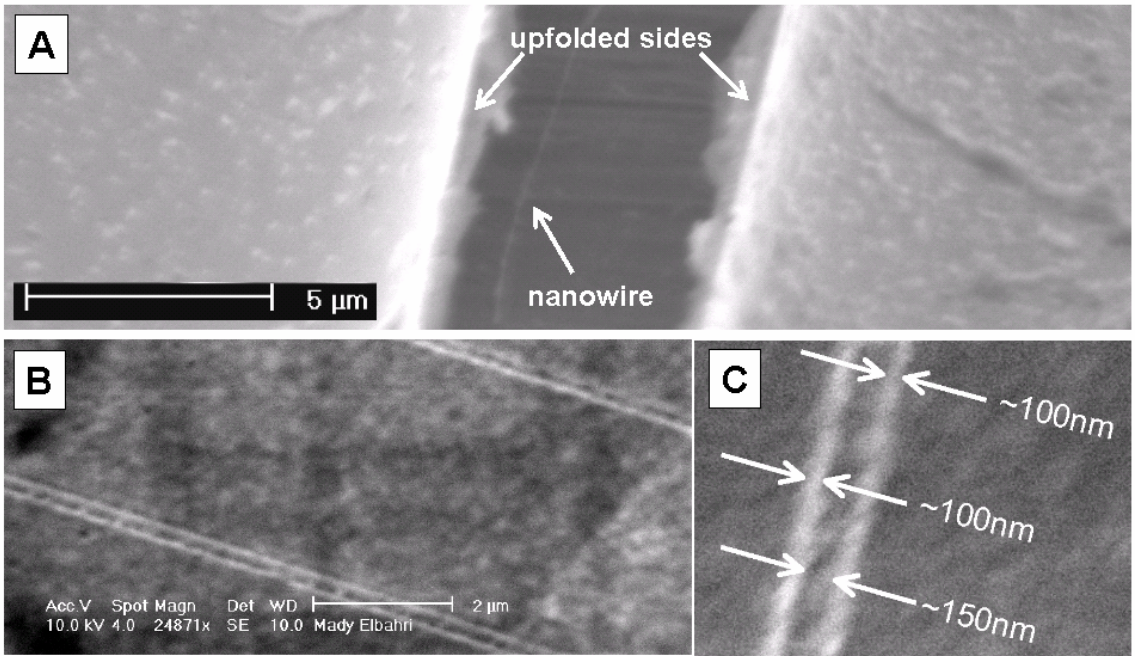

Figure 24: *Nanowires and nanogap formed with the help of delaminated thin films. A) Illustration of the principle, Ag nanowire on stainless steel foil substrate under delaminated photoresist covered with silver. B) Part of an array of parallel Au nanowires on a silicon substrate, C) magnification of a, nanowires are well separated with a 150 nm gap.*

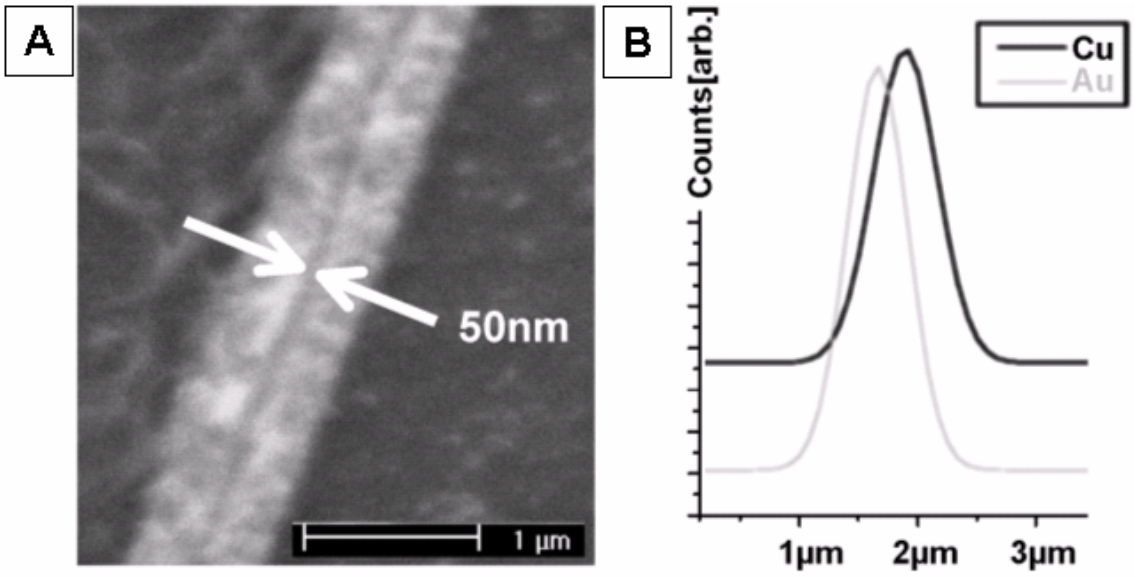

Figure 25: Nanogap between (Cu) and (Au) wire on polymer substrate: A) geometry, B) Gaussian fit of an EDX line scan shows the different materials of the wires.

The Cu and Au wires obtained in this case are broader due to a small incident angle of angles of 10° and -10°. The broadness of the wires facilitates the determination of material composition using EDX line scan, as shown in Figure 25b. Due to the low signal, a Gaussian fit was done for curves, showing the separation into the Cu wire (lower right) and Au wire (upper left).

2.4.4 Integration into Lithography

A microstructured thin film can contain predetermined breaking points. This is a chance to introduce nanoscale cracks into standard microstructures crated by lithography like photolithography on a ridged substrate like silicon.

Stress can be intentionally introduced by choosing appropriate thin film geometry. The strain fields which cause the cracks can be controlled by the microscopic geometry of the thin film. For this purpose several microstructured films are designed by conventional lithography in collaboration with Dr. Berndt Schmidt, Rossendorf. Structuring is prepared on 100 nm SiO_2 coated Silicon substrate by using "Shipley Lack S 1813" photoresist, used together with an adhesion promoter (closed system). All wafers were exposed to UV light overnight. Cracks formed by thermal cycling, it was heated to a temperature around 90 °C and held there for 45 minutes on the hot plate then exposed to VLN_2 for 3 minutes. Figure 26 (a-d) gives an example for that approach. The film has a form of a bow tie. Applying stress to this structure leads to mechanical failure at the weakest point; a crack occurs right in the middle of both trapezes (b).

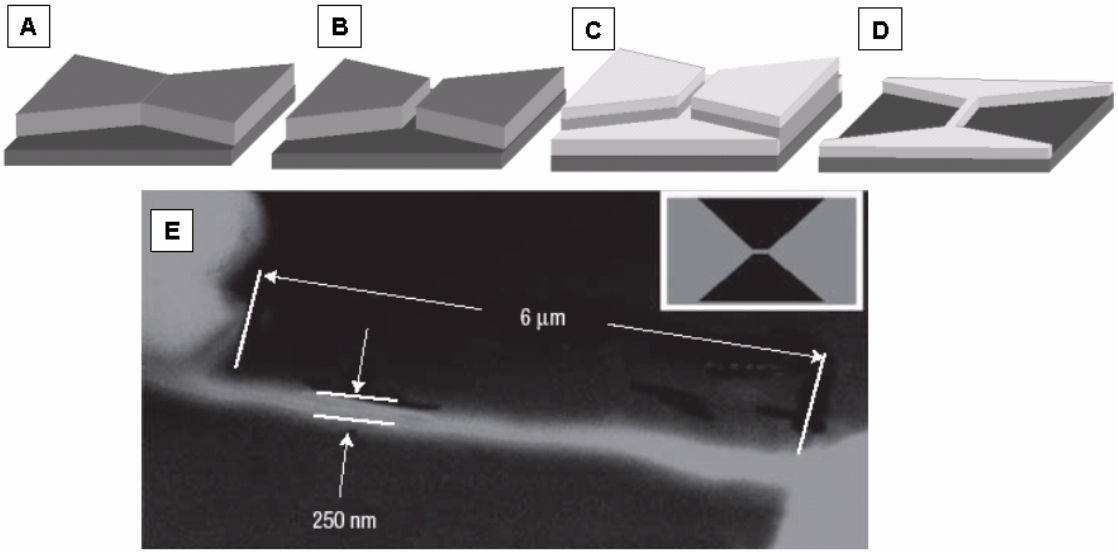

Figure 26: Different process steps for cracking a micro-structured thin film, A) will be exposed to stress, that it fractures, B) along a predetermined breaking line, C) Onto this, the material out of which the wire will be made is deposited, D) By removing the thin film together with the excess material deposited, the desired nanostructure will be obtained (here). E) a wire between two contact pads.

A wire between contacts is realized by deposition (c), and mask lift off (d). A SEM image, Figure 26e, shows the realization of a one step device using bow-tie approach after metal deposition and mask lift off. The advantage of this particular structure is that the wire forms simultaneously with macroscopic contacts in an organized manner.

Another interesting phenomenon was observed for other wafers containing rectangular structures connected with channels as seen in Figure 27a.

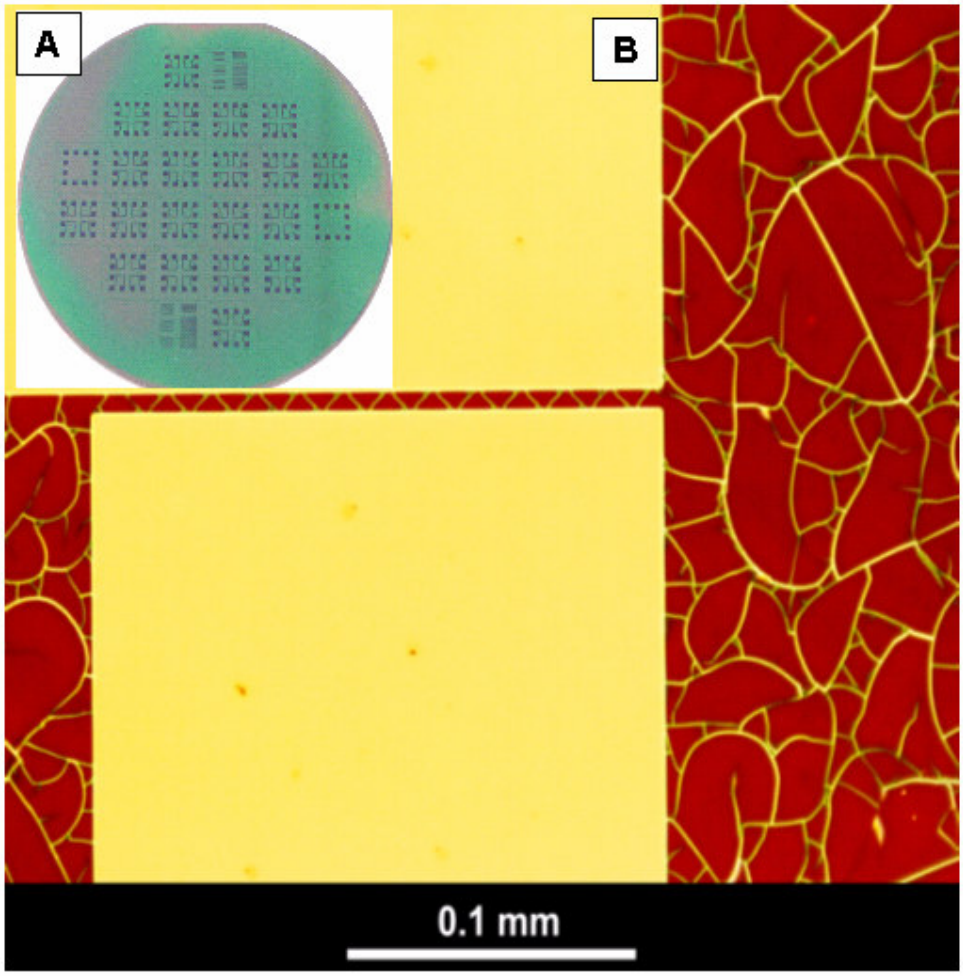

Figure 27: *Cracks on structured microchip: A) Microchip containing rectangular and channel structures, B) Different cracks sizes and order, random and thicker cracks in the rectangular area, while ordered zigzag and thinner cracks are found in the channel.*

Interestingly, two types of fractures can be observed, see Figure 27b. Cracks inside the rectangular area show the dried-mud pattern with disorder structures. In contrast to that a zigzag like fashion in a well organized pattern is observed inside the channel. Recently it was shown, that the worm like structure results from non-linear deformation and in plane bi-axial compression of the film ([119]). Biaxial compression accounts for the thermal film stress driving delamination and leads to buckling and post buckling instabilities. The compression applied on the edges of the plate has a destabilizing effect.

The plate of the film tends to buckle away from its rest plane and bends to recover its normal length. Buckling therefore results from a balance between the release of the in-plane compression energy and gain of bending energy, this balance gives rise to many buckling bifurcations. In the case of buckling,

the mechanism of self ordering leads to the well aligned periodic structure and in the case of fracture, a similar mechanism is responsible. If the stored elastic energy in the film is greater than a critical energy, then both delaminating and fracture will occur simultaneously, (see 2.2.2) resulting in a periodic fracture pattern.

Figure 28a shows a SEM image with cracks in a well arranged zigzag pattern. By partial mask lift off, seen in Figure 28b, one can observe that, the wires have obtained a similar zigzag fashion. Figure 29c shows, how the wires are connected end to end within a 200 µm length and 10 µm width channel, resulting in 20 wires per channel. This structure utilizes a failure tolerance device where a damaged wire within the zigzag lines has no impact on the conductivity of the device.

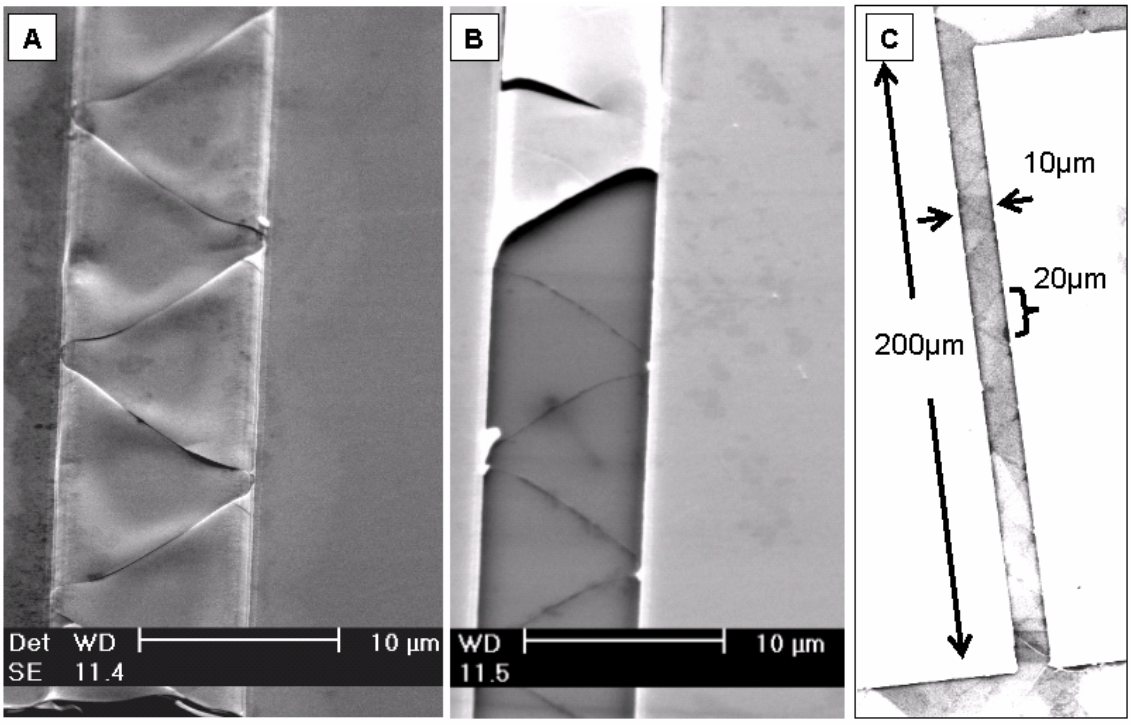

Figure 28: SEM shows the Zigzag fashion of the cracks and the wires. A) Patterned delamination and fracture of zigzag, B) Partial mask lift off showing a similar pattern of the wires. C) End to end connected wires in the channels.

2.5 Fracture Approach--Summary and Outlook

A new template approach for the generation of well-defined nanowire network structures that can be used on almost any solid material up to macroscopic sample sizes in a cost-effective manner is described here. Thin film cracks used as a template enables one to demonstrate the production of networks or single nanowires with diameters of less than 40 nm, while the length of individual wires can have macroscopic dimensions. Neither the wire materials nor a significant restriction in the selection of substrates limits our approach. This, however, is limited by at least two factors: first, diffusion of the deposited material on the substrate could lead to the broadening of wires; second, the quality of the deposited nanowires depends to a large degree on the quality of the thin film fracture.

In spite of this approach, nanowires below 40 nm are demonstrated without further optimization. Examples for the generation of different wire materials on different substrates are also given. This includes Pt nanowires on Nafion or Ag and Au nanowires on glass, silicon and even more Ag/Teflon nanocomposite on commercial household foil.

Also, a simple method to obtain well-aligned nano-shadow masks on different substrates is presented. The method is used for creating templates by combining the shadow mask approach with the controlled thin film fracture and delamination. The typically unwanted effect of thin film delamination is used to an advantage in this process. The difficulties like alignment of the mask on the surface or close control of its distance from the substrate faced while working with shadow masks have been overcome by using delaminated cracks. Advantages of the “fracture approach” have been successfully combined with advantages of the “nano-shadow mask” approach. Such a judicious combination employs two size reduction effects. The microstructure induces cracks on the nanoscale when a film thickness in the submicron range is chosen. Therefore to obtain nanowires even smaller than these openings, evaporation can be carried out around a critical angle that can theoretically reduce the width of the obtained nanowires down to single atoms. Disadvantages of the individual techniques, like the inability to fabricate adjacent structures, the difficulty in fabrication and placement of the mask within a small distance of the surface and their orientation have been overcome by the combined approach. In spite of this, side-by-side parallel nanowires with a nanogap of less than 50 nm are demonstrated. Further examples were shown also demonstrating sufficient control of the process for efficient nanostructuring and provide a glimpse of the possibilities of this approach.

The advantages of cracks, i.e. their straight alignment, the scalability down to the nanometer size and their natural ability to be oriented by microstructures via strain are employed to align patterns by different ways. Even more nanowires with individual macroscopic contacts can be fabricated together in one step with this approach. The frequently occurring contact problems do not take place here.

Integration of the fracture approach into microstructures is also possible. A regular pattern of nanowires with zigzag-like fashion is formed within a microstructured channel.

However, this part is now under further investigation (120). Primary results indicate a dependence of the zigzag pattern on the channel width. Furthermore, integration of such circuits that can be used for sensor application is also going on. The primary results show a significant sensitivity of Pd or even Au nanowires to H_2 gas. Electrical and magnetic properties of the nanowires are also planned to be investigated.

This part is dedicated to my wife and my son Bilal as I got the idea while making some pancake together in our kitchen. At this moment I started the so called water based hot plate for nanosynthesis and nanopatterning. A part of this research is included here.

3 Nanowires using the Drop Approach

3.1 Introduction

There has been considerable interest in systems that spontaneously organize into predictable surface patterns (121). Nonlithographic techniques leading to controllable and potentially functional structures occupy a fundamental niche in modern materials science. If a droplet of macroscopic, non-passivated colloid suspension is dried slowly on a surface such as glass, a ring pattern is formed. The particles aggregate at the rim of the droplet because of attractive capillary forces between the particles when the water film thickness of the dimension of the particle diameter. The mobility of the particles is lost after complete drying, suggesting a three-step mechanism for the particle adsorption. First positioning and adhesion in the suspension liquid are controlled by charge and polar interactions between the substrate and particle surfaces. In the second step, capillary forces between the particles and the surface laterally displace the particles during drying. After complete evaporation in the third stage an irreversible reorganization of the particle-substrate interface occurs, which prevents resuspension or displacement when resubmerging the assembly into the adsorption liquid.

The history of publications in the ring formation goes back to Denkov et al (122) who analytically described the mechanism of particles accumulation at the rim by the capillary effect existing between the particles. A series of publications by Deegan et al (123,124,125) presented physical explanations of colloidal fluid evaporation and ring formation and growth in daily occurring events, such as a coffee ring stain. Deegan explained that the ring is produced because the contact line is pinned, and so solvent lost by evaporation at the droplet's edge must be replaced by solvent drawn from the interior. The flow that brings fluid from the center to the edge of the droplet also carries solute, which is deposited at the edge. He supported this mechanism by an analysis of the height-averaged velocity field, and its effect on particle deposition, assuming rapid vertical diffusion of particles across the height of the droplet and adhesion of the particles onto the substrate.

Ring deposition of particles from colloidal dispersion upon drying of droplet has been introduced. It has been shown that barium ferrite nanoparticles can self-assemble in the "Olympic Rings" (126) (intersecting rings, ring diameter 0.6-5 μm). The mechanism of ring building was explained by hole formation in an evaporating thin film as well as interparticle dipolar interactions. Ring like structures which self assemble from a solution of nanometer-sized metal particles on a solid substrate with a diameter of 0.1-1 μm were formed during the drying process (127). A formation of magnetic ring using Co nanoparticles is also shown (128). Recently Xu et al (129 and references therein) shows well organized concentric micrometer rings (ring width 5-0.6 μm) of polymer and semiconductors through the solvent evaporation process using a sphere-on-flat geometry combined with repetitive stick-slip motion under the control of a motor. But even with this significant progress, drying-approach still faces certain challenges which can be summarized as follow; a) The end structures are mostly in the

micrometer range even if nanometer building blocks are used, b) This approach is mostly restricted to a ring geometry and other geometries like wire, chain arrays are rare, c) The approach is limited to a suspension/colloidal solution.

It turns out that an approach that works with many different materials and allowing the structures to be aligned down to the nanoscale in a different geometry is a challenge.

In contrast to the "cold drop" discussed above, here, the drop is dried on a hot plate.

Drying of a liquid on a hot surface consists of several regimes which are determined by the heat transfer between them. This fact was utilized, 73 years ago by Nukiyama (130), who demonstrated that at atmospheric pressure there are a maximum and a minimum value of heat transfers in the water-boiling curve. Accordingly, the heat transfer regimes are classified as follows:

a) Film evaporation regime for $T_s < T_b$ b) Nucleate-boiling at $T_s \geq T_b$

c) Transition regime at $T_s >> T_b$ with a d) Film boiling regime for $T_s > >> T_b$

where T_s is the temperature of the hot surface and T_b is the boiling temperature of the liquid. These regimes are also sketched in Figure 1.

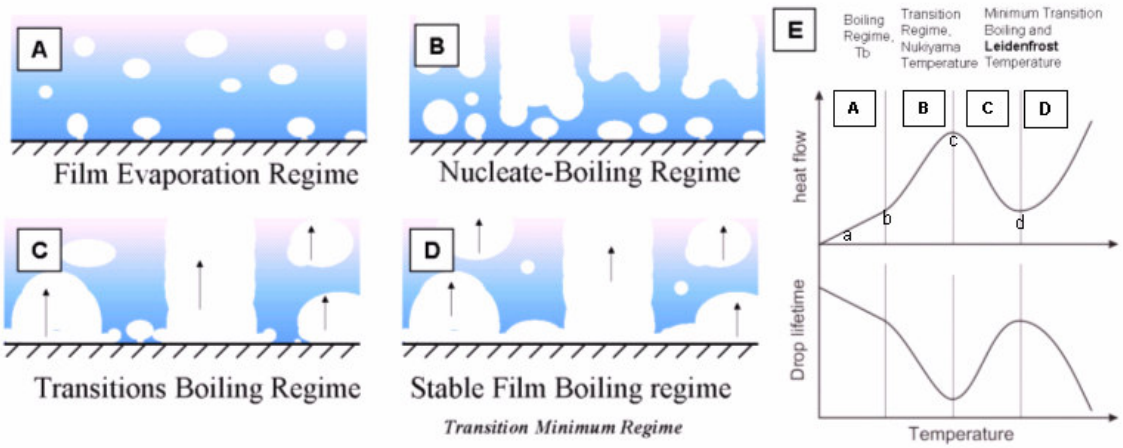

Figure 1: A-D) Schematic showing the heat transfer regimes, E) Schematic showing the dependence of heat flux and drop life time on temperature.

The lifetime of a droplet of a volatile liquid placed upon a hot surface is in fact not a monotonous function of the temperature, whilst the drop lifetime diminishes at temperatures equal to its boiling point. The dependence of the total vaporization time of drop (drop life time) on the temperature of the hot surface T_s is explained (131) by the film boiling phenomena.

A typical curve illustrating the dependence of a drop life time on the temperature of the hot surface T_S and its corresponding pool boiling curve is sketched in Figure 1e.

When T_S is far below the boiling temperature of the liquid drop T_b, the drop evaporates slowly due to molecules escaping from its surface. However, when T_S approaches to T_b heat is transferred from the hot surface to the drop by convection and subsequently the drop life time decreases. This part is illustrated by the range a-b which is called liquid film type vaporization regime. At point b when T_S, is equal to T_b nucleate boiling is observed and bubbles/slugs arise in the central part of the drop with a further decrease in the total life time until a minimum life time is observed at point c. This point is called Critical heat flux (CHF) and characterised by a rash evaporation of the liquid drop with maximum boiling rate. The temperature at this point is known as "Nukiyama temperature" and defines the departure from nucleate-boiling regime. Slightly above Nukiyama temperature a regime known as Transition boiling begins in the range c-d. The frequency of contact between the drop and the heated surface decreases and the time required for complete vaporization starts to increases. This indicates a decrease in the rate of heat transfer from the heated surface to the drop which is caused by the formation of a partial vapor film between the drop and the hot surface. The drop lifetime continues to increase with the temperature until a maximum at point d. This point d indicates the disruption of contact between the drop and the heated surface due to the formation of a stable vapor film. The encapsulated vapor film between the liquid drop or liquid film and the hot wall causes heat transfer degradation where a minimum heat flux point (MHF) is reached. The drop starts to dance on its own vapor, the Leidenfrost temperature is reached. Note that the water under Leidenfrost has now two interfaces, air/water "cold interface" and water/vapour "hot interface". Furthermore, the minimum heat flux point is a metastable state, so if the hot wall temperature does not increase further, a vapour film collapse and a shift to the evaporation/boiling regimes occurs. The collapse of the vapour film occurs by subcooling effect. Subsequent increase of T_S beyond the point d causes the total evaporation time decreases slowly as shown by the curve which is called the Film-Boiling regime.

However, in this part, the patterning using a drop on a hot plate was investigated at two temperatures, namely @ 80 °C (evaporation regime) and @ 230 °C (the transition minimum, the Leidenfrost one). Accordingly drops are classified into two types:

"Hot drop" for drying @ 80 °C & "Superhot drop" @ 230 °C.

In most of the studies in this field pre-existing particles have been used. In contrast to that, an aqueous drop is utilized here. Firstly, the solute has to be deposited than the solute has to be transformed into the desired material by a chemical reaction.

3.2 Basic Aspects of Liquid Drops on a Surface

3.2.1 Wetting

Some of the most important chemical and physical processes occur at a surface or interface. The surface of a medium whether it is a liquid or a solid has very special properties which are often quite distinct from the bulk substance. The broken symmetry at the surface gives rise to altered interaction forces (132). As illustrated in Figure 2a, bulk atom/molecule benefits from the interaction with all neighbours and finds itself in an energetic favourable state. By contrast, surface molecule/atom finds themselves in a higher energetic state as they have lost some of the interaction partners. This symmetry perturbation is responsible for the special behaviour of the surface and leads to anomalous phenomena (e.g. wetting).

Wetting refers to how a liquid deposited on a solid (or liquid) substrate spreads out. When a small liquid droplet is put in contact with a solid several phenomena can be observed, which depend on the surface tension/energy of liquid/solid. If the liquid shows a high surface tension (strong internal bonds) compared to the surface to be wetted, it will form a droplet, whereas a liquid with low surface tension will spread out over a greater area (bonding to the surface). On the other hand, a drop will wet a high surface energy surface and form a cap on surfaces possessing low surface energy. The driving force behind the phenomenon is the minimization of interfacial energy.

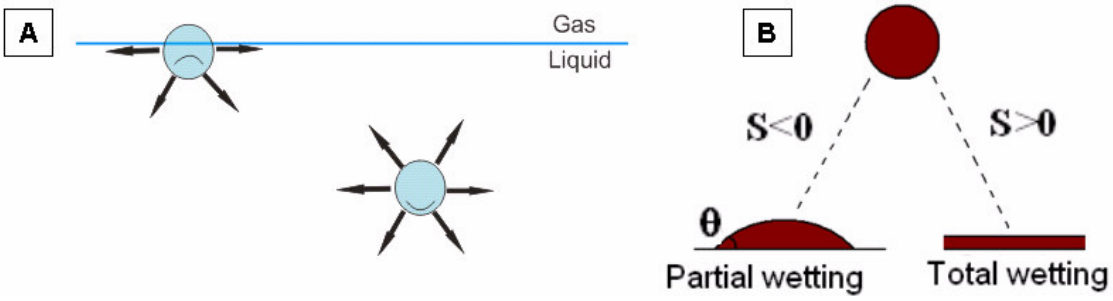

Figure 2: A) A "happy" molecule in bulk: it benefits from interactions with all its neighbours, whereas molecule at surface is "unhappy", B)Two wetting regimes for a drop according to the spreading parameter "S".

3.2.2 Spreading Parameter (S)

There are two regimes of wetting namely partial or complete wetting. The parameter that distinguishes them is called spreading parameter S, which is the measures for the difference between the surface energy (per unit area) of the substrate when dry and wet:

$$S = [E_{substrate}]_{dry} - [E_{substrate}]_{wet} \quad (3.1)$$

or $$S = \gamma_{SO} - (\gamma_{SL} + \gamma) \quad (3.2)$$

where, γ is the liquid-vapor energy (i.e. the surface tension), γ_{SL} the solid-liquid interfacial energy and γ_{SO} the solid-vapor interfacial energy (mN/m). According to the S value a complete or partial wetting can occur; $S > O \rightarrow$ Complete wetting, $S < O \rightarrow$ Partial wetting

As illustrated in Figure 2b, in the partial wetting regime the drop forms a spherical cap on the substrate with a contact angle θ_E. at equilibrium. The liquid/vapour interface meets the solid surface and defines the contact line. According to the contact angle described by Young, water droplets will exhibit contact angles of $< 90°$ on a hydrophilic surfaces, whereas on highly hydrophobic surfaces contact angles are observed to be $> 90°$. At equilibrium, the chemical potential in the three phases should be equal and the Young equation is satisfied where,

$$\gamma \cos \theta_E = \gamma_{SO} - \gamma_{SL} \quad (3.3)$$

3.2.3 Capillary Length and Meniscus

There exists a particular length beyond which gravity becomes important, namely, the capillary length (κ^{-1}) , which is determined by: $\kappa^{-1} = \sqrt{\frac{\gamma}{\rho g}}$, where, γ is the surface tension of liquid, ρ is the liquid density and g is gravity. Placing a small object on an initially horizontal liquid surface will cause a perturbation. The surface perturbation induced on the liquid surface diminshes exponentially with distance with a characteristic length, which is the capillary length. A liquid placed in the vicinity of a wall will be disturbed so that, when the liquid is wetting, it rises slightly near the wall, whereas when it is non-wetting, it drops. The meniscus is the region where the liquid surface is curved.

3.2.4 Lotus- Effect and Self-Cleaning

Adding roughness to a hydrophobic surface results in superhydrophobic material. Superhydrophobic surfaces have contact angles greater than 150° and show almost no contact between the liquid drop and the surface “drop above an air-blown porous surface”. This is sometimes referred to as the "Lotus-Effect". The self-cleaning property of Lotus leaf is a phenomenon achievable by rolling a water droplet on a superhydrophobic surface. If the surface contains contaminations, e.g., dust particles, the particles will be removed from the surface if the absorption of the particles into the water drop is higher than the static friction force between the particles and the surface. The primary condition for removing dust is a drop rolling where a sliding drop will cause a surface contamination to be deposited on the surface.

The behaviour of a drop on a superhydrophobic surface is similar to the levitation of a drop above a hot plate by the so called “Leidenfrost phenomenon”, a phenomenon discussed in the next part. This

similarity can be seen in Figure 3. Other than the Lotus effect, which implies a non-wettable ”Superhydrophobic surface”, a Leidenfrost droplet can have the same shape on a hydrophilic surface.

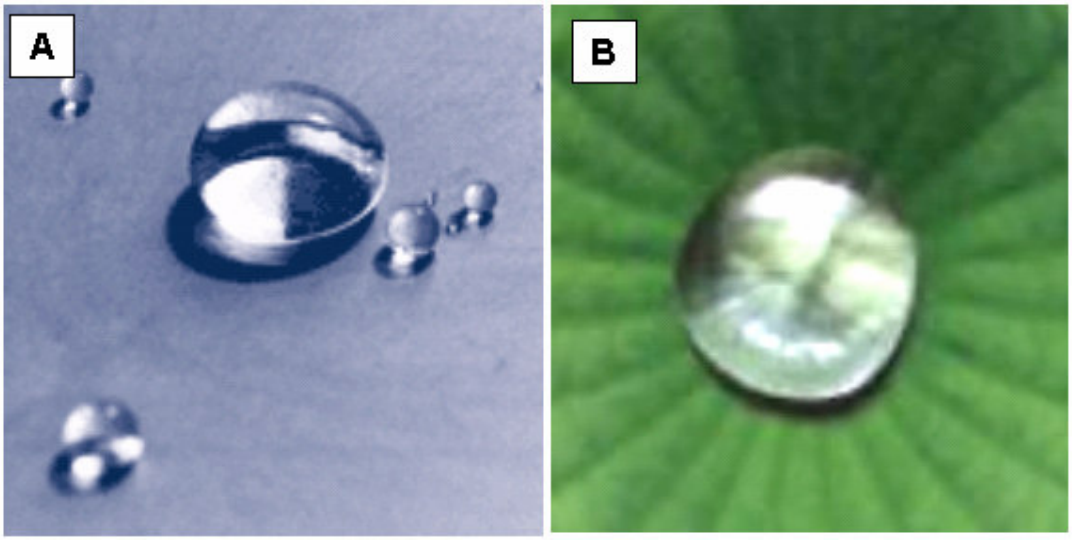

Figure 3: Images show water droplets with spherical shapes. A) A water drop on a hot plate at the Leidenfrost temperature, B) A water droplet on “Lotus leaf “a superhydrophobic surface. (Wikipedia, the free encyclopedia).

3.2.5 Leidenfrost-Phenomena

“An iron spoon of any size, well polished within and free from rust and dirt, is heated over glowing coals until it glows with light. To this glowing spoon, removed from the coals … one drop of very pure distilled water...Moreover, however this drop only evaporates very slowly. For if you turn to a pendulum indicating seconds with its oscillations, at least 34 or 35 seconds, that it runs a little over half a minute of an hour before the whole drop disappears. Which at last exceedingly diminished so that it can hardly any more be seen, with an audible crack, which with the ears one easily hears, it finishes its existence, and in the spoon it leaves a small particle of earth.....”

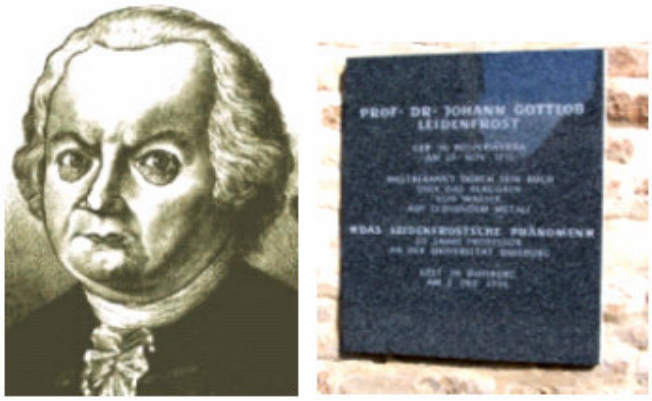

Figure 4: An image and plaque of Prof. Dr. J. G. Leidenfrost (Wikipedia, the free encyclopaedia).

Heat is transferred to droplet by conduction through the vapor film on the bottom half and by radiation to the entire droplet. Mass is removed from the droplet by evaporation on the lower surface to supply

265 years ago Johann Gottlob Leidenfrost (1715-1794) published a comprehensive article titled “De Aquae Communis Nonnullis Qualitatibus Tractatus”, which shows the behaviour of a water drop on a hot plate.

Initially, as the temperature of the plate is below 100 °C, the water just flattens out and slowly evaporates. As the temperature goes above 100 °C, the water drops hiss on touching the plate and evaporate relatively quick. As the temperature goes past 200 °C, however, the droplet of water does not evaporate quickly. The droplet dances on the hot plate for a while before it vanishes.

When water touches the hot plate, the bottom part of the water vaporizes immediately. The drop is not any more in contact with the solid but levitates above its own vapour. The temperature, at which the drop dances and generally the levitation phenomena occur, is named after Leidenfrost.

the vapor film and by diffusion from the upper surface. The droplet is supported by the excess pressure in the vapor film and levitates on its own vapour (133).

This phenomenon has long been regarded as an interesting curiosity having little or no significant applications. It has also been used in some dangerous demonstrations, such as dipping a wet finger in molten lead and blowing out a mouthful of liquid nitrogen, both enacted without injury to the demonstrator. The effect is also responsible for the ability of liquid nitrogen to skitter across lab floors (134). Indeed, it is only now that realization of the scientific potential behind the Leidenfrost effect begins (135). Here it will be demonstrated that the Leidenfrost effect can be used in nanotechnology. Drop levitate on its own vapor is a mobile chemical reactor, where nanoparticles synthesis and self organization can occur in one step ([1]).

3.2.6 Drop Impact

The liquid drop/solid surface interaction has been studied for more than 125 years (136) and the fascinating hydrodynamics involved still interest a lot of researchers. Even though, much research has been done in this field, because of it is of importance in spry cooling (137,138), this process is complicated and not yet completely understood (139). The interplay of several parameters like drop size, velocity of the drop, chemical composition, surface geometry, temperature and such other parameters have a considerable influence on the resulting structure.

Interfacial forces, viscous forces and capillary forces are the three basic forces governing the behaviour of droplet on a surface. The interfacial force which can be determined by the droplet size, velocity of impact and density of liquid, has a direct influence on droplet spreading on the surface. The deformation of the droplet on the surface is governed by the capillary force and the viscous dissipation

[1] M. Elbahri, R. Adelung, D. Paretkar. PCT/DE2006002066.

which is governed by the fluid viscosity. The competition between these various forces is described by the dimensionless quantity known as capillary number and can be seen as interplay between forces which govern the drop mobility and the others resisting that behaviour.

Alternatively the capillary number can be expressed as simply the ratio of Weber number and Reynolds number. Weber number represents the competition between the inertia and the surface tension. While the Reynolds number represents the competition between the inertia and viscous dissipation.

Upon impact of a droplet on a hydrophilic surface (attractive interaction); the kinetic energy will force the drop to expand to a certain diameter, which is limited by the viscosity and surface tension. At equilibrium a pancake shape is established. By impact on a hot surface, the situation becomes more complicated. According to the wall temperature and We-number several regimes can be found. The four main regimes observed on a hydrophilic surface are; deposition, splashing, disintegration and rebound (140).The deposition regime occurs when both the Weber number and the wall temperature is low. If the velocity of the incident drop is small, the drop has not enough kinetic energy to leave the surface and therefore will stick on it. This scenario will occur if the temperature of the wall is below the saturation temperature of the liquid (i.e. evaporation regime). By increasing the drop velocity the drop is flattened to a thin film, however, the surface tension is not large enough to ensure drop cohesion. Increasing the temperature of the wall the other regimes namely, splashing and disintegration begin to appear. Splashing happens when the wall is heated up close to the liquid saturation temperature or slightly above. Small bubbles are formed (i.e. bubble boiling), as a consequence the well known star shape appear. The splashing behaviour will continue for higher temperatures until a certain temperature is reached where a drop explosion occurs and secondary droplets are generated which is called the disintegration state.

The disintegration behaviour characterizes the transition regime. The number and size of the secondary droplets depend on the impingement velocity. The higher the Weber number, the smaller the droplet size and the higher the droplets generated.

If the secondary drop possesses a low kinetic energy, the vapour cushion between the drop and the wall acts as a shock absorber and the drop keeps enough energy to retain a spherical shape and get away from the surface, e.g., by rebounding. Thus in contrast to rebounding that can occur at hydrophobic surfaces which need high kinetic energy, the rebound regime exists here by restrictive conditions: the incident velocity (i.e. Weber number) must be very low, but the wall temperature must be relatively high.

3.3 Fabrication Technique

Fabrication of nanostructure by using the drop approach requires in general not more than, a pipette, a glassware containing the solution/suspension of the desired material, a hotplate, and a silicon wafer, see Figure 5. The experimental procedures for the fabrication of the structures were carried out as described below.

Figure 5: Requirement for drop based nanostructuring.

3.3.1 Substrate Preparation

Commercial silicon species (1-2 x 1-2 cm^2) are usually cleaned by air-blow and then cleaned with isopropanol by ultrasonication for 30 minutes and subsequently dried in air.

3.3.2 Solution /Suspension Preparation

All the glassware used in the preparation of the solutions was cleaned for 3 minutes in an ultrasonic bath using acetone and then completely dried in air before use.

Fresh solutions of the desired material, here, Zinc acetate [$Zn(CH_3COOH)_2$, (99.99 %, Sigma–Aldrich, Schnelldorf, Germany], and Silver nitrate [$AgNO_3$, (99,99995%, provided from Alfa Aeser,

Karlsruhe, Germany)] is firstly prepared as 0.1 M solution then diluted to the desired concentrations using the dilution formula:

$$M_{conc.} V_{conc.} = M_{dil.} V_{dil.} \quad (3.4)$$

However, to ensure that the physical properties of the salt solution are like the pure water, only concentrations in the range of 10^{-3}-10^{-5} M are used here.

Furthermore, other materials like, silver nanopowder, ([Ag, 100 nm, weight ratio 1:150], 99.95 %, from Sigma–Aldrich, Schnelldorf, Germany), as well as zinc oxide powder ([ZnO, weight ratio 1:150], 99.99 %, Sigma–Aldrich, Schnelldorf, Germany are also used.

3.3.3 Procedure

In general, a single drop with an initial volume of 50-75 µl forming a ~7-10 mm diameter spherical cap on a surface is placed on the hot substrate. As different techniques are used here regarding drop patterning, more details about the experimental parts for each process will be given with the results and discussions.

After complete drying the pattern was examined with the aid of an optical microscope, and scanning electron microscope (SEM) and in some cases with the atomic force microscope (AFM).

3.4 Results and Discussion

3.4.1 Evaporation of a Hot Drop

The so called coffee-drop deposit phenomenon is not particular to coffee. Mineral rings left on washed glassware, banded deposits of salt on the sidewalk during winter and enhanced edges in water color paintings are some examples, which show a similar behaviour.

Deegan explained why a ring is formed and postulates that the evaporation of a cold drop will form a single ring.

However, here, the pattern formed by using a hot drop (75µl, 10-5M, AgNO3) as well as the cold drop for comparison is investigated and shown in Figure 6. For the cold drop the evaporation time was found to be in the range of one hour. It was observed that the drop remained pinned most of its drying time (~ 75% of it), before the contact line started to move. As a result, a single outer ring followed by additional irregular and discontinuous structures in the interior are formed as shown in the optical image in Figure 6a,b respectively. This behaviour indicates a depinning event occurring with the cold drop at a late stage of the evaporation. In contrast to the cold drop, the hot drop shows a shorter pinning time at the start, than retraction and thinning, followed by a rapid motion of the contact line. The evaporation time was found to be in the range of 1 minute. The pattern obtained by the hot drop was characterized by the formation of intersecting rings followed by multiple continuous rings, as seen in the optical image in Figure 6c,d respectively. The consecutive deposition and retraction cycles of the contact line result in the observed rings. Thicker and thinner rings are observed which suggest a random movement as well as different pinning times of the contact line. It is worth mentioning, that the dried patterns for different solute in the whole range of dilutions (concentrations, 10^{-5}-10^{-3}M) show almost the same features.

The behaviour of the cold and hot drops shows some similarities regarding the depinning effect. However the hot drops show a high density of well separated rings whereas in the cold drops the rings are lacy, discontinuous and appear only at the end stages of the evaporation.

Indeed the difficulty to get a ring by a cold droplet and in general the patterning using a drop is also stated by several authors: Bediwi et al.(141) report on the difficulties of obtaining a uniform deposit, Adachi et al.(142) shows lacy like concentric rings which can be explained through a stick-slip motion of the contact line caused by particles deposited on the surface. Parisse et al. (143) observed a sol-gel transition of polymer solute at the boundary. When the thermocapillary forces influence the assembling process during solvent evaporation, diverse microstructures such as polygonal networks in the interior of the drop are formed. This effect was explained by the involvement of dispersed nanoparticles to convection flows due to evaporation (144). The so-called Marangoni convection gives

rise to hexagonal honeycomb (145) networks and/or interior ring or even thin film by inward flow (146).The authors attribute the difficulty of the patterning using a drop to several factors like, the liquid surface tension and diffusion of vapor in air (147), concentration (148), particle size (149), ionic strength (150), surfactants (151), solvent-solute interactions (152), and hydrodynamic instability (153,154).

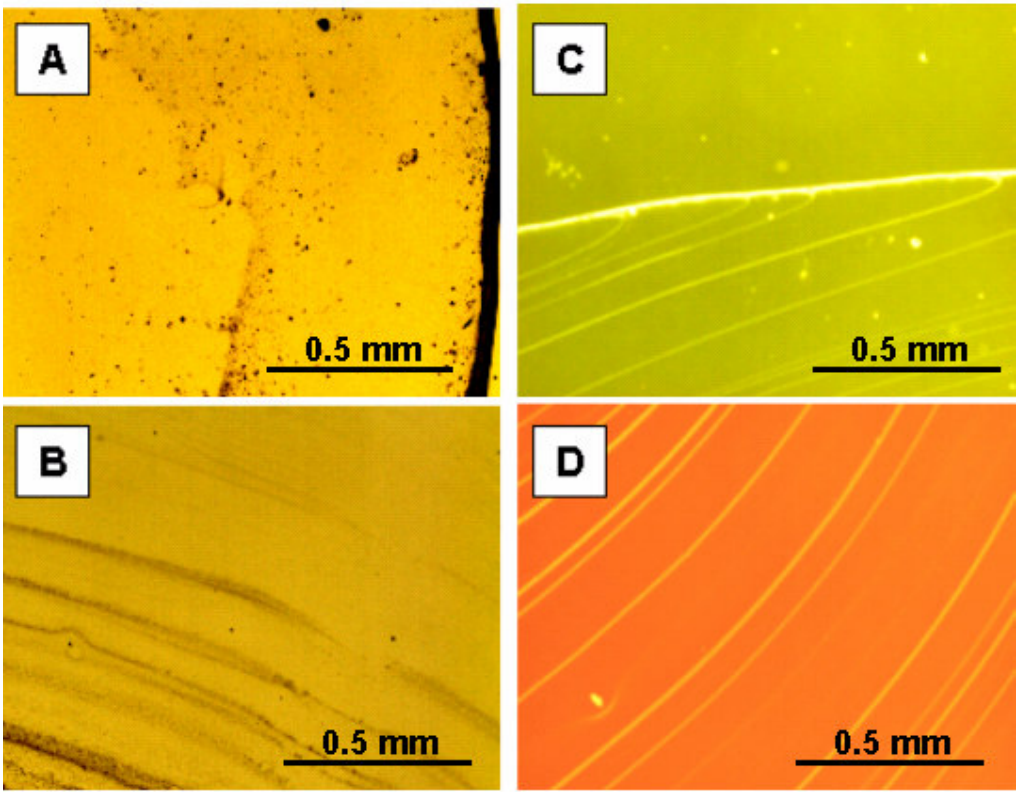

Figure 6: *Optical microscope images of a part of the dried rings pattern; A) an outer part of a ring by cold drop, B) an inner part of a dried cold drop "lacy pattern", C) an outer part of a dried hot drop "discontinuous rings", D) inner part of a dried hot drop " multiple rings". Scale bars are* ***0,5 mm*** *in all images.*

It turns out that the self pinning mechanism is not so straight forward and ring formation is not so simple as one might get the impression from a statement of Deegan "The deposition can be predicted and controlled without knowing the chemical nature of the liquid, solute or substrate" (6).

The puzzle of the end structures could be better understood by taking into account the evaporation modes of a pure liquid, which is neglected by most of the authors.

In 1977, Picknett and Bexon (155) reported on the mass and profile evolution of a slowly evaporating liquid drop. They distinguished two basic modes for evaporation, i.e., the Constant contact Angle mode (CA), where the base shrinks with time while the contact angle remains constant, and the Constant contact Base mode (CB), where the base diameter remains pinned while the contact angle decreases with time. Evaporation occurs either with these two distinct modes or with some

combination of them. The transition from one mode to another is not delicate but depends on the nature of the solvent, drop diameter, and the evaporation flux. In 1989 Birdi et al. (156) reported the mass and contact diameter of water and n-octane drops placed on glass and Teflon. Two regimes were observed during drop evaporation on substrates. In the first case, with contact angle < 90°, the evaporation rates were found to be linear where the contact radius is constant and the contact angle varies. In the second case, with contact angle > 90°, the evaporation rate was nonlinear, the contact radius decreased, and the contact angle remains constant. In 1994 and 1995 Shanahan and Bourges-Monnier (157,158) studied the evaporation of large water and n-decane drops (3-5 mm^3) on polyethylene, epoxy resin, and Teflon. They showed the existence of four distinct stages in the evaporation process. In the first stage, the contact radius remains constant while the contact angle and the drop height decrease. In the second stage, the same processes happen but the evaporation rate increases. In the third stage, which follows for smooth surfaces, height and radius diminish collaterally, and the contact angle is maintained more or less at a constant value. In the final stage, the drop disappears in an irregular fashion with all parameters tending to go to zero. This step is difficult to follow experimentally, and it is probably related to the triple line anchoring on local heterogeneous zones. In 2005, Fang et al. (159) studied the evaporation of water, methanol, acetone and toluene drops. In the first stage of evaporation, a water drop is pinned by surface heterogeneity of the substrate and shows a constant (CA) and (CB), then it evaporates under (CB) mode with discontinuous variation of the contact angle i.e. decrease, before a mixed mode is observed at the end stage. An alcoholic drop is also first pinned and then showing a (CA) mode (Base varies) with a “Stick- Slip” like fashion. Acetone shows a short pinning before a mixed mode sets in with a very rapid decrease in the base diameter accompanied by increase of the contact angle.

These experimental observations tell us that if a macroscopic drop of those liquids is allowed to evaporate, then the end structures after a complete drying will be: a) only a ring in case of water, b) several rings in case of alcohol and c) a thin outer ring with a thick film in the interior by acetone. However this observation must be valid for a diluted solution.

To visualize this effect, drops (50 µl) of diluted salt (10^{-5}M, $AgNO_3$) are allowed to evaporate from different solvents at room temperature. Figure 7 shows the resulting structures after complete drying of; a) salt/water, b) salt/isopropanol, and c) salt/acetone, on a silicon substrate, respectively.

Three different structures are observed; in the case of water a thick ring is formed whereas isopropanol showed several rings and by acetone a thin ring with a film in the interior is formed. Indeed, the obtained patterns are in agreement with the ones expected above. It seems to be that the evaporation mode of the pure liquid controls and regulates the final structures. This is plausible under the condition of a diluted solution because the physical properties of the solution are almost the same as the ones of the pure solvent.

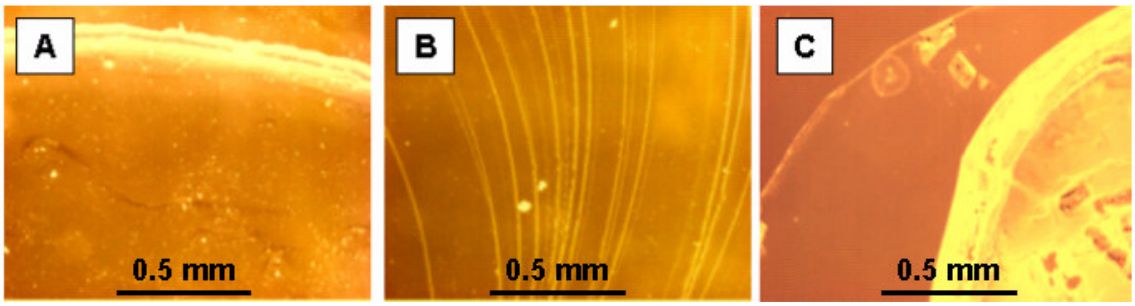

*Figure 7: Optical images (DF,colored) show the patterns obtained by drying a drop of silver nitrate, ($C=10^{-5}M$, RT) in different solvents; A) water, B) isopropanol, C) acetone. Scale bars are **0,5 mm** in all images.*

Furthermore, the lacy patterns obtained by the cold drops shown above (Figure 6b) can now be easily understood as a result of the mixed mode appearing at the late stage of evaporation for water.

An interesting observation is the formation of multi-rings in the case of isopropanol in analogy to the hot drop. Therefore the question arises, whether the cold water drop changes its evaporation mode upon heating.

Molecules that evaporate from a liquid must be located near the surface and must have sufficient kinetic energy to overcome the liquid-phase intermolecular forces. The evaporation proceeds more quickly at higher temperatures due to the lowering of the intermolecular force.

In 1995, Rowan et al. (160) revealed a very basic equation relating the change rate of the drop volume, dV/dt, to its height, h:

$$dV/dt = -kh. \tag{3.5}$$

This equation has been widely adopted for various purposes since its publication (161). The drop evaporation constant, k, in the equation is defined as $(2\pi DM/\rho RT)(P_s - P_0)$, where D is the diffusion coefficient of the vapor molecules in air, ρ is the density of the drop liquid, M is the molecular weight of the liquid, R is the universal gas constant, T is the temperature, and P_s and P_0 are the vapor pressures of the liquid on the drop surface and at infinite distance away from the drop, respectively. The pressure term of the Rowan equation is linked to the intermolecular cohesive energy in the liquid (heat of vaporization), ΔH_{vap} by the Clausius-Clapeyron equation:

$$\ln P_s/P_0 = -\Delta H_{vap} / RT + \text{constant} \tag{3.6}$$

This equation tell us that the weaker the intermolecular forces in the liquid, the easier it is for molecules to escape from it, and the higher the vapor pressure will be.

At room temperature the latent heat of water is higher than of isopropanol (ΔH_{Water}= 44 kJ/mol and $\Delta H_{Isopropanol}$= 38.6 kJ/mol) (162,163), which means, that the vapor pressure of water is lower and the rate of evaporation is lower. As a result the water shows a (CB) mode with variation of contact angle and formation of a ring.

The decrease of the intermolecular cohesion force by an increase of the temperature is known. For instance water at 80° C has ΔH_{Water}= 41kJ/mol. Indeed, the latent heat of water becomes nearly equal to that of isopropanol, and one would expect approximately the same pattern consisting of several rings like the one shown by isopropanol. However, the main difference between the water hot drop and the isopropanol cold drop is the evaporation mode. Where isopropanol shows a (CB) mode, a hot drop shows a mixed mode at the contact line. This mixed mode will result in a hopping of the contact line, i.e. contact angle decreases, which reduces the segregations of the solute between the lines.

The following conclusion can be drawn so far: Drops of different solvents dry differently hence different drying patterns are obtained. This is mainly irrespective of the dissolved material under diluted condition. The physical properties of the liquids control and regulate the form and shape of the structures that will be finally obtained. In this context the drop size and total evaporation time, concentration etc. will play a crucial role to tune the obtained pattern. There is no theory in literature that explains the control in patterning by the choice of the solvent. But a qualitative understanding of this complicated process (164) is a crucial part if a drop will be used as a new tool for patterning.

However, drying of a free hot drop results in macroscopic stochastic rings, which would be most likely ineffective in advancing any technologically useful application. Therefore, it is focused on two main aims: 1) Organized nanostructures

2) Not only ring but also wire geometries, which is a big challenge for nonlithography drop approach.

3.4.2 Strategy for Ordering Structures and Wire Formation Using a Hot Drop

3.4.2.1 Parallel Arrays

It is well known that pinning of the contact line on a substrate is produced by boundaries separating regions of different surface chemistry or physical roughness. Such a region is considered as a microscopic domain of a system. The collective behavior of all the microscopic domains results in a joint macroscopic pinning of a moving contact line (165). So that a single small defect can not keep the contact line pinned. Even if the interface becomes pinned for a moment, the elasticity of the interface attempts to smooth over the deformations caused by the pinning site. For wetting, the liquid-vapor interfacial tension provides elastic forces. At long length scales, gravity also smoothes the interface. If the defect is strong enough, it will "pin" the line locally and force it to stretch. In the vicinity of the defect, i.e., at length scale ≤ capillary length, the contact line keeps the symmetry of the defect and adopts to takes its shape. The capillary length describes the perturbation of the contact line near the defect. This perturbation will decay exponentially in a distance equal to the capillary length (166).

The relevant parameter to describe the influence of a defect is the dimensionless field strength, f (167), which is defined quantitatively as: $f = d\Delta S/\gamma e$ where d is the defect diameter, S is the spreading parameter coefficient, e is the drop/ film thickness, and γ is the surface tension of the liquid.

Indeed various models have attempted to explain and predict the influence of such surface heterogeneity and defects on contact line structure. Theoretical models have focused on dilute (168), randomly positioned (169) and patterned defects (170). Even though this complex behaviour is not fully understood, it is believed that new experimental and theoretical models are needed for a quantitative understanding of these phenomena (171).

However, by the combination of this deformation effect with the mixed mode of evaporation observed by the hot drop, a new route for nanostructure fabrication has been developed. The general setup can be understood in terms of a Deformation accompanied Dewetting of the contact line around a strong Defect (DDD or D^3 Approach).

Utilizing this approach was first done by drying a hot drop (10^{-5} M of $AgNO_3$ salt solution) on a structured Si substrate containing engraved number "1". A pattern consisting of dried lines was formed. Those lines took the shape of the number "1" that acted as a defect on the free surface, see Figure 8a. Furthermore, an intentionally introduced artificial circular defect forces the hot drop to dry around it in a regular manner. Several rings are observed as shown in the SEM image in Figure 8b. A high magnification image Figure 8c shows that the line width can go down to nanometer range.

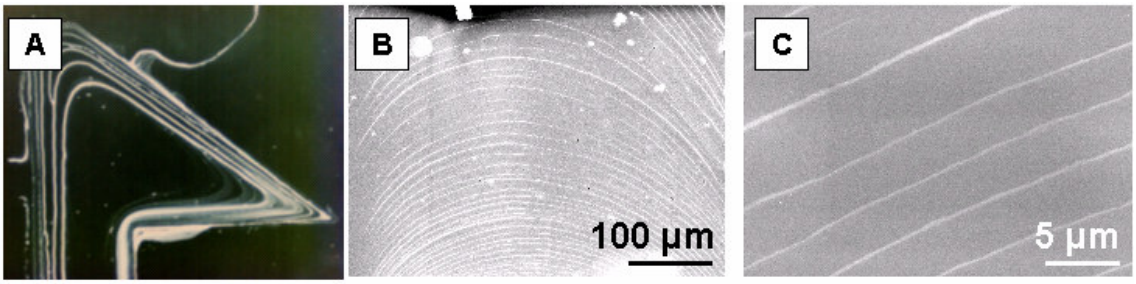

Figure 8: Patterns formed by drying of a hot drop around a defect; A) An optical image (DF) of deformation of lines around No.1, B) A SEM image show the rings formed by drying around a circular defect, C) high magnification of the inner region of image in B, show that the lines width is in nanometer range.

As mentioned before, to achieve structuring such as wire arrays using a droplet is still considered to be problematic. Yawahare et al. (172) demonstrates the formation of meso lines from a drop using nanoparticles under three perquisites, evaporation between partially wetting surfaces, the presence of pining points and the availability of a surfactant. As a further development and simplification the D^3-Approch is used here to obtain an mm^2 area of wires in a controllable manner.

The general steps of the D^3 strategy are described in the followed sketch and can be summarized as follow:

1) Cylinder or tube (defect) is placed on a clean substrate.

2) The complete set up is introduced to a hotplate at 80 °C.

3) Deposition of a drop containing the desired material.

4) Tube (defect) lift-off after complete drying.

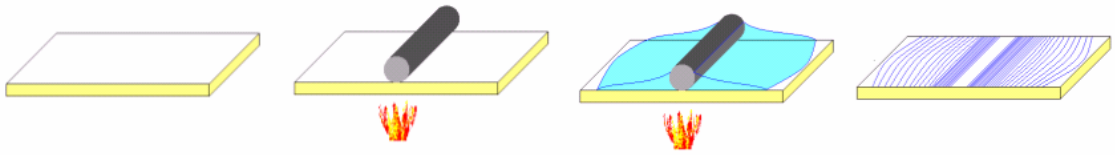

Figure 9: Sketch describing the general steps for "DDD" /"D^3"approach.

Experimentally, a glass cylinder with a diameter of about 1.5 mm and a length of about 8 mm is positioned on a flat silicon substrate to a hot plate at 80 °C. A 40 µl drop of 10^{-5} M silver nitrate is deposited on each side of the cylinder. The drop spreads on the substrate, some of the solution remains unbound, while the other part is trapped within the gap between the cylinder and the silicon substrate due to capillary force. The dried pattern obtained from this geometry is sketched in Figure 10b and the corresponding SEM image shown in Figure 10c.

Alignments of lines in insulated parallel patterns require an elimination of the curved part around the tube. That can easily be done if the tube length is equal to the substrate length or the end part of the tube is located outside the substrate. A glass cylinder with a diameter of about 1.5 mm, and a length of about 15 mm placed on a flat silicon substrate of ~15x15 mm^2 and the same procedure like above was repeated. Here the end pattern is sketched in Figure 10 d,e. The lines here align themselves parallel to the axis of the cylinder as seen in the SEM image in Figure 10f.

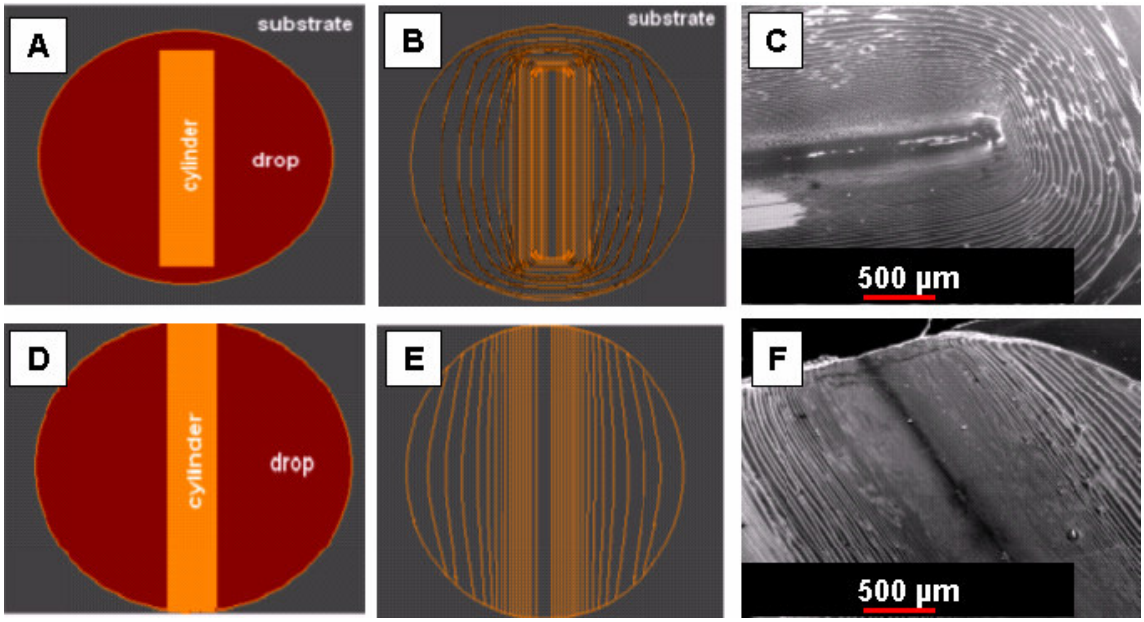

Figure 10: Top view of drying lines and SEM of the patterns obtained. A) Schematic representation of one of the configurations used in this study "tube pattern", B) the expected dried pattern from this configuration, C) A SEM image for the obtained pattern. D-F) the same like A-C) but for lines pattern. Scale bars are ***500 µm*** *in both SEM images.*

Away from the cylinder, the structure shows the well known ring geometry already observed by the free hot drop experiment. This indicates that here the tube has a minor effect on the contact line. As the contact line reaches a certain critical distance, d, it takes the shape of the tube. This critical distance was observed to be in the range of 1 mm, i.e., less than the capillary length of the solvent (~2.5 mm) and slightly above the tube diameter (0.75 mm).

Up to this critical distance the defect strength is high enough to cause a deformation of the drop. The deformation around the defect can be seen as a result of a competition between the force connected with the tensions of the drop edge and the force connected with the tension exerted by the field strength on the contact line.

The lines shown in Figure 10f were heated above 200° C for 2 hr to convert the salt ($AgNO_3$) to silver according to:

$$2AgNO_3 + 200° C \rightarrow 2Ag \downarrow + \uparrow 2NO_2 + \uparrow O_2$$

Investigation by optical microscope, Figure 11a, revealed the lines stability against the chemical transformation and shows the highly ordered lines on both sides of the glass cylinder. The wires length is observed to be comparable to the tube length. The distance between the wires as well as their width decreases in the proximity of the contact line between the cylinder and the substrate, see Figure 11b, 500 µm away from the tube, and c) in the vicinity of the tube ~ 100 µm.

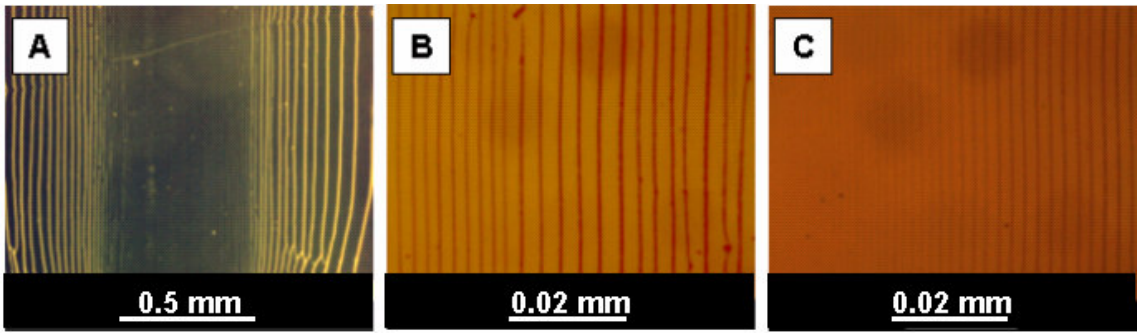

Figure 11: Investigation of the lines after the chemical transformation, , A) An optical image (DF) shows the stability of the lines around the both side of the tube. B) An optical (BF) images revealed that the wires width and the distance between them decreases in the proximity of the tube. C) like B but closer to the center and therefore with even smaller lines.

Further examinations were done with the aid of SEM. Four positions were chosen to be examined, a, b, c and d which are shown as arrows and its corresponding SEM image in Figure 12a-d respectively. Area a) shows microwires which are formed 0.5 mm away from the middle of the tube, in proximity to the tube in area b) shows mesowires which are located at a lateral distance of ~300 µm from the line of contact between the glass cylinder and the substrate, and in the vicinity of the tube in the area c), which extends 200-100 µm from the contact between the glass cylinder and the substrate, highly regular and homogeneous wires down to ~200-100 nm are obtained. An EDX line scan was carried out across the wires at position (a). Broad wires were chosen to be able to show enough signal for a determination of the chemical composition. Pure silver peaks are obtained at the positions of the wires, while the oxygen peaks are at the noise level as shown in Figure 12e, which confirms the transformation of silver nitrate to sliver.

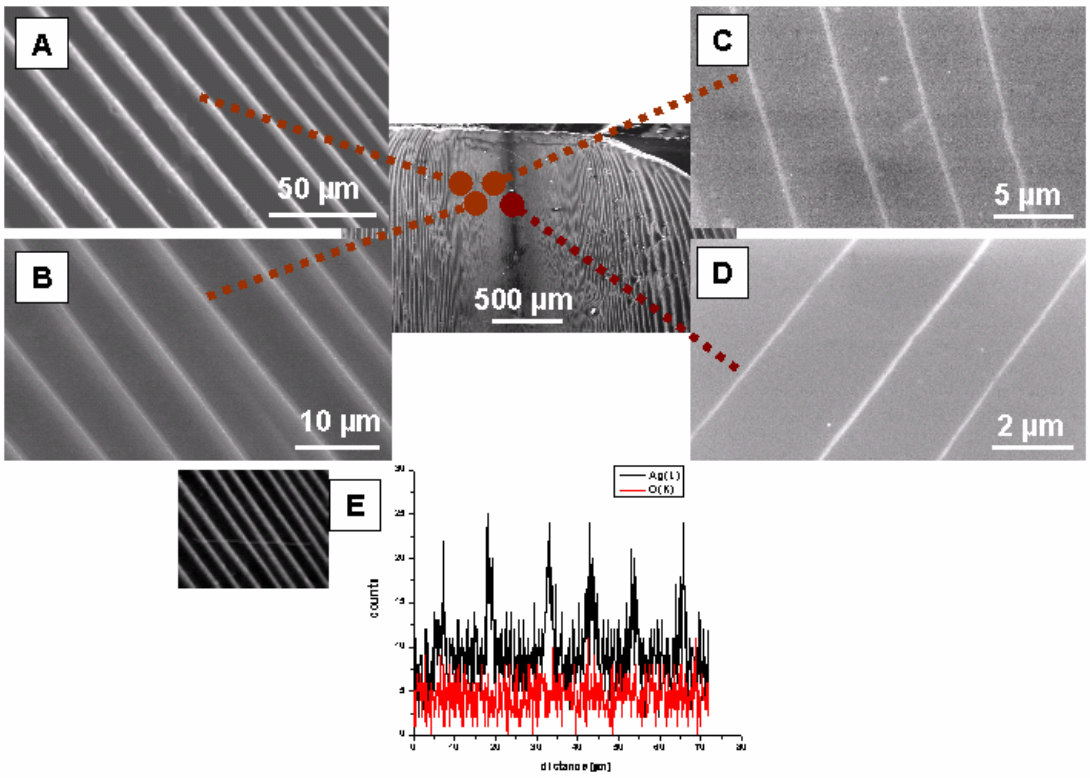

Figure 12: SEM images of the parts of silver wire arrays obtained from thermal decomposition of the wet deposited silver nitrate: images A-D) comparison between four different positions and illustration of the gradient nature of the wires, E) EDX line scan reveals a successful transformation of silver nitrate to silver.

AFM investigations showed that not only the width and the distances are changed but also the wire height becomes smaller even in the same area as shown in Figure 13 a,b for a mesowire area. The smallest wire in this image, the one on the right side of the image, is ~600 nm thick and ~15 nm high, see Figure 13b. However, closer to the tube, in the area that extends 200 µm from the contact area between the glass cylinder and the substrate, nanowires of sizes down to ~200 nm with a height of ~ 20 nm were obtained as shown in Figure 13c,d. Wires below < 100 nm, with a height of ~ 2 nm are obtained in the area that extends 100 µm from the tube, Figure 13e.

However, in the vicinity of the tube, a line of dots is formed, Figure 13f. This can be attributed to the surface tension driven Plateau-Rayleigh instability. The instability could be seen as a result of 1) reduction in the line width or 2) simply a concentration effect where the concentration of the solution at the end of the stage of the drying process becomes extremely dilute compared to the initial concentration or 3) a combination of both effects.

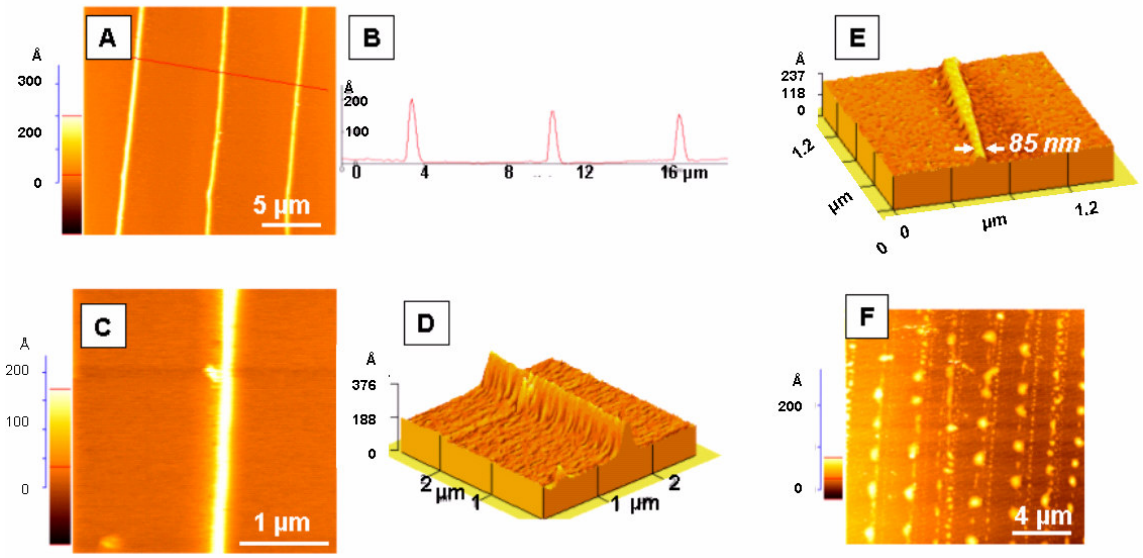

Figure 13: AFM images of the aligned wires: A) A part of mesowires and B) A line scan on the same wires reveals the height change of the wires, C) Nanowires of 200 nm and D) 3D topographical AFM image of the same wires show a height of ~ 20nm respectively. E) 3D topographical AFM image of wire below 100 nm with a height of only 2 nm. F) Image showing the instability that occurs in the near vicinity of the tube where doted line is formed.

The obtained results confirm the gradient nature of the wires. This gradient effect has been found in the case of a restricted geometry (173) which consists of a spherical lens on a flat substrate, and the resulting pattern is a gradient of macroscopic concentric rings. This is explained in the light of stick-slip motion of the contact line: A repetitive motion (174) of the line is a result of the competition between a "pinning" friction force and a "depinning" capillary force due to the irreversible solvent evaporation. High evaporation rates at the stationary contact line cause a fluid flow from the interior towards the edge. The resulting outward flow carries the non-volatile particles. The deposition of these particles at the edge exerts a friction force against the movement of the contact line causing it to "stick". Decrease of the contact angle during the evaporation causes an increase of the capillary force. When the contact angle becomes similar to the receding angle, the capillary force becomes greater than the friction force hence the contact line becomes unstable and "slip" (175,176) to a new position.

In contrast to the process described above where pre-existed particles are used, here an aqueous solution of $AgNO_3$ is used; the deposition processes have to be interpreted differently: as the highest evaporation rate is found at the edges rather than in the middle, therefore ionic products will change locally at the drop periphery. Evaporation of the solvent increases the salt concentration until supersaturation conditions are reached and deposition occurs.

Very smooth wires, with a precipitate free area between them can be obtained, as can be seen in Figure 14a (3D representation). This indicates that the supersaturation condition is satisfied at the contact line only. Furthermore, the higher the concentration, the lower the required evaporative loss to reach a

precipitation condition at the contact line. For instance, in the case of higher concentration, here 10^{-3} M, the wires have a frayed side as shown in Figure 14b. This means that the precipitation occurs not exclusively at the contact line but also in its vicinity. Furthermore, Instabilities to frayed side -like structures has been qualitatively understood on the basis of the velocity of the displacement of the meniscus. A faster movement stabilized the front, while a slower one led to the development of fingering instabilities at a propagating front (177).The increase in viscosity due to the increase in concentration caused a reduction in the speed of solution front (178), thereby leading to the development of fingering instabilities at a propagating front.

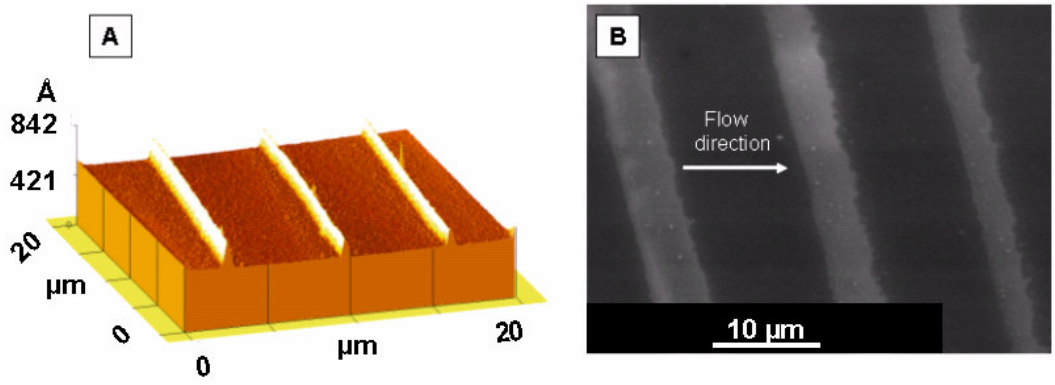

Figure 14: A) A 3D topographical AFM image reveals how smooth the wires are, and showing clearly the cleanliness of the area between them. B) SEM of broad wires with frayed side formed by higher concentration, 10^{-3} M.

3.4.2.2 Grid Structure

Till now this "hot drop" method has been limited to simple structures like concentric rings or parallel wires. Even more complex patterns can be formed if two subsequent depositions are applied. For example, the formation of a grid structure can be easily realized as sketched in Figure 15a below. Here lines are formed by a first deposition around the tube. Turning the tube by 90° around the first dried pattern and applying a second deposition results in a crossbar network of wires, a "grid". Figure 15b shows a SEM image of a realized grid with a gradient mesh sizes. AFM images of this grid were also taken by keeping an angle of about 30° between the scan direction and one set of the wires in order to eliminate artifacts. A 3D topographical AFM image as well as a close up are taken as shown in Figure 15c,d, respectively. The 3D image shows clearly that the region between the crossing wires is deposit free. There is no trace of any structural change between both deposited wire arrays which indicates that the wires deposited first have no influence on the second deposition, i.e. no pinning effect. The deposit has a deciding role in the stick-slip motion mechanism by the pinning of the contact line.

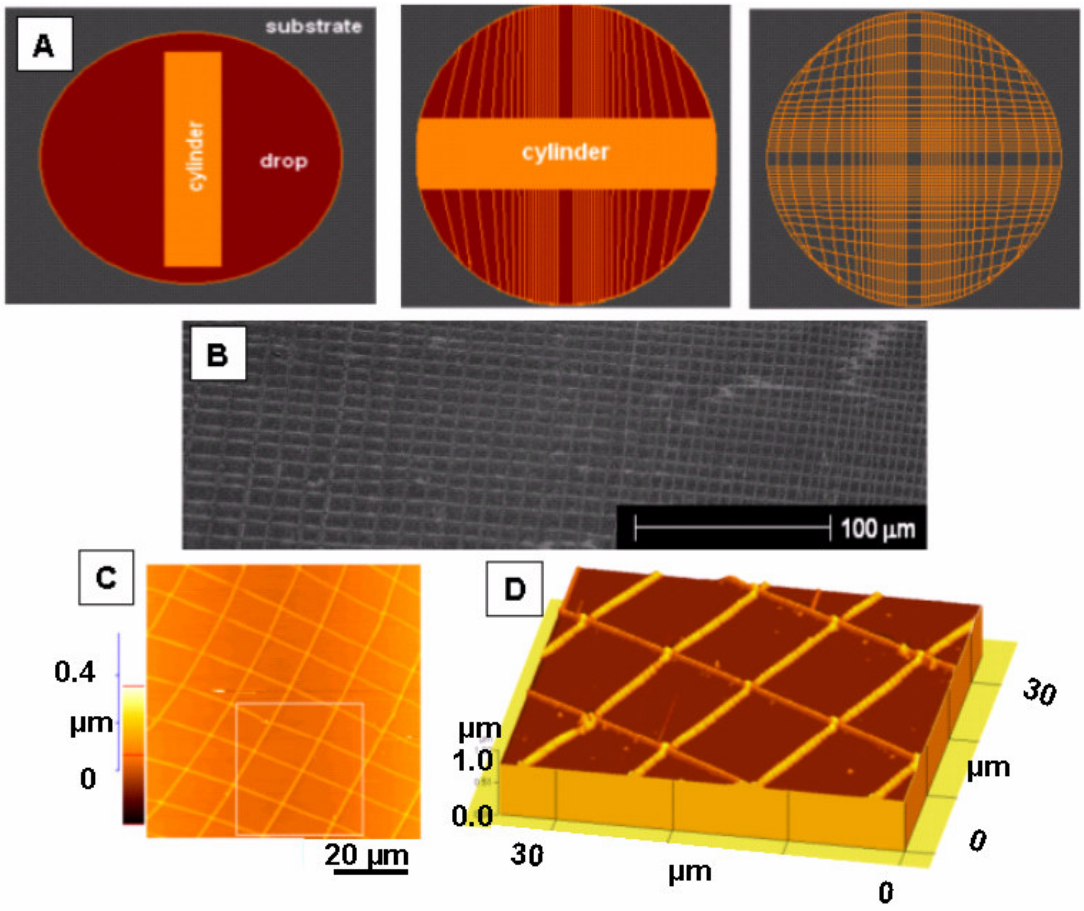

Figure 15: Grid pattern: A) A sketch illustrate the mechanism of Grid formation, B) SEM image of the grid formed and C,D) An AFM and 3D topographical AFM image of the part of the meshes formed.

It is surprising that the presence of the first array of lines does not interrupt the pattern formed by the second drop. To verify this observation, in a modified experiment a free hot drop is allowed to evaporate on a structured sample. The optical image in Figure 16 shows that the drop behaves as if it dried on a smooth, unpatterned surface. This confirms that there is no influence of the first structured surface, and that the mechanism of stick-slip discussed in the literature can not applied here in this manner. Indeed, to date, neither the mechanisms responsible for the stick–slip of the three-phase line nor the thermodynamic interpretation of the corresponding contact angles are well understood (179). Moreover, this mechanism explaining the situation for free droplet is essentially stochastic even on flat silicon and can not explain the high regularity of the wires near the tubes. It seems, that there is at least one other mechanism affecting the patterning phenomenon.

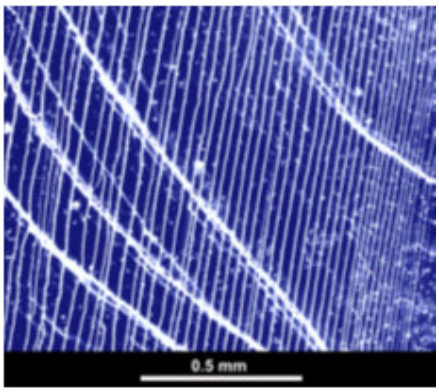

Figure 16: Optical image (DF), drying pattern of a free drop on the already existing lines. No pinning effect is observed.

Dewetting instabilities of thin films are well known and can play a crucial role in the patterning observed here. This can be discussed qualitatively as follows:

Rupturing of a thin film at a characteristic "critical thickness" was theoretically predicted in 1966 by Vrji (180). The original Vrij model emphasized the breakup of soap films. A variant of this model for investigating the dewetting of thin polymer films from solid substrates was developed (181). It was found, that the surface undulations give rise to a pressure gradient which drives the film instability. Two mechanisms are discussed which may initiate rupture: (i) nucleation, e.g., from defects or impurities in the film, and (ii) spontaneous film rupture. In this kind of dynamical instabilities, there usually exists a critical wavelength, the corresponding amplitude which grows the fastest (182), and thus determines the dominant wavelength. In such a case, one thus expects a dewetting structure with a characteristic length scale behaving correspondingly (183) where the critical wavelength is film thickness dependent (184,185). Based on this approach stripe- and dot-shaped polymeric patterns in micro- or sub micrometer scale are obtained by dewetting of a thin film of a polymer solution on a flat substrate (186). Similarly, stripes of nanoparticles are generated by dewetting of a polymer thin film containing nanoparticles (187,188). It was found that the mechanism for the arrays is the so-called fingering instability (189,190) which occurs at the edge of an evaporating solution comprised of a volatile solvent and the polymeric solute.

Indeed as dewetting of water on a wettable substrate is not a well known phenomenon, the use of organic solvents is more favourable. Those solvents usually have a low boiling point and evaporate easily thereby leaving the dissolved substance behind. Furthermore, the used solvents are mostly lipophilic which enhance its dewetting properties from a wettable substrate.

However it was shown that an evaporating thin film of water on a wettable surface can show a dewetting behaviour by formation of holes (191). The origin of rupturing is simply the excess pressure

in a thin film as compared to the pressure in the corresponding bulk phase (192). This excess pressure is known as disjoining pressure, Π, (193,194) and it is related to the film thickness e by (195) :

$$\Pi(e) = \frac{A}{6\pi e^3} \tag{3.7}$$

where, (e) is the film thickness and A is Hamaker constant.

As the film evaporates, it becomes thinner so that the disjoining pressure acting on it increases until a critical value is reached where dewetting occurs. A schematic of thin fluid dewetting is sketched in Figure 17. The free surface of a thin film deforms by thermal fluctuations in the film thickness, Figure17a. Such a deformation is subject to a driving force "dissipation of energy and thus the increase in system entropy by the evaporated solvent molecules" causing surface waves which grow exponentially with time. However, there is a critical wave which grows fastest and is responsible for the instability, as shown in Figure 17b. In the valleys of this fluctuation, the liquid surface becomes thinner due to the evaporation and the flow from thinner "concave" to thicker "convex" regions "different in the chemical potential" hence the pressure increases with a decrease in the local film thickness, the fluctuation finally reaches the substrate, as shown in Figure 17c, and initiates dewetting, Figure 17e, (196,197).

This dewetting instability can be directly applied to the contact line of an evaporating drop on a substrate. At the beginning the drop has a spherical cap shape, which means a film thinning is considered only at the meniscus. It was found that such a film initiates dewetting through the nucleation mode (198).

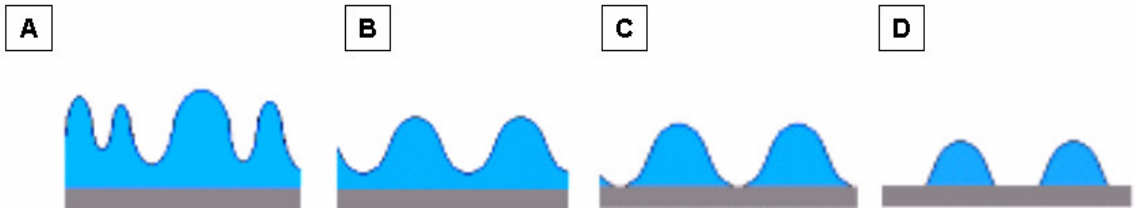

Figure 17: Sketch shows a possible mechanism of the dewetting instability in a thin film.

The phase separation takes place with the formation of holes, forming "dry patches" which will open at the meniscus. These dry patches grow and the material is deposited in the rim surrounding the growing hole hence a discontinuous ring is formed. By further evaporation, the shape of the drop changes from a spherical one to a thin film (see sketch Figure 18 a, b). The interface becomes unstable and the dewetting mode changes from nucleation at the meniscus to thermally exited capillary waves. As the characteristic wavelength is dependent on the film thickness which will vary due to evaporation from one point to another, the critical wavelength corresponding to the instability will also vary,

resulting in stochastically arranged rings. This part can explain the pattern formed by the hot drop (see Figure 5c,d).

Regular structures can be realized by employing a lateral confinement in competition with the thickness-dependency of the characteristic wavelength of the instability. It was shown that in case of a fiber covered by a liquid thin film, a spontaneous destabilization in a highly regular manner occurs (199).

Figure 18: Sketch illustrating a dewetting of a free and a restricted hot drop: A,B) thickness dependant on the instability responsible for the irregular structures, and C) A lateral confinement in competition with the thickness-dependency of the characteristic wavelength of the instability responsible regular dewetting event in the thin film.

This regularity was explained as follows: The system will set itself to a wavelength which is related to the fiber diameter, which is the critical wavelength for the instability. The relation between this critical wavelength and the fiber diameter (b) is:

$$\lambda = 2\pi\sqrt{2}b \tag{3.8}$$

In the same fashion the system here will select a certain wavelength in the vicinity of the tube. However that will be related to the cord of the circular base of the tubes wetted area. So that eqn 3.8 can be modified as follows:

$$\lambda = 2\pi\sqrt{2}r_{cord} \tag{3.9}$$

The cord decreases with the evaporation hence the wavelength will also decrease but in a regular manner as shown in Figure 18c. As a result a gradient of highly ordered lines is formed.

In this context, the motion of the contact line actually might be seen as a result of film thinning by the disappearance of solvent due to evaporation and not necessarily to the lateral (receding) physical movement of fluid in the neighborhood of the contact line.

The wire formation around the tube is preconditioned by fluctuations that reach down to the substrate. If a cold drop dries around the tube but the fluctuation will not finally reach the substrate, only a thin film of a hill and valley structure is formed as seen in Figure 19a,b.

This first qualitative explanation is made as there is currently no quantitative theory to explain these phenomena. Nonetheless controllable dewetting of a diluted aqueous solution to form ordered pattern represent a novel concept (2) that has a high technological potential.

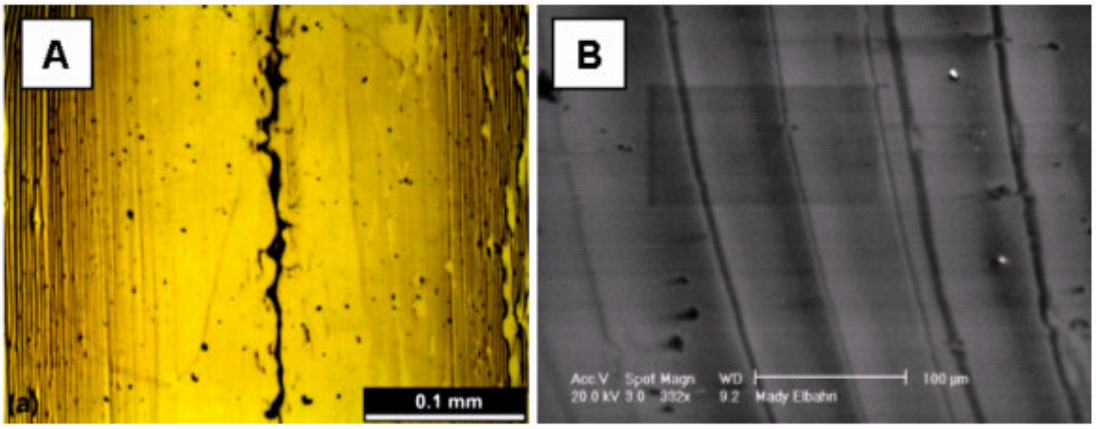

Figure 19: Images illustrating the importance of temperature to obtain separated structures: A) Optical image illustrating the dried pattern of a cold drop around a tube, B) SEM image of the same sample shows the hill-valley structure.

However, away from the two step approach by the hot drop, the realization of an all in one approach using a drop, directly on a substrate where chemical syntheses and structuring occur simultaneously is a novel concept.

As explained in the introduction of this chapter, if a liquid drop touches a hot solid with a temperature higher than the liquid boiling point, the lower part of the droplet will immediately evaporate and partially protect the rest of the droplet from further evaporation. The drop is not any more in contact with the solid but it levitates above its own vapour. Such a drop is called Leidenfrost drop, after the name of the German physician who first reported the phenomena 250 years ago (200). In the next section it will be shown that the superhot drop at Leidenfrost temperature permits a novel aspect for nanotechnology.

[2] M. Elbahri, K. Hirmas, F. Faupel, R.Adelung.(Patent –applied)

3.4.3 Evaporation of a Superhot Drop

3.4.3.1 Leidenfrost "Nanomanufacturer"

The Leidenfrost condition is defined as a local maximum in the evaporation life time of a droplet (201,202,203). Such a local maximum occurs due to the poor heat transfer between the substrate and the droplet because of the vapor encapsulation. Existence of the Leidenfrost temperature has been widely investigated (204,205). The increase in the drop life time starts at a temperature above the nucleate boiling point of the liquid and increases gradually towards a maximum where a complete vapor film is formed.

The Leidenfrost temperature was found to be varying with the type, nature, roughness of the surface, the way of depositing the drop and the liquid purity (206,207). To determine the Leidenfrost temperature in this work as well as its experimental fluctuation, the life times of water drops (50-75 µl) on three silicon samples were measured. One of these samples was not cleaned, while the others were cleaned in ultrasonic bath using isopropanol for different lenghts of time. This small drop did not cool the hot-plate significantly (evaporative cooling), so the measurements were made under essentially isothermal conditions.

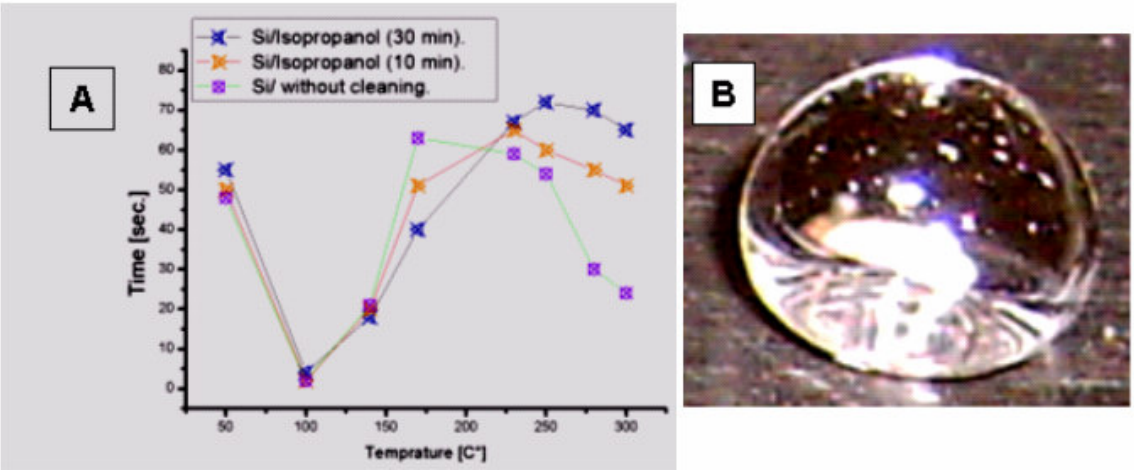

Figure 20: A) Determination of Leidenfrost temperature, B) a typical Leidenfrost drop used.

The lifetimes were determined with a stopwatch, beginning when a drop left the pipette. The result shown in Figure 20a indicates a high sensitivity of the Leidenfrost temperature to the surface roughness. Experimental values of the Leidenfrost temperature depend critically on the conditions of the experiment. The existence of the floating state of the vaporizing drop is related to the establishment of a balance between the force of gravity, accelerating the drop towards the surface, and the force of the excess pressure in the vapor interlayer, keeping the drop in a levitating state. If the drop is located on a rough surface, then the levitation state is only possible when the vapor layer is thicker than the surface roughness to prevent the start of a heat-exchange crisis (boiling). If the surface

is perfectly smooth, then the deciding role in the beginning of this crisis will depend on several parameters like the equilibrium temperature on the evaporation surface and the pressure in the vapor interlayer (208,209). Different details of the Leidenfrost phenomena are still unclear (210,211). For instance, the effect of the drop size on the Leidenfrost temperature is still uncertain. However the dynamics of the Leidenfrost drop is better understood than the static aspects.

The drop size can affect the drop dynamics by changing its shape (212,213). Small droplets below the capillary length ~ 2.5 mm for water have a very rapid motion due to their low friction that allows them to move freely on the surface (214) or even to bounce. A droplet with a radius above the capillary length will form a puddle flattened by gravity which will reduce the free friction transport behaviour known for a spherical droplet. Bigger droplets ~ 50 mm will suffer from instability by formation of bubbles inside the drop which will rise and burst at the upper surface (215). The driving forces for this was argued to be deformation of the lower interface caused by the difference in pressure between the center and the edge of the drop.

However, under experimental condition in which this work was conducted motion has been observed for droplets up to ~ 6 mm diameter. Consequently a superhot drop with a diameter of around 10 mm @ 230 °C is found to be optimal for the Leidenfrost drop and typically used for a deposition. A typical drop used in this experiment is shown in Figure 20b.

In contrast to a ring/multi rings that formed by evaporation of cold/hot drop, evaporation of a superhot drop resulted in a thin film. The Leidenfrost drop has usually no constant shape (216,217). The drop radius as well as the thickness of the vapour film will decrease steadily over time in the gravitational regime before a global evaporation is observed in the capillary regime; so the drop does not only shrink but it also sinks (218). Consequently, if a loaded drop is used a thin film is obtained. Figure 21a shows an SEM image of a part of such a thin film formed by using a drop loaded with 0,003 M of zinc acetate. The high magnification image Figure 21b shows that the film is composed of a dense assembly of nanopillars. EDX measurement, Figure 21c, shows no traces of carbon and ascertained that the film consists of ZnO. This is remarkable, as the thermal decomposition synthesis of ZnO rods at solid substrate using acetate salt as precursor was only observed to occur at 280 °C (219,220) whereas here the reaction takes place at a temperature of ~230 °C. However a thermal decomposition mechanism is questionable in this case as the temperature in the droplet is far too low to explain the reactions (< 100 °C). As a reaction zone, only the vapor/liquid phase between the substrate and droplet can be considered to provide a nucleation and growth zone with adequate temperatures/pressure.

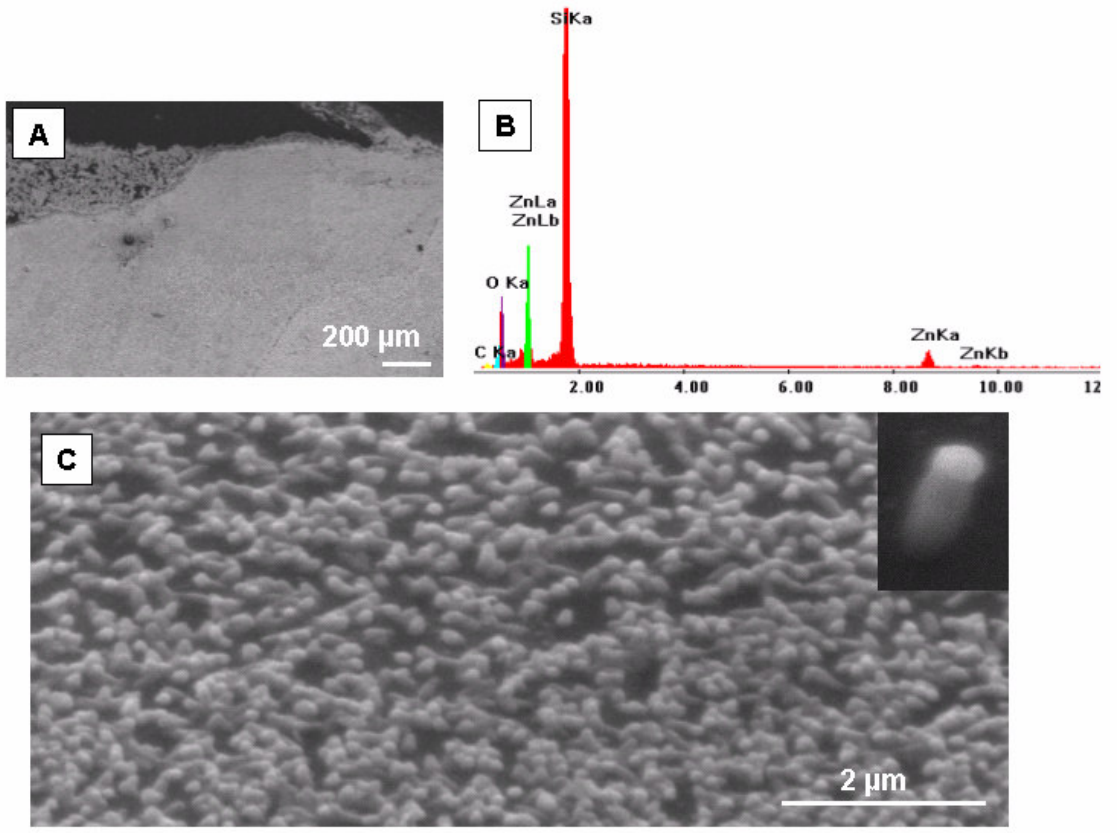

Figure 21: Formation of nanoparticulate thin film of ZnO using a superhot drop, A) A SEM of a part of the thin film, B) EDX measurement shows the film composed out of ZnO, C) High magnification of A, reveals the formation of nanopillars.

3.4.3.2 Metastable Chemical Reactor "MCR" Underneath the Water

As was shown (see introduction) the vapour/liquid interface is established at the Leidenfrost temperature for liquid drops or liquid films in which an encapsulated vapour layer separates the hot wall from the liquid. Therefore the unusual synthesis of ZnO realized in the superhot drop is also expected to occur in the liquid film.

To verify this hypothesis a beaker with 100 ml of 10^{-3} M. zinc-acetate was put on a hot plate at 230 °C. After a short time (5-10 min.), a floating thin film, as seen in Figure 22a, could be observed on the water surface, "cold interface", before boiling started. The floating behaviour results from the convection flow that occurs upon the vapor film collapse underneath the water (see introduction). The film can be easily taken off by fishing it out with a silicon substrate, rinsing with hot water and a subsequent drying in air, see Figure 22b. High magnification SEM images of the extracted film can be seen in Figure 22c, it can be seen that the film is composed of nanopillars, Figure 22d. EDX analysis showed that the pillars are composed of ZnO, Figure 22e. Further investigation by the aid of XRD,

Figure 22f, confirmed the wurtzite crystal structure of ZnO, where the peaks appear at 2Θ = 31.7º, 34.4º, 36.3º, are corresponding to (100), (002), (101), respectively.

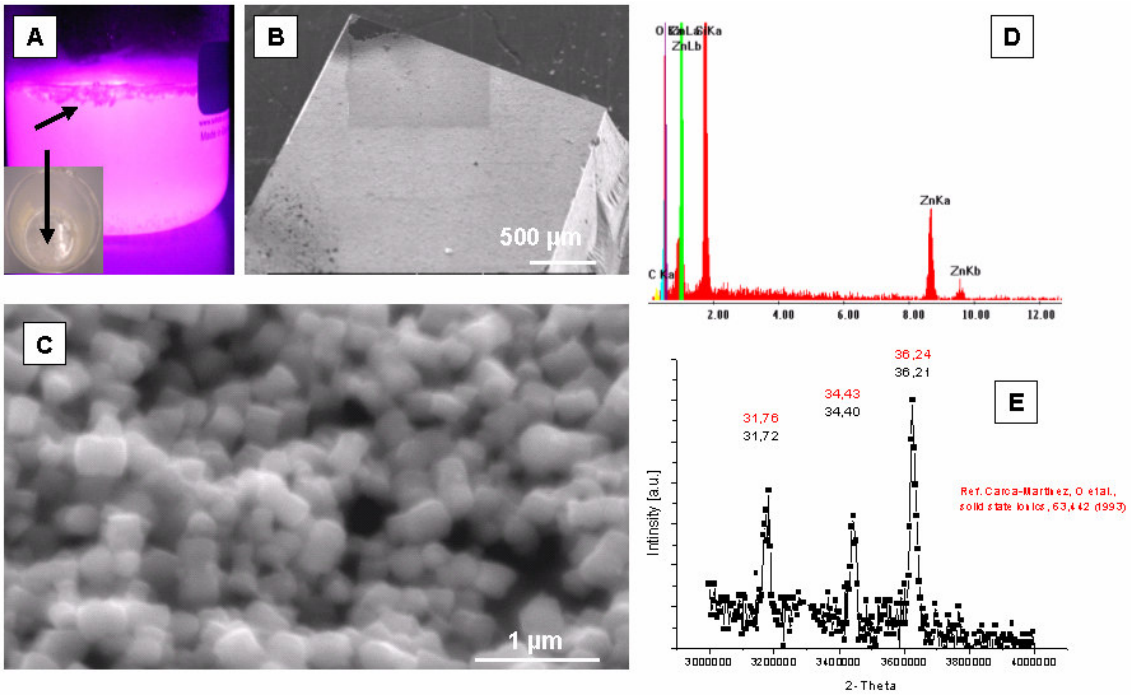

Figure 22: ZnO formed in a glass beaker at Leidenfrost temperature: A) an image showing the floating film, side view of the film under illumination with a UV-Lamp, B) SEM of the film after extraction placed on Si substrate, C) High magnification SEM image revealing that the film is composed of ZnO nanopillars, which is confirmed by EDX as well as XRD, D), E).

Interestingly, when the experiment was done in a conventional way, by introducing the beaker with solution on the plate before heating, instead of the nanoparticulate thin film a turbid solution followed by a white participate with a sponge like structure as confirmed by SEM, Figure 23a, which is composed of zinc acetate as confirmed by EDX, Figure 23b was obtained. The same behavior was also found by using a drop, see Figure 23c,d. That indicates the correlation between the film/drop and illustrates the importance of carrying out the experiment around the Leidenfrost temperature.

A wide variety of routes was already found to syntheses ZnO, because of its unique applications in various fields. The synthesis of 1D ZnO nanostructures has attracted considerable interest because of their promising applications in nanoscale optoelectronic devices (221). Among the manifold techniques described in the literature, evaporation and condensation processes are favored for their simplicity and high-quality products (222,223) but these gas-phase approaches generally require economically prohibitive temperatures of 800–900 °C and remains constrained by the expensive insulating (for example, GaN) substrates required for oriented growth, as well as the size and cost of the vapor deposition systems (224). Wet chemistry approaches provide the best choice because of their low growth temperatures, low cost and good potential to scale-up. Nanopillars/rods growth of divalent

metal oxide like ZnO is theoretically and experimentally verified to have occurred by heterogeneous/ secondary nucleation and mostly under highly alkaline condition (pH~11-13). In this regard, Vayssieres et al. developed a seeded growth process to make ZnO rods and columns (225). However the long time (5-10 hours) as well as use of organic solvents, which is not desirable considering the new trend of green chemistry, limits this approach. A direct formation of nanopillars in alkaline solution without a seeding layer was achieved by solvothermal syntheses using pressurized batch reactors "autoclave" under mild temperature of 150 °C (226). However the long time, of 24 hours, and also the high cost, and the poor quality and quantity of the end product limits this approach.

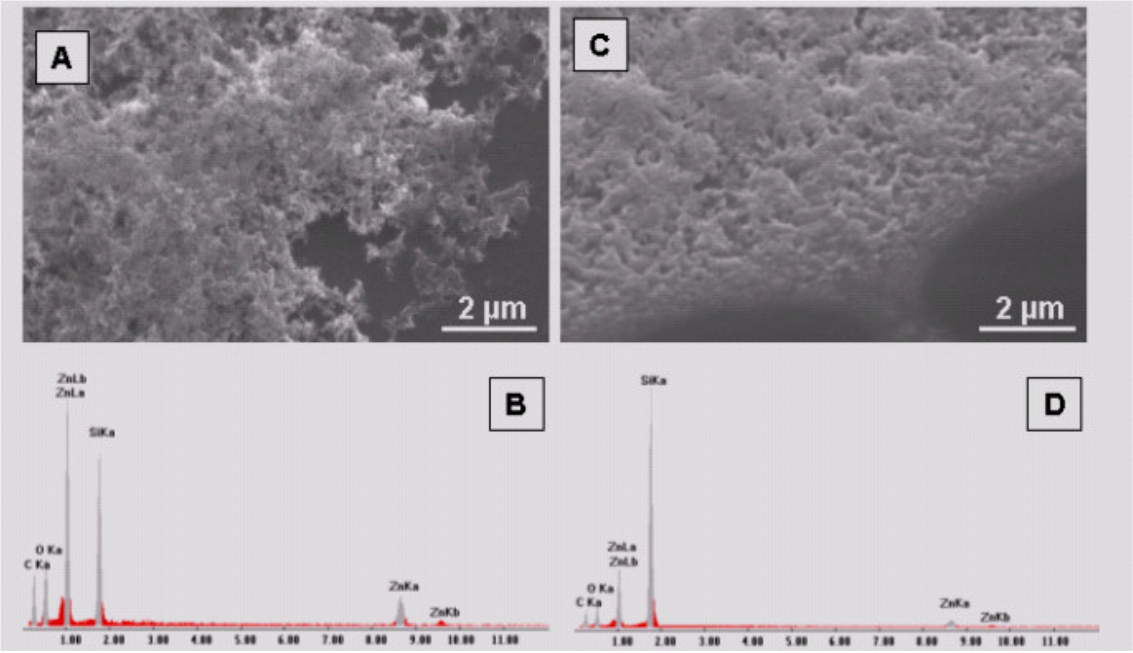

Figure 23: Images illustrated the importance of carrying out the experiment around the Leidenfrost temperature. For example the identical concentration of zinc acetate under the conventional way results in an unorganized precipitation with a sponge like structure, SEM and EDX by a film A,B and drop C,D.

Direct ZnO nanoparticle syntheses in water are not appealing. Conventional synthesis of such particles has been considered to be especially difficult in the absence of any organic solvent and/or basic condition (227,228,229,230). It turns out, that the metastable chemical reactor (MCR) ([3]) under Leidenfrost condition permits an exception for the growth of ZnO in water and more importantly, gives suitable conditions for synthesis of ZnO nanorods, (see Figure 24a,b,) in a one rapid, cost effective and green process.

From a chemical point of view, formation of ZnO from acetate is considered as basic hydrolysis reaction, i.e. pH 9-13. However, here, at pH~6.3 (measured by pH-paper) it becomes difficult to

[3] M. Elbahri, R. Adelung, PCT/DE2007/001444.

explain the result by the conventional way. Indeed, the result obtained here suggests that the water participates as a reactant and/or as a catalyst in the reaction.

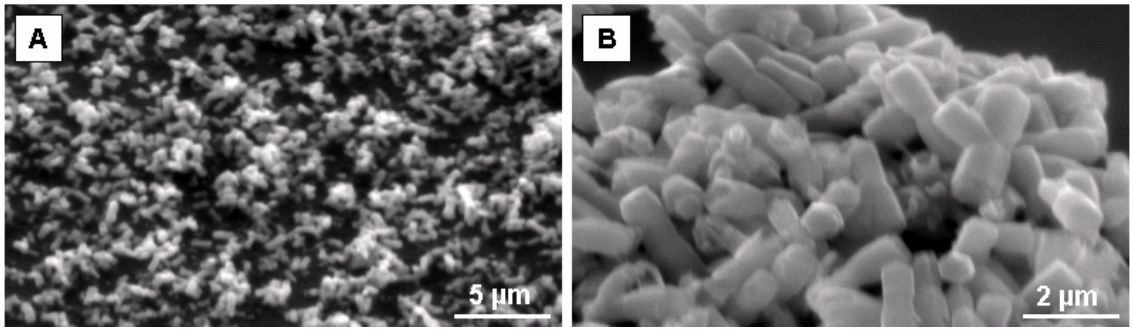

Figure 24: Nanorods formed at Leidenfrost temperature with a higher concentration (5.10^{-3}M): A) thin film of nanorods, B) higher magnification SEM reveals the hexagonal structures of ZnO.

Indeed, a charge separation at the interface of an evaporated aqueous solution on a hot surface and under Leidenfrost conditions was introduced by C. Pounder in a series of publications (231,232,233,234) between 1970 and 1980.

If that is the case here, and by taking into account the diminishing ability of water to solvate the ionic species of an inorganic salt at temperatures above 200 °C (235), it follows, that the hot interface formed under Leidenfrost conditions enriches a high concentration of different ions ($ZnOH^+$,$CH3COO^-$, H^+, OH^-). The inhibiting ability of charge separation results in high ion associations at the metastable hot interface which have nowhere to go, they must recombine quickly. These ions can interact in different ways. However, the above result indicates that the pathway to form ZnO is favored compared to the others. Accordingly a possible mechanism for ZnO could be that; the proton of water is combined with the acetate ions where proton is consumed, and the interface now is rich with OH^-, hence the basic hydrolysis required for ZnO is realized at the hot interface where ZnO can be formed.

Indeed, the temperature and pressure at the hot interface seems to play an important role to promote a rapid transformation, which could take place in an irreversible manner. Actually the overall chemical reaction at Leidenfrost temperature might be:

$$Zn\ (CH3COOH)_2 + H_2O \rightarrow ZnO + 2\ CH3COOH$$

It is worth mentioning here that the stability of "MCR" is governed by the stability of the hot interface. As a vapour film collapse occurs the temperature is automatically shifted to the evaporation regime and boiling starts. This means that any perturbation of this condition will affect the efficiency of the reactor. A remarkable reproducibility of ~ 50% can still be achieved used this way.

In all cases, for the thesis, the important finding is that a superhot drop includes a chemical reactor and now the challenge is to use it for nanostructuring.

3.4.4 Strategy for Nanostructures using a Superhot Drop

3.4.4.1 Clusters Array by Drop Sliding

Drying of droplets as well as drying combined with flow phenomena has been utilized, for patterned deposition of solutes in DNA microarrays (236) and deposition of semiconductor nanowires or nanotubes onto functionalized substrates (237). Self organization of matter in regular submicro- and nanoscale lines of organic solution using wetting instability of a Langmuir-Boldget film (238,239) as a cost-effective way, has also been discussed.

In contrast to the above two step approaches using a cold drop, this part presents a novel, all-in-one droplet-deposition-based, template-free, and rapid (only a few seconds) approach for fabricating nanostructures. The general setup for the array patterning can be described with the help of an ”Anti-Lotus effect”. The Lotus effect (240) is famous for removing dust particles by picking them up an incorporating them in a droplet that is moving over the surface and thus cleaning it. The effect is based on surfaces forming spherical droplets with contact angles close to 180° (i.e. superhydrophobic) which enable the incorporation of particles as well as a reduced friction. In contrast to that an”Anti-Lotus effect” is used to deliver material from a superhot droplet by moving it over the surface. A sketch of the possible approach is presented in Figure 25a. A water drop loaded with diluted solution of the desired material is gently put on a hot substrate at 230 °C. The puddle was allowed to stay on the hot substrate for ~5 s on a fixed position before the substrate is tilted by ~30° to make use of the gravity as a propulsion force for the droplet, as seen in Figure 25b,c.

Conventional powders typically contain all types of grain sizes, including sub-micrometer- and nanometer- sized particles. For our experiments, a droplet was loaded with commercially available bulk zinc oxide powder. The resulting nanoclusters chains are shown in Figure 25d,e. In this case, upon droplet deposition and just before tilting, the particles separate on the basis of their sizes. Typically, the largest particles leave the droplet immediately, followed by the comparatively smaller particles, as illustrated in Figure 25f. Apparently, the deposited area provides several self-pinning points for the droplet, from where the cluster lines start to stretch. Thus upon tilting the substrate about 30°, several cluster chains parallel to the flow direction were deposited on the substrate simultaneously, as seen from the optical microscopy image in Figure 25g. The area I shows a comparatively larger range of cluster sizes representing the self-pinning area. Some of these will act as a center point for the line-stretching observed in area II, which has a significantly smaller cluster size range.

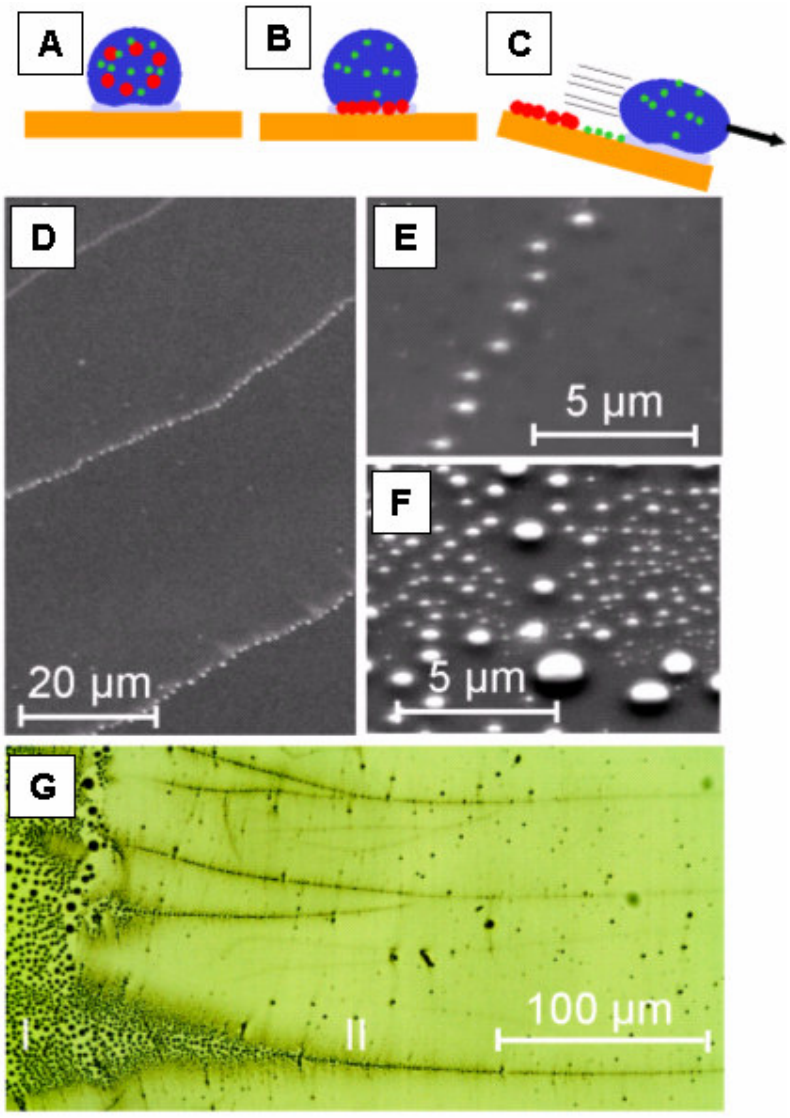

Figure 25: Line deposition by superhot drop: A) Sketch of a droplet loaded with particles levitating on its own vapor at the Leidenfrost temperature. B) Selective deposition from a Leidenfrost droplet. C) Illustration of a movement of the droplet by tilting of the substrate which creates the "Anti-Lotus effect", the delivery of particles in lines from the droplet. Particle size selection during the deposition of ZnO particles from suspension at the Leidenfrost temperature: D) SEM image of chains of ZnO particles with a quasi-similar size created by a running droplet, E) magnification of part of a chain from D, F). Before tilting the droplet, an area is created where grains of different sizes condense. (SEM micro graph) G) Optical Microscopy shows the transition between the area and the line (I is at the area before moving, II is at the line of clusters).

In such a way, a water droplet loaded with silver nanoparticles is able to release them in dense nanowires, Figure 26a,b. Wire formation requires a short range lateral attractive force which cause individual cluster to stick with each other. This will occur if the separation distance between the clusters is smaller than their diameter. The fusion observed is facilitated here by the non-passivated clusters and high temperature.

The interface chemical reactor underneath the drop enables various chemical reactions for the creation of nanoparticles. Here, using a drop of an aqueous solution and applying the Anti lotus method an all-in-one approach is realized where synthesis and patterning occurs simultaneously. Figure 26c shows a chain arrays of ZnO that formed by using a drop of zinc acetate, 10^{-3} M, and applying the sliding mechanism. EDX line scans across the cluster chains show the chemical composition of the wires and reveal that nearly all of the material is concentrated along the lines, Figure 26d. By the same way silver cluster chains are obtained from silver nitrate, Figure 26e. A homogeneous size of around 150 nm clusters with a separation distance of 200 nm can be produced. EDX line scans show the silver signal, see Figure 26f.

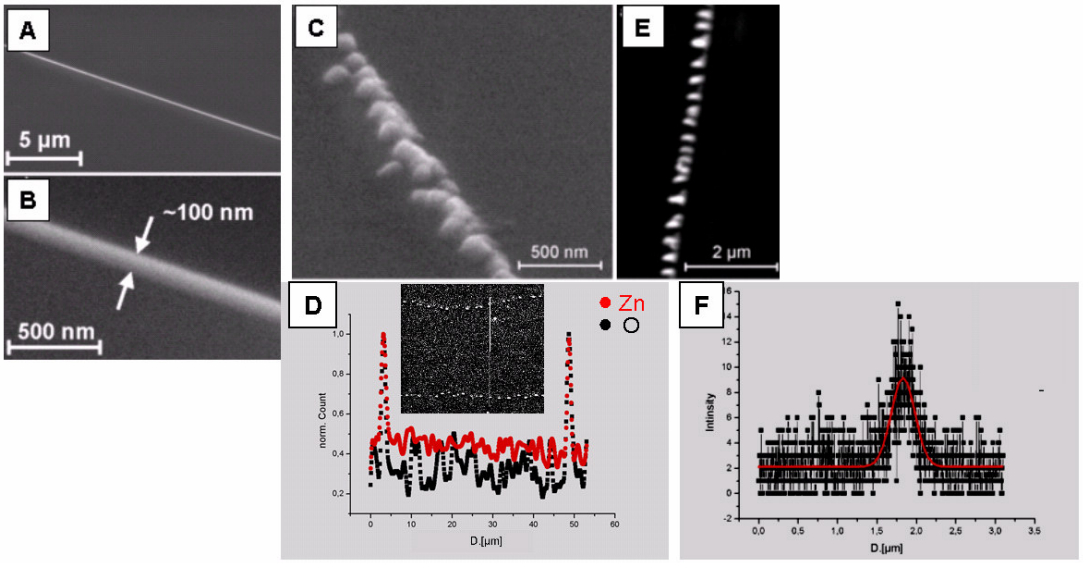

Figure 26: SEM images of different particles generated by anti-lotus: A,B) using silver nanoparticles (C, D) ZnO particles from zinc acetate with EDX analysis, (E,F) silver from silver nitrate with EDX analysis.

Temperature is an essential parameter for carrying out the experiment. As mentioned above the drop was allowed to stay on the hot plate for ~5 s before tilting the substrate so that the life time of the drop must be higher than this time. If the heat transfer limiting vapour happens to be loaded with salt, the salt might either increase or decrease the coefficient of heat transfer thus ultimately affecting the droplet evaporation life time (241). For instance, loaded droplets with life times of around 14-16 s, which is about a quarter of the life time of the virgin droplet of water (73 s), proved to be much longer at Leidenfrost temperature than at any other temperature, making room for our experiments. The decrease in the lifetime observed could be attributed to the increase in heat transfer within the droplet facilitated by the initially deposited particles.

3.4.4.2 Wires and Rings Patterning by Drop Impact

Flow is not the only possibility in fluid dynamics. There is also another interesting phenomenon known as drop impact. Impact of a cold/hot drop will results in a pancake film. In contrast, impact of a superhot drop is associated by drop explosion, where several secondary droplets are formed. Miniaturization of superhot drops is still questionable, several authors attribute this phenomenon to the influence of the rise in interfacial pressure created by the impact of the droplet with the surface at Leidenfrost temperature (242 and references therein).

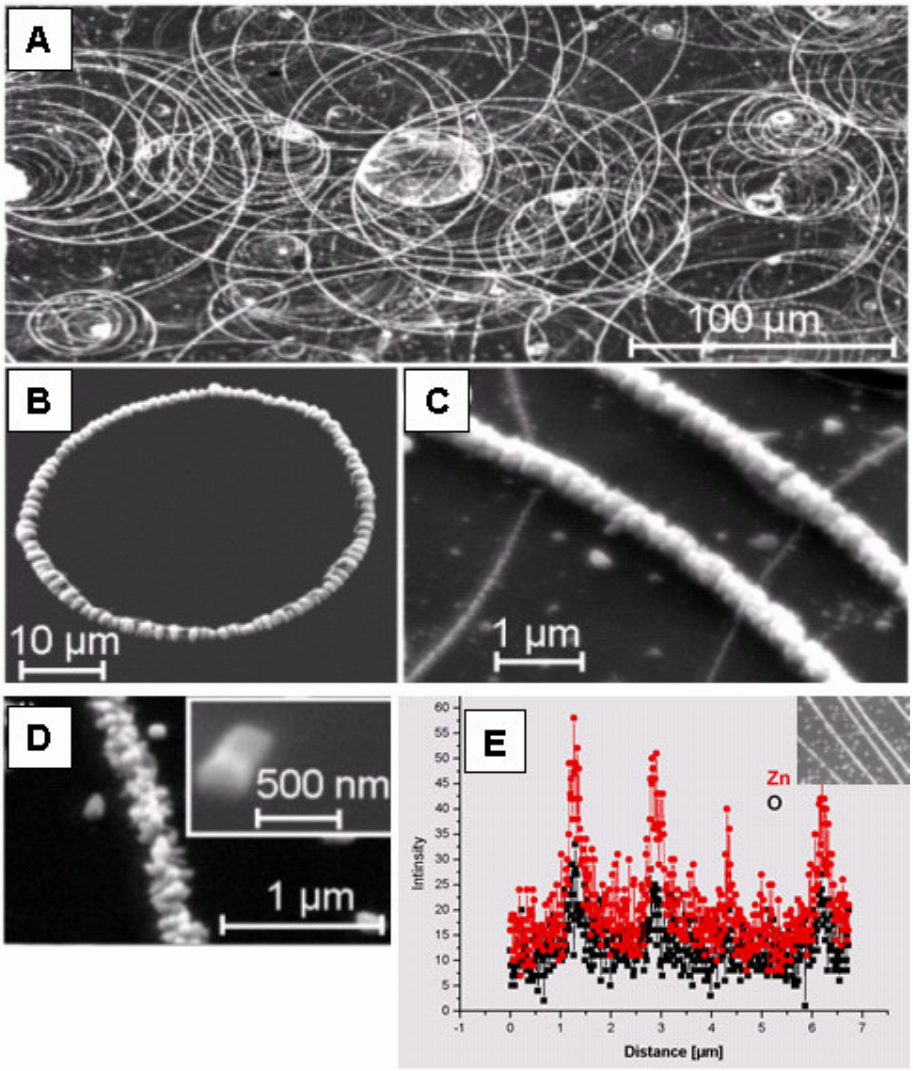

Figure 27: Optical microscopy images of ZnO rings formed by droplet disintegration at the Leidenfrost temperature: A) Overview showing intersecting ZnO circles, B) individual ZnO ring, C) rings of different sizes intersecting each other, D) Part of a ring, the magnification reveals the hexagonal crystalline character, E) EDX line scan reveals the formation of ZnO (intensity arb. Units).

Figure 27a shows the result of an impact from a drop loaded with Zinc-Acetate. Several rings are observed in the SEM micrograph. A typical single ring can also be seen in Figure 27b. Figure

27c shows a part of intersecting rings with different radius and periphery width indicating the polydispersity of the secondary droplets formed up on drop miniaturization. A magnified view of part of a wire, Figure 27d, shows that the resulting structures that are composed of a dense assembly of nanorods revealing the hexagonal crystalline character for ZnO, see inset, which is also verified by EDX shown in Figure 27e.

Ring structures with a superhot drop is not only restricted to semiconductors. Also metallic circles and intersecting arrays can be achieved by using a drop of 10^{-3} M AgNO3. Optical microscope images of a part of intersecting chain arrays and isolated rings of nanoparticles are shown in Figure 28a,b respectively.

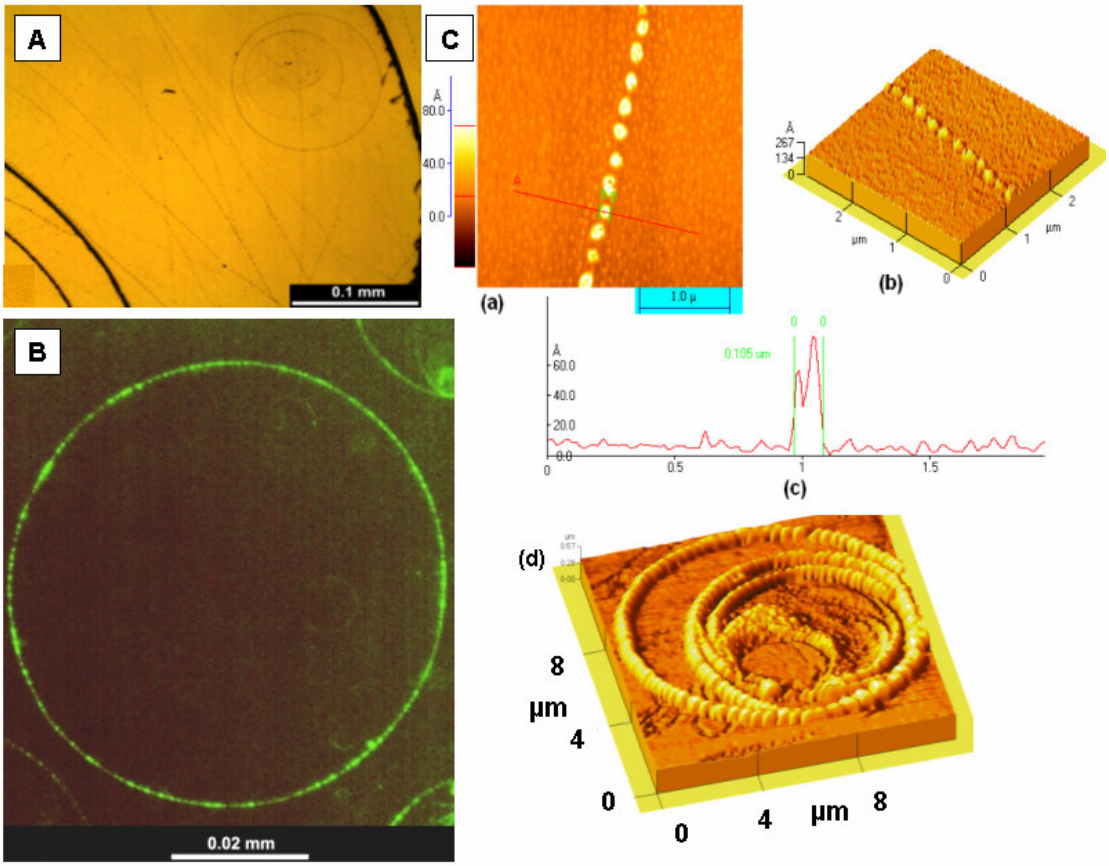

Figure 28: Images of discontinuous rings and wires formed by droplet disintegration at Leidenfrost temperature using lower concentration, 10-3 M: A) optical overview of intersecting structures obtained upon drop impact, B) individual silver ring composed of nanoparticles, C) An AFM images of: (a) silver cluster chain, (b) 3D topographical representation revealing that the particles are quasi monosized, (c) line scan showing a nanoparticle diameter of about ~ 105 nm and confirming the absence of particles in the neighboring regions of the lines, (d) multiple concentric nanoparticulate rings have been formed with this approach.

Further examinations were carried out with the aid of the AFM, Figure 28c, that shows how the particles are almost monodispersed with size of about 100 nm and the ratio of gap to a particle

diameter is unity. Additionally a micrometer of nanoparticulate multirings formed by this approach is also shown.

Further investigations on more diluted solutions were also done. Here silver nitrate aqueous solution with concentrations of $c=10^{-5}$ M was used. Upon impact a similar behavior like in the case of 10^{-3} M was observed. Intersecting structures, multi rings/wires as well as free rings, were obtained.

Surprisingly, the structures obtained here show a tendency to form continuous wires and rings, instead of doted structures observed earlier by10^{-3}M. Continuous structures of a free range and intersecting wires are observed by optical microscope and AFM as shown in Figure 29a,b,c,d respectively. This observation is also confirmed by further examinations with the SEM where Figure 28e shows an area of intersected solid wires and Figure 29f reveals clearly the continuity of the silver wires. EDX, Figure 29g confirmed the successful chemical transformation and shows a pure silver signal.

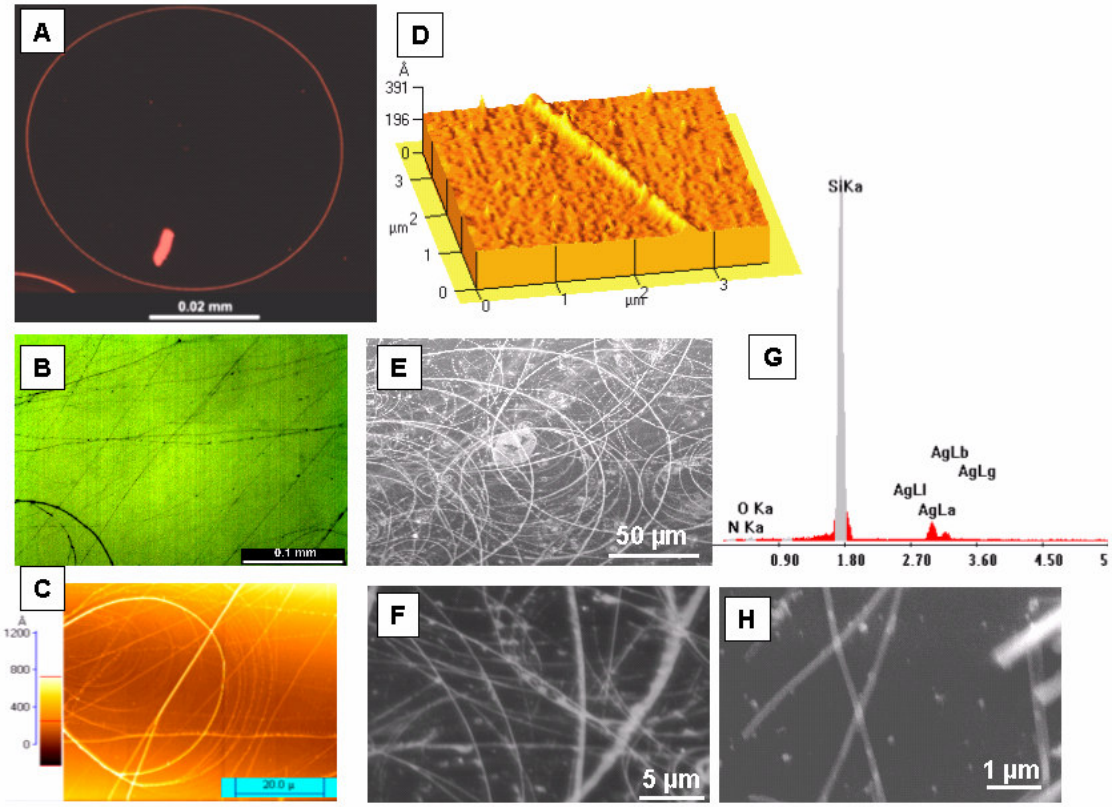

Figure 29: Images of continuous rings and wires formed by droplet disintegration at Leidenfrost temperature using lower concentration,10-5 M: A) Optical image (DF) of individual silver ring, B) Optical image overview showing intersecting structures, C) AFM overview of the contentious nanostructures, D) 3D representation of an AFM image shows a part of a smooth wire, E) SEM overview shows the intersecting rings and wires, F) Higher magnification of the last image reveals the continuity of the wires, G) EDX confirmed that the structure composed of silver ignoring the signal from nitrogen/oxygen, H) Smooth wires can also be obtained using Zn-acetate, revealing the concentration dependence of this behaviour.

To investigate weather the observed behavior is dependant on the chemistry or on the concentration, a drop of 10^{-5} M of zinc acetate is used. As shown in the SEM images, Figure 29h, smooth wires rather than chains were observed, which reveals a concentration dependence of the structures.

Furthermore, the structures obtained here for both concentrations which are done on a silicon substrate are also found using a quartz glass substrate. This allows investigations of the optical properties of both structures which will be shown in the next chapter.

Indeed, the stretched lines and the circles obtained upon impact at Leidenfrost can be regarded as fluid chemical reactors where a nucleation and growth of the nanostructures occurs.

For a particular solvent, there is certain solubility for a solute, an addition of any excess solute will result in precipitation and formation of nanocrystals. Thus, in the case of nanoparticles formation, for nucleation to occur, the solution must be supersaturated. That can be achieved either by directly dissolving the solute at a higher temperature and then cooling to low temperatures or by adding the necessary reactants to produce a supersaturated solution during the reaction (243,244). The precipitation process basically consists then of a nucleation step followed by a particle growth stage. The driving force for both stages is the reduction in the Gibbs free energy; a solution with solute exceeding the solubility possesses a high Gibbs free energy, so the overall energy of the system would be reduced simply by segregation of solute from the solution. However, the important parameter to explain the result above is simply the critical nucleus size r*, which can be obtained by setting $\Delta G/dr = 0$ and so

$$r^* = 2v\gamma/3k_BTln(S) \tag{3.10}$$

where v is the molecular volume of the precipitated species, γ is the surface free energy per unit surface area, and kB is the Boltzmann constant, T is the temperature and S is the saturation ratio, where the saturation ratio is = $(C_i\text{-}C_0/C_0)$ where C_i , C_0 is the initial solute concentration and the equilibrium concentration respectively.

The above equation shows, that the higher the saturation ratio S (higher initial solute concentration), the smaller the critical nuclei size r* will be. That means that the growth time of the nuclei decreases with the concentration of the solution. Furthermore for a given value of S, all particles with $r > r^*$ will grow and all particles with $r < r^*$ will dissolve.

As both experiments were carried out under the same condition, (temperature, drop size, etc), it turns out that a small stable nuclei with a short growth time is established by 10^{-3} M hence the growth continues to form a dot array whereas nuclei formed within the lines/rings by 10^{-5} M are metastable and undergoing coalescence into elongated supcritical nuclei hence a smooth wire is formed.

Indeed the uniformity of the size distribution observed at the concentration of 10^{-3} M at the Leidenfrost condition is achieved through a short nucleation and growth period which prevents a depletion effect. If the reaction time is sufficiently long, the monomer concentration should drop as the reactants are depleted due to particle growth "Ostwald ripening" and defocusing will occur, where the larger particles continue to grow, and the smaller ones get smaller and finally dissolve. But, if the reaction time is short, then a "self-sharpening growth process" occur (245, 246). As the saturation ratio (S) decreases the corresponding critical nuclei size (r*) increases according to eqn (3.10), a new critical size is achieved so that any particles smaller than this will merge "dissolve in each other" together. Essentially, each nucleus acts as a seed for further growth and is present at the end of the reaction as an individual particle. Accordingly smaller particles grow more rapidly than the larger ones where focusing in size occurs, and nearly monodispersed size distribution can be obtained.

Indeed the vapour collapse underneath the droplets/lines generates an automatic cut off and achieves an optimal condition for a self-sharpening process through a short nucleation period that generates a monodispersed size distribution of the particles at the end of the reaction.

3.4.4.3 Integration into Mask Approach

To take a fabrication process beyond the small scale of the laboratory, it is important to be able to achieve an exact placement of the nanostructures on a substrate. That can be achieved by combining the drop with a top-down strategy. A micropatterned grid with square-type holes of 50 µm by 50 µm, which is typically used for transmission electron microscopy (TEM) sample preparation, was employed to predefine the arrangement of the structure. By simply placing the TEM grid onto the hot silicon substrate during the process of impact deposition, the large droplet became divided equally into smaller droplets, each forming a 50 µm by 50 µm pool. It was found that the best organized structures were obtained from a drop falling from a height of ~2 cm. This height is optimal, because the impact energy from this height is relatively small, therefore the disintegrated droplets are less spread out over the TEM grid. Figure 30a shows a large area covered with ordered concentric rings. The atomic force microscopy (AFM) image, Figure 30b, shows a part of the concentric ring system that was formed at each pool site. A low-magnification image (optical microscopy, dark field) in Figure 30c confirms the regularity of the pattern obtained without any further optimization.

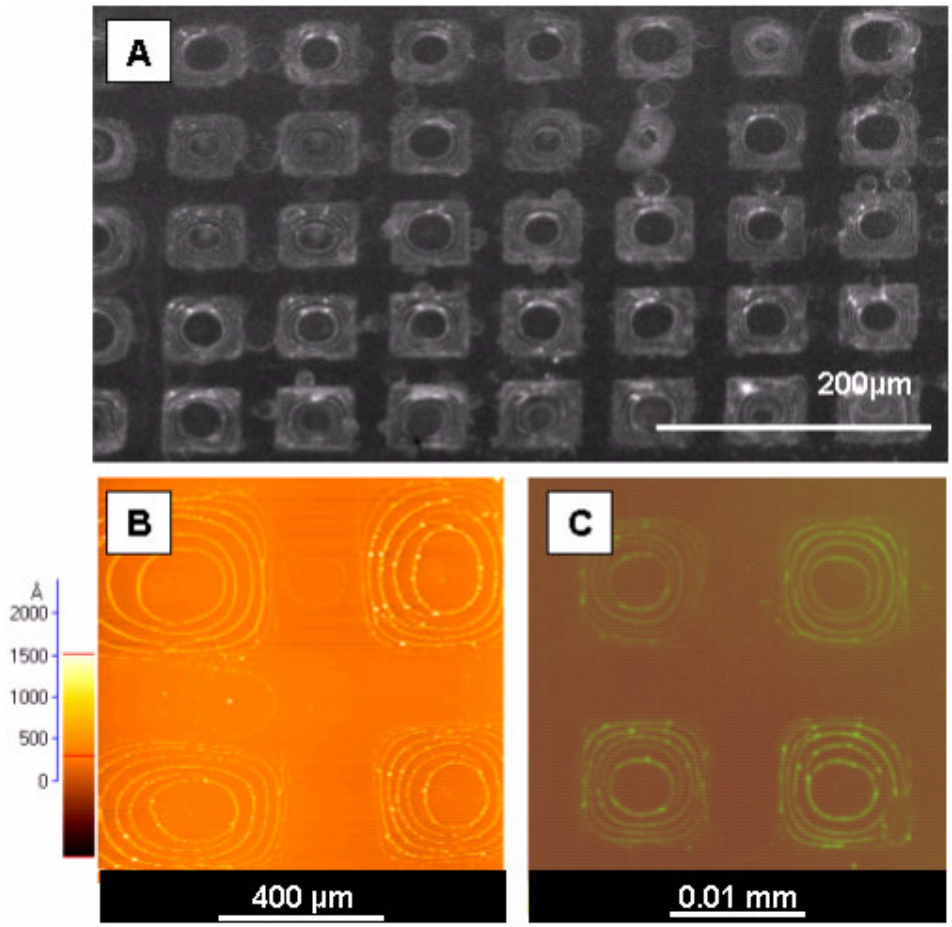

Figure 30: Ordered concentric rings by combining the drop with a top-down strategy: A) SEM overview of a concentric silver rings system which is aligned with help of a TEM grid, B) an AFM image shows a part of a concentric silver ring system, C) Dark field optical microscopy image gives an overview over the reproducibility of the aligned ring systems.

3.5 Drop Approach--Summary and Outlook

Nanostructuring accompanied by a chemical reaction directly onto a substrate via solvent evaporation using a drop on a hot plate is demonstrated here. Covering a large area with nanoclusters, wires or rings in a rapid, cost-effective manner is generic for this process. Dilute concentrations of solution and precise control of the thermal aspects are emphasized in this study.

The possibilities of nanostructuring using a drop on a hot plate were investigated with two types of drops, namely the hot drop at 80 °C and the superhot drop at 230 °C.

For the hot drop it was found that mainly the physical properties of the solvent control the form and shape of the deposited structures and not so much the chemical composition of the diluted solution. However, stochastic, micro-sized rings were obtained by an evaporation of a hot drop. Therefore, a new and simple approach based on ***d***eformation accompanied ***d***ewetting of the contact line around a ***d***efect, "D^3 or DDD" is introduced. A hot drop around a circular defect was found to form a gradient of rings, whereas a cylindrical tube highly reproducible regular gradient pattern of parallel arrays was formed. The height and the width of the wires as well as their spacing tend to decrease gradually with increasing proximity to the axis of the cylinder. Structures, down to nanometer range, i.e. below, < 100 nm in a precisely controllable manner, are realized in this approach. Note that after the finding of the "DDD", only a first optimization was performed; the method has a high potential for further optimization. For instance, complex structures like grids with gradient mesh sizes were made by successive deposition using the D^3 approach.

The idea of using a salt solution rather than nanoparticles opened a new possibility of a subsequent controlled chemical reaction on the deposited lines. For instance, here, thermal decomposition of $AgNO_3$ is used to form smooth silver lines; however, primary results show a formation of nanoparticle chains if the transformation occurs under UV-light irradiation.

However, the process is not restricted only to salt solution, as nanoparticles can be also aligned in the same way.

Going beyond the boiling point of a liquid, and using a superhot drop at the Leidenfrost temperature, a novel "all in one" template-free method to generate and deposit nanoclusters to form chains, wires and rings using suspension or solution droplets is realized. The rapid synthesis of nanostructures with timescales equivalent to the stability of the liquid droplet at the Leidenfrost temperature (10-15 s) without complex chemicals or sophisticated equipment is generic to this process. The overheated vapor interface underneath the superhot droplet is utilized as a new chemical reactor permitting a novel nanosynthesis.

A combination of flow dynamics and chemistry enables various forms of surface structures to form. Anti-Lotus technique provides the possibility to form a large area of array. Nanoparticle lines with lengths in mm range are formed by drop sliding.

Impact technique is also utilized here as a new tool for nanostructuring. Miniaturization of a superhot drop facilitates the formation of intersected complex structures, which are composed of smooth or dotted rings/wires reflecting the concentration effect. This process covers large areas with nanostructures as it can easily be performed in parallel with many droplets; therefore, within the same time frame, one can cover areas of any arbitrary size with the nanostructures.

By combining this approach with a simple mask strategy such as TEM-grid, the rapid large-scale fabrication of well-organized nanoscale morphologies appears realistic.

In general, drop on a hot plate is a new, environmentally friendly system for the direct production, deposition, and patterning of nanostructures on a surface. Furthermore, this approach is generic and could easily be modified for many chemicals with very few limitations. As the author believes that an understanding of the phenomenon is the key parameter for a controlled work and further progress, a qualitative discussion describing a possible mechanism is given.

The high interest in the first Publication "*Anti-Lotus Effect for Nanostructuring at the Leidenfrost Temperature*" that covers part of the research performed here can be seen as an indicator for the potential of the method. Several secondary comments were given in:

A) Front cover of ***Advanced material*** "Volume 19, Issue 9, (May, 2007) "

B) ***Nature Nanotechnology***, News and Views, "Drip painting on a hot canvas" 2, 344 - 345 (01 Jun 2007)

C) ***Nanowerk-Spotlight*** "Applying a 250-year old discovery to nanotechnology" fabrication (May, 2007), http://www.nanowerk.com/spotlight/spotid=1907.php

The Metastable chemical reactor "MCR" permits a new method for the nanoparticle synthesis in a beaker (Lab-In-Beaker) under an ambient atmosphere. However, the possibility of using such a reactor in a polymerization technique or simply for preparing a composite/hybrid material is not examined yet, but it is planned for future investigation.

The method used for grid patterning can be applied also for the preparation of multilayer nanostructures simply by multiple depositions on a fixed defect position.

Furthermore, the gradient nature of the structure formed by DDD approach facilitates the investigation of the dependence of optical, electrical, and transport phenomena on size and width of the structures.

However, there are still a lot of questions regarding the topic, such as the possible influence of the substrate, humidity, temperature, pressure, concentration, solvents, and drop size on the patterning. The research in this topic will continue where more investigations and also the integration of the obtained structures in a nano-device will be made.

4 General Conclusion and Outlook

In this thesis, a new paradigm for producing lateral nanostructures directly on a substrate is realized using unconventional ways.

Cracks are a hierarchical phenomenon and found in nature in a wide variety of scales, even in a nanoscale. Cracks have a bad reputation due to the fact that they occur during mechanical failure of materials. On the other hand, cracks follow strain fields and can be tolerably controlled in width, length, and density; therefore, they are considered to be ideal templates for nanowire deposition.

The process begins by depositing a brittle thin film on a flexible substrate by spin coating or simply by spray coating. Nanoscopic cracks were formed by inducing mechanical stresses in the film, either by differential thermal expansion with the substrate generated by thermal cycling, simply by mechanical bending or thoroughly swelling the substrate in an appropriate chemical environment. Once cracks are formed, these can be used as templates for horizontal nanowire formation by depositing material into the cracks using physical deposition techniques. By mask lift-off of the brittle film, nanoscale structures that decorated the surface are left behind.

Several examples are presented which show how these mechanisms of mechanical failure of thin films can be turned into useful templates for various nanostructures.

Hierarchy network of wires that covered a large area in a dry mud-like fashion have been fabricated.

The advantages of the fracture approach have been successfully combined with the advantages of the nano-shadow-mask approach, permitting a novel shadow mask for vacuum deposition.

Cracks with delaminated sides were used as templates for the deposition of ordered parallel wires (which are even smaller than the openings) by evaporation around a critical angle, which can theoretically reduce the widths of the obtained nanowires. They were also utilized as templates for the deposition of pairs of parallel wires consisting of similar or different materials with only a few nm separations. In spite of this, nanowires with a width of less than 40 nm or nanogaps between two parallel wires of less than 50 nm have been fabricated without further optimization.

A one-step device where nanowires are suspended between two electrodes in an organized manner has been realized by integration of cracks approach into standard microstructures created by photolithography on a ridged silicon substrate. The cracks can be controlled by the microscopic geometry of the thin film. Applying stress to the thin film with a form of a bow tie leads to mechanical failure right in the middle of both triangles, whereby wafers containing microchannels in a zigzag pattern were found. In both cases, nanowires between contacts are realized by deposition.

Away from the physical deposition, a new approach of chemistry and patterning direct on a substrate that based on a drop on a hot plate is developed.

Sprinkling a drop of water into a hot skillet is an everyday event that can be observed by anyone in his own kitchen. The persistence of water drops on a hot surface was first investigated by the German physician, Johann Gottlieb Leidenfrost, "A Tract about some Qualities of Common Water" in 1756. When water touches the hot plate, the bottom part of the water vaporizes immediately. The drop is not any more in contact with the solid but levitates above its own vapour. The temperature, at which the drop dances and such levitation phenomena generally occur, is named after Leidenfrost.

Another demonstration of the same principle would be that a thin vapor film is built underneath the water film when it is suddenly heated (film boiling) and then provides temporary protection against further heating in the same way as it occurs in the Leidenfrost drop phenomena.

This effect is used and introduced here as a new tool for green nanotechnology.

Under Leidenfrost conditions (230 °C), water possesses two interfaces, a top interface (air/water, called "cold interface") and a bottom one (water/vapour, called "hot interface").

The hot interface formed underneath the water/drop at Leidenfrost conditions permits a novel concept of "Interface chemistry at the bottom surface of water" that enables a green synthesis of nanocomponents in a beaker using a water film (Lab-in-Beaker) or directly onto a substrate using a drop (Lab-in-Drop) in a rapid (10-15 sec.), simple and hazardous-solvent-free and/or reducing-agent-free process, using only an aqueous solution of the desired nanomaterials.

The fluid dynamics of a drop on a hot plate at the transition regime are totally different compared to evaporation and boiling regimes. For instance, sliding of water drops on a wettable substrate becomes easier by the reduced friction due to the underlying vapor film. Furthermore, drop impact is very different. Impact of drops at evaporation/boiling regime will result in a pancake film, whereas impact of a drop at the transition regime is accompanied by an explosion, in which several 'daughter' droplets are formed. These phenomena are utilized here as new nano-design tools.

Fluid dynamics at Leidenfrost enabled the creation of a new type of a "mobile deposition machine" where the drop containing the desired material is moved over a surface and deposits material along its way. By merging fluid dynamics (drop sliding/impact) with the chemical reactor underneath the drop at Leidenfrost temperature, a novel "all-in-one" approach is realized where synthesis and patterning of nanocomponents occur simultaneously and directly onto a substrate. In spite of this, mm^2 area of parallel nanowires, nanocluster chains as well as free and intersecting rings with a width of less than 100 nm have been fabricated without further optimization.

Highly ordered patterning with deposition occurring in an exact position was realized by integrating the drop approach into a mask approach. Concentric rings are formed upon drop impact on a TEM grid that covers a silicon substrate.

In contrast to a Leidenfrost drop that shows a hydrophobic behaviour, a drop located on a hot surface at a temperature below its saturation point will wet the substrate. If the drop is loaded with material, a pattern (mostly ring shape) is left behind upon drying. Here it was shown that the evaporation mode as well as the physical properties of the liquids control and regulate the form and shape of the structures that will be finally obtained. This is largely independent of the dissolved material under diluted conditions. For instance, a single ring was formed by drying a loaded water drop at RT where several rings are formed when drying occurs at 80°C. However, drying of a free drop on a hot surface (50-80 °C) results in macroscopic, discontinuous, and stochastic patterns.

For a controlled ordered pattern, i.e. parallel arrays, network, ring, etc., a new strategy "DDD" is developed that combines the **d**ewetting aspect of an evaporating **d**rop/ thin film at 80 °C, with another old aspect, namely, deformation of a liquid (i.e. water) contact line around a wettable **d**efect.

The process begins by depositing a drop of desired material onto a substrate that contains a passive defect (i.e. tube on a substrate) or active defect (engraved onto substrate). The entire setup is put on a hot plate at a temperature of 80 °C. Upon drying, a well-organized gradient pattern that starts at a certain critical distance (~ defect radius) is formed. The change of the wetted defect cord during evaporation controls and regulates the form and shape of the structures; hence a gradient pattern is finally obtained.

Moreover, complex patterns like grids have been fabricated by performing consecutive depositions. In that way lines are formed by a first deposition around the tube. Turning the tube by 90° and applying a second deposition results in a grid network of wires. However, even with this DDD approach, nanowires, rings and meshes with a width of less than 100 nm have been successfully fabricated without further optimization.

The wire materials were fabricated by localized chemistry on the surface. Simply, a salt solution was deposited and then the chemical transformation to the desired material was done directly on the substrate surface.

Still, every approach has its limitations and advantages.

Regarding the fracture approach, a detailed control over the crack openings is still a challenge. For instance, cracks formed on flexible substrates by applying uniaxial stress to the film while bending can be closed when released. Another case is delamination of cracks which led to local shadowing, which in turn prevents the nanowire material from reaching the substrate during deposition. A poor opening

of buckle-driven delaminated cracks was also sometimes observed at the confined channel in a microstructured substrate. Any of those events can result in the discontinuity of the wire that can lead to difficulty in electrically connecting them. Moreover, controlling parameters like film thickness, exposition time, and exposition temperature of the Photoresist on a hot plate have to be optimized in advance. Mask lift-off is also a very critical step and still a challenge for this approach. The extended exposure of the nanowires to the ultrasonic bath while removing excess material has also the unwanted consequence of destroying the wire or increasing the gap between the grains, or even re-deposition/adsorption of the dissolved polymer on the wires. With the possibilities for micro fabrication created by the clean room that is under construction right now, these difficulties can be overcome.

In contrast, a template-free approach, such as in the case of the drop approach, avoids this problem, as no microstructure fabrication is necessary.

However, there are other limitations regarding the drop approach. For instance, to create a regular pattern by DDD approach, control of parameters like solvent, concentration, and temperature have to be optimized for each material. The same is also true for the Leidenfrost drop. Creating nanoparticles at the hot interface is dependent on the stability of the hot interface. Consequently any perturbation of this condition will affect the efficiency of such reactor. Even with that being so, a remarkable reproducibility of ~ 50% can still be achieved this way. It is very likely that the reproducibility will be drastically increased by reducing contaminants like dust on the sample surface. Also this can be done by fabrication in a clean room.

Nevertheless, both approaches possess a lot of advantages.

Growing nanowires in cracks has a number of advantages, including a high aspect ratio (extremely thin, but very long nanowires), the ability to form straight or complex branched networks, the possibility to orient nanowires via strain fields, and the ability to grow into other micro- or macroscopic structures. The technique has the potential of generating a pattern of nanowires that are formed according to a prescribed pattern on a surface. Such crack templates are cheap and simple to generate, and a wide range of materials and host substrate can be used. This should give many labs without cutting-edge equipment a possibility to form complex nanostructures.

The drop on a hot plate method permits a novel approach for nanosynthesis and patterning on a substrate as well as following the trend of green nanotechnology which is characterized by:

- Being an environmentally friendly method: water is used as a solvent and reactor Safe chemical
- Safe chemical synthesis: only salt/water is used (non-toxic precursors, no hazardous organic solvent, reducing agent, surfactant, absence of chemical derivative etc.).

- High atom economy: The final product contains the whole amount of the starting materials.
- Low waste: very low waste for beaker methods and almost no waste for drop methods.
- Cost effective: inexpensive--only a hot plate, salt solution, pipet are required.
- Energy and time efficient: 15 sec. Process.
- Scalability: especially for "Lab-in-beaker" processes.

Furthermore the drop on a hot plate method still has a larger potential than one might think. Figure 1 shows another possibility for creating different types of nanostructures like vertical wires or even nanotubes.

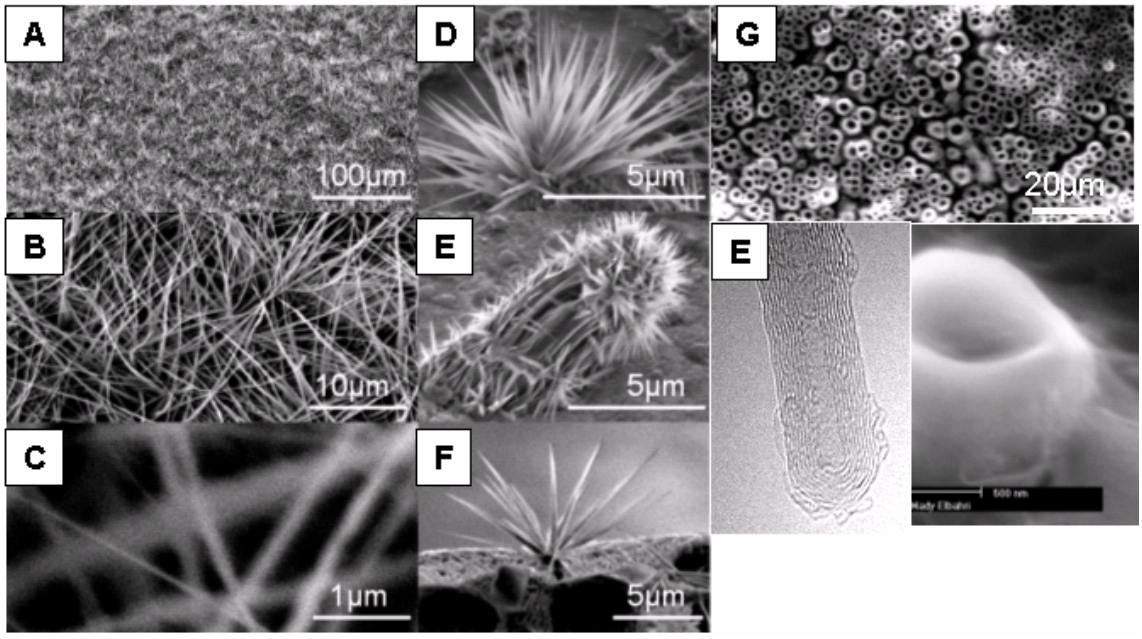

Figure 4.1: Microscopy images of vertical nanowires with various structure using a drop at Leidenfrost temperature: A-C) Grass of upstanding nanowires, D-F) "agaves" , "sea cucumbers" and "sea urchin" like nanostructure, G,E) meso and nanotubes.

However this part is still under investigation but it is included here to visualize the versatility of the drop approach.

In general, one could say that both approaches presented here offer a powerful approach to direct manufacture of nanowires on a substrate. Nevertheless, both approaches belong to the same category (self-organization approach), in which functional structures are assembled from well-defined chemically and/or physically synthesized nanoscale building blocks.

One-dimensional nanostructures represent the smallest dimension for efficient transport of electrons and photons, and thus are ideal building blocks for a hierarchical assembly of functional nanoscale electronic and photonic devices (247,248).

Nanowires obtained here, regardless of their preparation method, may serve as connectors for other nanostructures. These can be a challenge when developing nano-devices and circuits in nano electronics.

The optical properties of the metal nanowires are somewhat exotic. In contrast to metal clusters showing a Mie resonance (249), the optical properties of nanowires are governed by their geometry and by the plasma-like response of a free electron gas inside it. Such a kind of surface wave, known as surface plasmon polariton (SPP) (250), can propagate along a metal-dielectric interface of a long wire. The concentration and channelling of light using metal nanowires in a wave-guide-like fashion by, e.g. plasmon polariton tunneling, is assumed to be promising for a new generation of photonic devices (251,252,253,254).

As one can see in Fig 1a, silver wires made by the fracture approach (shadow mask) on a polymer substrate, show only one plasmon peak @ 400 nm which appears to be shifted towards the asymptotic value in the range of 380 nm.

Closely resembling the silver wires formed by the fracture approach, the continuous silver wires are obtained by drop impact at the Leidenfrost temperature on a quartz glass with a concentration of 10^{-5} M show a similar behaviour (see Figure 2b), black. The results obtained here for the continuous wires regardless of their preparation method are in good agreement with the observed SPP value for high aspect ratio nanowires as well as the expected behaviour from long wires (255,256).

However, in contrast, the discontinuous silver wires (obtained with 10^{-3} M, by drop approach,) show two peaks @ 408 nm, 610 nm (see in Figure 2b, red). Recently, it was found that electromagnetic energy transfer at optical frequencies can occur between closely spaced metal nanoparticles via near-field coupling (257,258). Therefore, it is reasonable to assume that the influence of the coupling between the clusters in the chain gives rise to plasmon-plasmonic coupling, which is reflected in their spectrum of plasmon resonances.

Plasmonic coupling between nanoparticles is used in a wide range of applications, including biosensors (259) and new optical devices (260). Since the coupling is associated with large

electromagnetic fields near the particle surface and in the gap between them, this enhancement can be so large that it allows single molecule detection (261).

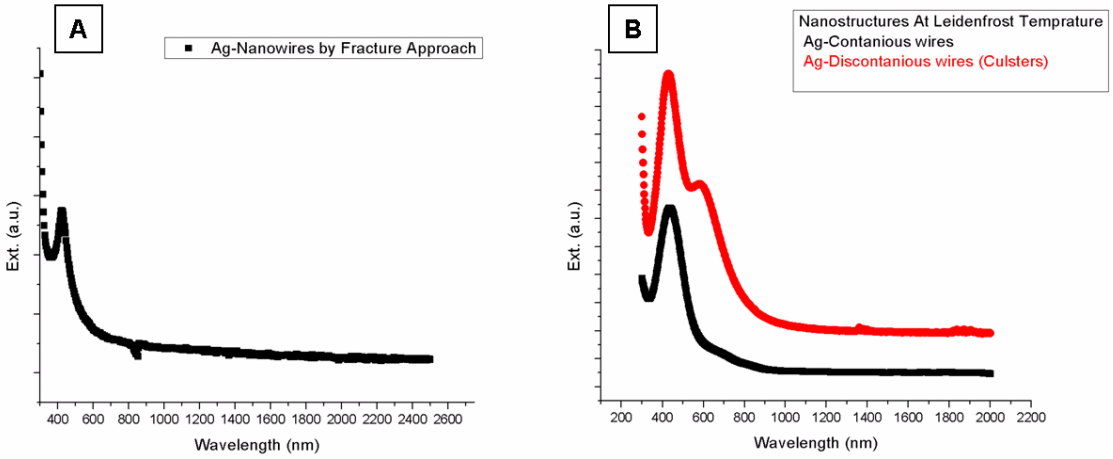

Figure 2: Optical properties of silver nanowires done by A) Fracture approach, B) Drop approach.

Sensing of important molecules for environmental or security-checking purposes may be considered as one of the major applications of nanowires (262,263). The extremely high surface to volume ratios achieved with these nanostructures makes their electrical properties extremely sensitive to species adsorbed on their surfaces. The mechanism envisaged involves adsorption (or possibly diffusion) of analyte molecules at the surface, which induce a change in the electrical resistance of the nano-objects. One principle of a sensor based on nanowires is to use the nanoscale gaps in the nanowires (264). Molecules, deposited into the gaps could provide a better conductivity because they bring some density of states into the gap and thus allow a hopping conductivity rather than tunnelling.

Unlike the traditional Pd-based hydrogen sensor that detects a drop in the conductivity of Pd upon exposure to hydrogen, the Pd-nanowire sensor measures an increase in the conductivity. The reason for this is the Pd wire consists of a cluster of Pd particles separated with nanogaps. Conductive paths form due to the closure of these gaps in the presence of hydrogen molecules as Pd particles expand in volume. The expansion of Pd particles is due to the penetration of atomic hydrogen which results from the disassociation of adsorbed molecular hydrogen onto Pd particles (265).

In order to use our nanostructures they have to be electrically connected. For this purpose a first attempt of contacting the wires has been successfully done as shown in Figure 4a. Metallic wire done by fracture show a linear I-V curve as seen in Figure 4b. However systematic investigations of the electrical and sensing properties of nanowires done by the fracture approach have already been started in the framework of anther PhD thesis.

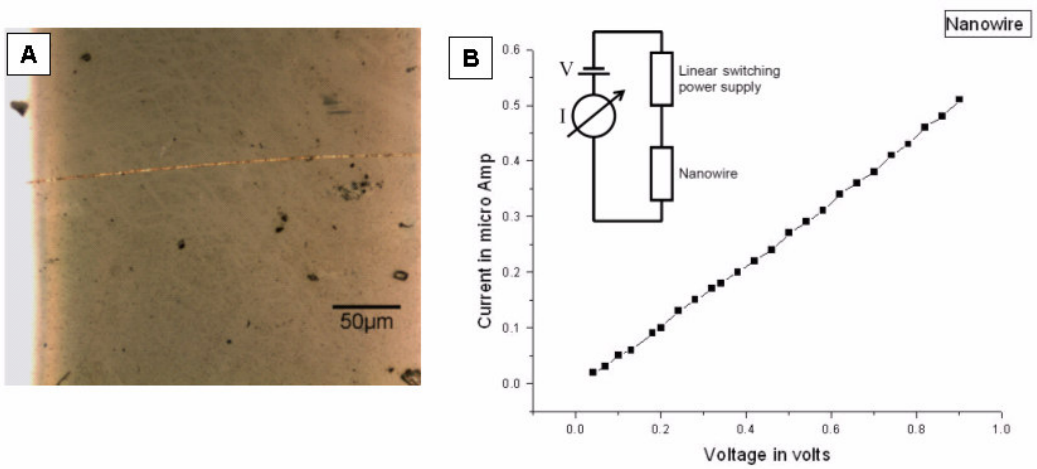

Figure 4: The conductivity of the nanowires: A) Gold nanowires suspended between two gold electrodes, B) schematic circuit diagram of the conductivity measurement with I-V curve show the conductivity of the nanowires.

Semiconductor nanowires have promising applications in nano-electronics, nanophotonic, and sensoric devices (266). The multifunctional semiconductor metal oxide, ZnO, has attracted significant attention as a candidate for chemical and biological solid-state sensors. This is because their electrical conductivity is highly dependent on the nature and concentration of the surface adsorbed species. The Zn ion with a mixed valance and oxygen vacancies of the nanoscale ZnO structure are responsible for the observed high sensitivity of electrical response to the presence of adsorbed molecules (267).

However, those studies have been made on single crystalline and show their properties due to the relatively high surface-to-volume ratio. Here, nanowires/rings done by drop approach consist of an agglomerate of nanorods, given potentially a much higher surface area than the single crystalline ones. Furthermore, at the contact points of the individual rods they possess so-called "chemically responsive interparticle boundaries" CRIBs (268) which are known to enhance sensory properties.

Photoluminescence (PL) spectra of ZnO bulk single crystals have been investigated in detail and considerable progress has been made in the last few years in explaining the origins of different ZnO luminescence peaks (269,270). Most ZnO nanowire PL spectra are reported for randomly oriented or aligned nanowires since the lateral resolution of the primary laser beam in PL is limited to about only 1µm due to optical limitations (271). Room temperature luminescence of ZnO wires shows only one very broad peak structure and therefore does not give much insight into detailed impurity related recombination processes as demonstrated in the low-temperature luminescence of ZnO bulk single crystals (272,273). Few reports for the low temperature photoluminescence experiments on ZnO nanowires identify the free exciton and three donor-bound exaction PL peaks (274). These are generally the strong ultraviolet band (around 386 nm), very weak blue band (around 480 nm) as well a negligible green band (around 580 nm). The green band emission corresponds to the singly ionized

oxygen vacancies and results from the recombination of the photogenerated hole with the singly ionized charge state of this defect. Recently, room temperature UV lasing emission (275) and high UV lasing efficiency of ZnO nanorods (276) have been reported.

Field emission is one of the many applications of one-dimensional nanostructured materials. Characteristic properties of semiconductor nanowires like wide band gap, thermal stability and oxidation resistance make it a good candidate for field emission (277). Highly oriented vertically aligned nanowires have been shown to have enhanced field emission properties (278). Tip morphology is also an important factor because sharper tips increase the effective electric field at the tips (279).

Chemical treatment of ZnO formed by drop approach, other morphology like spheroid and nanowires with a sharp tip can be realized (see Figure 5).

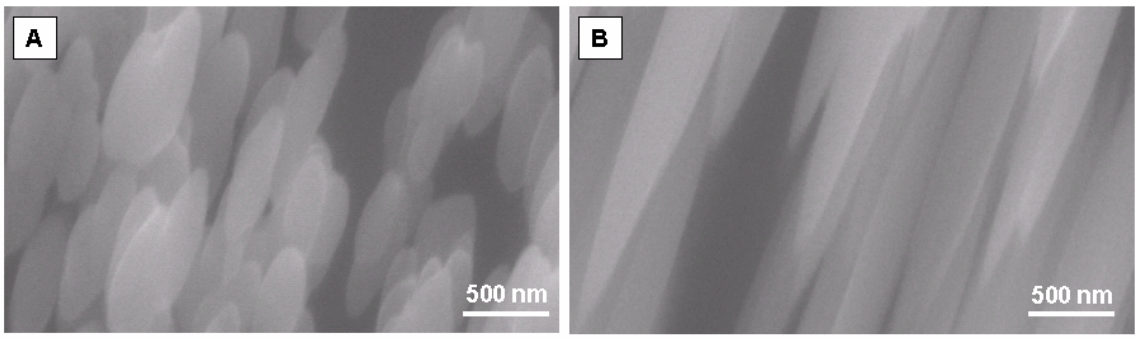

Figure 5: ZnO with different morphology: A) Spheroid, B) wires with sharp tips.

In spite of the elegance of the drop approach, the electrical, optical, and sensoric properties of those nanostructures remain to be tested, so their usefulness as a test device is still under investigation.

But nevertheless, it is more likely to say that both approaches "Fracture/ Drop" presented here offer a powerful alternative approach to the conventional methods and each of them represents

"unconventional nanomanufacturing on a substrate".

5 Appendix "Experimental equipment"

5.1 Vacuum Deposition Techniques

The most important methods to deposit thin films in vacuum are evaporation and sputtering. Evaporation removes atoms from the source by thermal means, whereas sputtering does this using mechanical means. In the framework of this thesis both methods are used. The deposition chamber is shown in Figure 1. In case of fracture approach deposition of the adhesion promoter, Cr, was done by evaporating where the wire material "" is mainly deposited by sputtering.

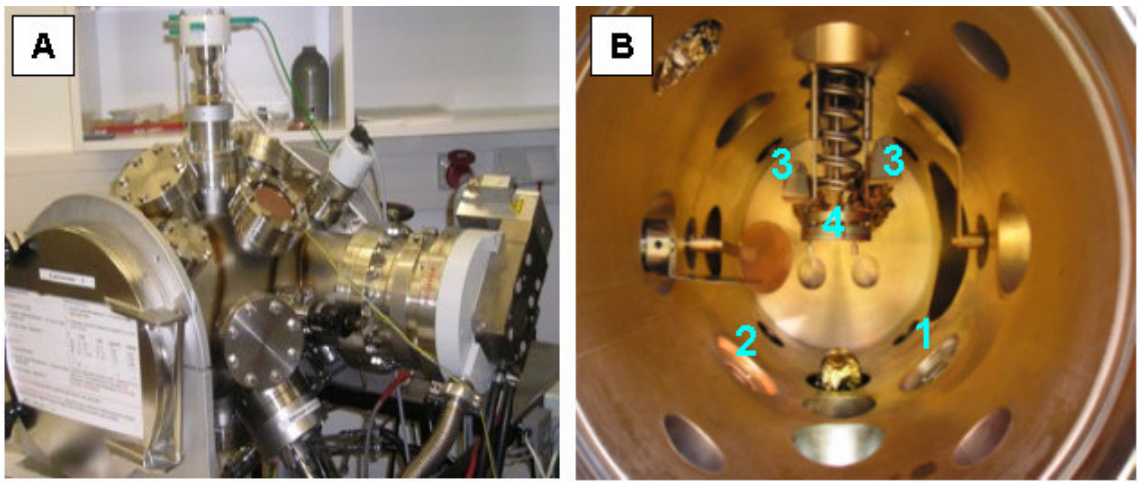

Figure 1: Photographs of the stainless steel vacuum chamber used in this thesis work: A) Vacuum chamber for sputtering and evaporation. B) the inside part of the chamber, view through the large load lock door: (1) pt magnetron (2) Copper magnetron (3) quartz monitors (4) sample holder.

5.1.1 Evaporation

In the evaporation process the material to be deposited is heated in high vacuum ~ 10^{-8} mbar to vaporize the species which subsequently condenses on the wafer surface. At such low pressures, the mean free path of the evaporated species is long enough to allow it to condense on the wafer surface without a high collision probability with the residual gas molecules. The evaporation rate is determined by the pressure, type of the evaporated material (atomic mass) and temperature. The rate is given by:

$$\phi = 3.513\times10^{22}\frac{P_e}{\sqrt{MT}} \tag{5.1}$$

There are two kinds of evaporation namely free evaporation and effusion. The former is isotropic where the latter is directional. Effusion is used for Chrome deposition.

As this evaporation process is inherently directional, films are deposited with poor step coverage, which is one of the major reasons for the increased interest behind using sputtering for depositing wire materials.

5.1.2 Sputtering

Sputtering is the term used to describe the mechanism in which atoms of the target are dislodged its surface by collisions with high energy particles (280). The technique has become a widely used deposition technique for many groups of materials.

In general, sputtering process consists of four steps:

1) Ions are generated and directed at a target

2) The ions sputter target atoms;

3) The ejected atoms are transported to the substrate.

4) The sputtered atoms condense and form a thin film.

This technique has replaced evaporation in many fields because of the following advantages:

1) Sputtering results in a uniform thickness of the deposited film over large substrates from large area targets.

2) Film thickness control is relatively easily achieved by selecting a constant set of operating conditions.

3) Film properties such as step coverage and grain structure can be controlled by varying the negative bias and heat applied to the substrate. On the other hand stress and adhesion can be controlled by altering process conditions such as power and pressure.

4) It is possible to use a single target for a number of deposition runs before target replacement is necessary.

However, sputtering has its own limitations, in case of film purity due to the low-medium vacuum range of use; low deposition rate of some materials, and; low stability of some materials facing high energy ionic bombardment.

5.1.2.1 Principles of Sputtering

In the sputtering technique the energetic particles may be ions, neutral atoms, neutrons, electrons or photons. However, the most relevant sputtering applications are performed under the bombardment of ions (281). When a solid surface is bombarded by atoms, ions, or molecules many phenomena can occur. The kinetic energy of the impinging particle is the most influential parameter to determine which events are most likely to take place. For low energies (< 10 eV), most interactions occur only at the surface of the target material. At very low energies (< 5 eV) such events are likely to be limited to reflection or physisorption of the bombarding species. For low energy which exceeds the binding

energy of the target material (5-10eV), surface migration and surface damage effects can take place. At much higher energies (> 10keV), the impinging particles are most likely to be embedded in the target, and this mechanism is the basis of ion-implantation. At energies between the two extremes (5-10keV), two other effects also arise: 1) some fraction of the energy of the impinging ions is transferred to the solid in the form of heat, and structural damage; and 2) another fraction of such energy causes atoms from the surface to be dislodged and ejected into the gas phase (sputtering).

As illustrated in Figure 2, the sputtering process takes place in an evacuated chamber. Argon is introduced into and ionized in the chamber which contains the substrate and the target of the material to be sputtered. The target is maintained at a negative potential relative to the positively charged argon atoms. The positive ion accelerates towards the negative charge, hitting the target with sufficient energy to remove material. Typically the argon atom are not embedded in the target. Sputtered atoms ejected into the gas phase are not in their thermodynamic equilibrium state, and tend to deposit on everything in the chamber, including the substrates.

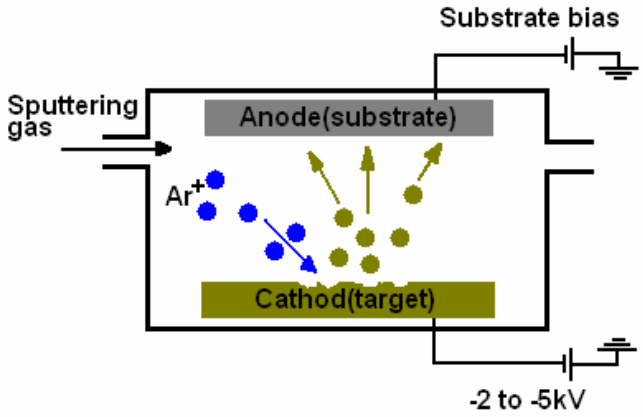

Figure 2: sketch illustrates the principles of sputtering.

Sputtering processes are divided into four categories: namely, DC, AC(mainly RF), reactive, and magnetron. Here, the discussion will be restricted to magnetron sputtering which is used in this work for the deposition of the wire material by fracture approach.

5.1.2.2 Magnetron Sputtering

In sputtering, not all of the electrons escaping the target contribute to the ionized plasma glow area. The wasted electrons fly around the chamber causing a number of problems. A magnetron sputtering source addresses the electron problem by placing magnets behind, and sometimes, at the sides of the target. The crosswise magnetic field is established by a ring of bar magnets plus one central one, and these are connected on the back by iron “field return” plate to complete the magnetic circuit and to confine the field as shown in Figure 3. Electrons emitted from the target surface or created by the ionization in the

sheath field are accelerated vertically by the electric field but, at the same time, forced sideways by the magnetic field hence the net motion is a clockwise drift around the circle of the target. This increases the path length in the plasma and increases the probability of collisions with the background gas. Since the impact efficiency of the available electrons with the working gas is increased, it is then possible to sputter at lower pressures than those used for either DC or RF diode sputtering. However, it is possible to deposit a film with high rate of deposition due to the higher ionization and plasma densities.

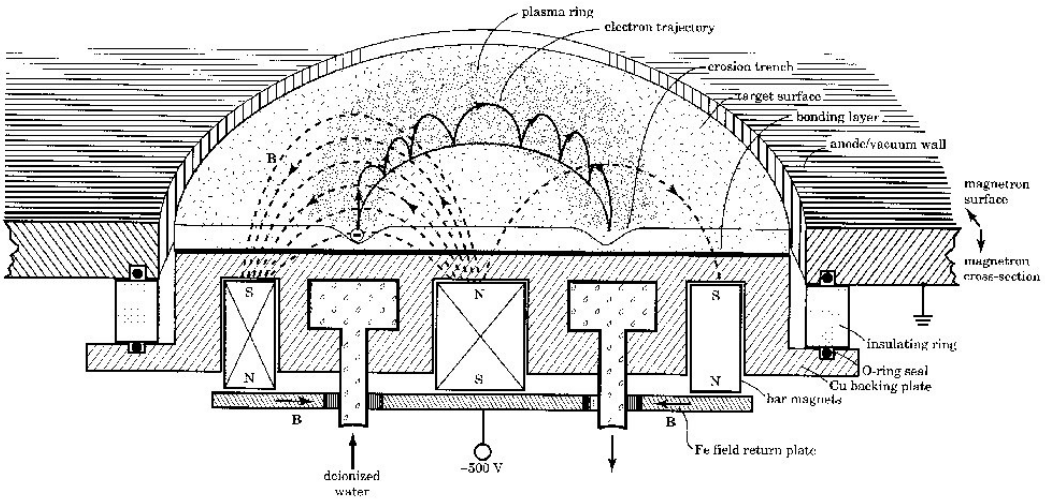

Figure 3: Magnetron Sputtering (figure D. L. Smith: Thin-Film Deposition: Principles and Practice)

The resulting film properties can be controlled by adjusting the following parameters:

a) Sputter current: It mainly determines the rate of the deposition processes and hence the time which remains for arriving particles during the growth process for either surface diffusion and agglomeration on existing growth centers or nucleation with other adatoms.

b) Applied voltage: It determines the maximum energy, with which sputtered particles can escape from the target (reduced by the binding energy) Energies of the sputtered particles show a broad distribution with a maximum between 1 eV and 10 eV. The applied voltage also determines the sputter rate, which is the number of sputtered particles per impinging ion.

c) Pressure in the sputter chamber: It determines the mean free path (λ) for the sputtered material, which is inversely proportional to the pressure. Together with the target-substrate distance (TS) the pressure controls, how many collisions occur for particles on their way from the target to the substrate.

d) The substrate temperature: It can have a strong impact on the growth behaviour with respect to crystallinity or density of the samples. It can be adjusted to room temperature or higher temperatures. However, even during sputtering without external heating the substrate temperature may rise

considerably, especially during long sputtering times for the deposition of thick films. Usually substrate and target surfaces are parallel to each other.

e) Deposition angle: sputtering under oblique incidence is achieved by tilting the substrate or the target. In that way a new preferential direction for the film growth and potentially anisotropic films can be produced.

F) Film thickness and reading calibration: during the deposition processes a convential STM-100/MF quartz microbalance monitoring system was used. The STM-100/MF uses the resonant frequency of an exposed quartz crystal to sense the mass of deposited films attached to its surface. Calibration is affected by three different parameters, material Z-Factor, material density, and tooling factor. Density and Z-Factor are material factors where tooling is a deposition system geometry correction which consideres the location of sensor relative to the substrate.

In principle, the Z-Factor can be calculated by the following formula:

$$\text{Z - Factor} = \left[\frac{D_q . U_q}{\frac{D_f}{U_f}} \right]^{1/2} \tag{5.2}$$

Where: D_q is density of quartz , U_q is shear modulus of quartz, D_f is density of the film and U_f: is the shear Modulus of the film. Film Z-Factor values are typically very close to the bulk Z-factor values. High stress materials seem to have values slightly lower than expected. For a more exact solution a calibration is carried out like in the density method. However use of the material bulk density value will normally provide sufficient film thickness accuracy. If additional accuracy is needed, the following procedure is used:

A new sensor crystal (this eliminates Z-Factor errors) is placed adjacent to the substrate so that both sensor and substrate see the same evaporant stream. The instrument density is set to the bulk value of the material. Z-factor is set to 1.000 and the tooling factor is set to 100 %. Approximately 5000 angstroms of material is deposited on the sensor and the substrate. The correct density value is determined by the formula:

$$\text{Density}\left(\frac{g}{cc}\right) = \frac{(\text{Density Parameter}).(\text{Reading})}{(\text{Measured thickness})} \tag{5.3}$$

The calculated value is checked by setting the instrument density parameter to the calculated value and making sure that the thickness display shows the corrected reading. The correct tooling factor value can be determined by the following formula:

$$\text{Tooling } \% = 100 \times \frac{(\text{Substrate Thickness})}{\text{Displayed Thickness}} \tag{5.4}$$

5.2 Atomic Force Microscopy (AFM)

Scanning probe microscopes are of great importance in analyzing nanostructures. Figure 4 schematically shows the operation principle of the AFM. The high degree of spatial resolution is made possible by the small size of the cantilever and its close proximity to the surface. The cantilever is equipped with a tip which interacts with the sample surface. A laser beam reflects off the back of the cantilever, its deformations due to interaction forces can then be measured. The deflection of the laser spot incident on a photodetector divided into two parts indicates the deflection of the cantilever. Oscillation is stimulated using the deformation of a piezoelectric tube. The system can be operated in air, vacuum, or liquid.

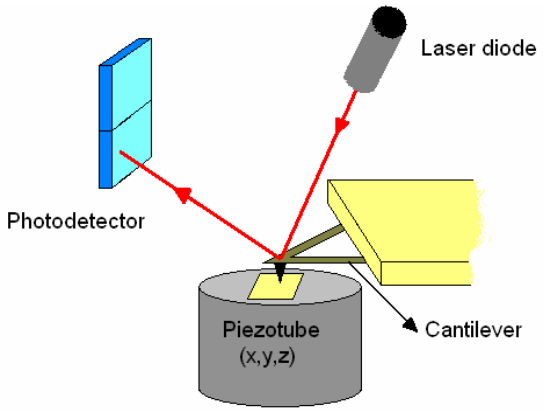

Figure 4: Sketch showing the operation principle of the AFM.

5.2.1 Probe-Sample Interactions

If two solids are in close proximity to each other several interactions resulting in a force of attraction or repulsion can result. The sensitivity of state-of-the-art force microscopes is sufficient to detect surface forces at the nanometer scale including intermolecular interactions. Figure 5 shows the typical variation of the interaction potential between probe and sample if their separation is successively decreased. At relatively large separations, typically of the order of 1 nm or more, van der Waals interactions lead to a negative interaction potential and thus to attractive forces. These forces are always present in any situation. Their origins are zero-point quantum fluctuations which strongly depend on the local probe-sample geometry, as well as on their respective materials, and finally on the medium between probe and sample.

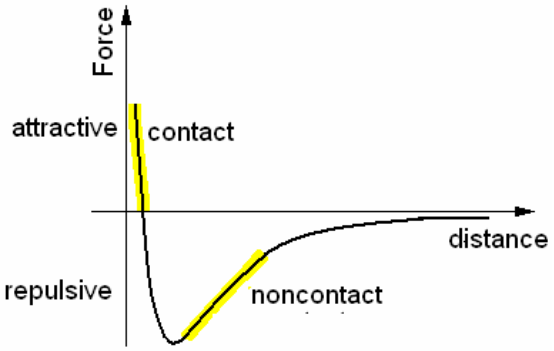

Figure 5: The typical variation of the interaction potential between probe and sample.

The van der Waals forces usually increase in magnitude if the probe approaches the sample surface. Often the resulting force-distance curve can be characterized by a simple reciprocal power. If the outermost atom of the probe starts to penetrate the sample surface, i. e. the electronic wave functions of probe and sample start to overlap, short-range repulsive forces are introduced. Since the valence- and conduction-band electrons are typically 1-10 Å away from the outermost atomic nuclei of the sample, while the extent of the inner bound electrons is 10-30 pm, the resulting repulsion is indeed very limited in range. When reducing the distance further more and more interatomic interactions lead to a continuously increasing repulsion, while the overall long-range probe-sample interaction is still attractive. Thus the net interaction potential exhibits first a point of inflection, then an absolute minimum, followed by a situation where the repulsive short-range interactions just balance the attractive long-range interactions, and finally a regime where ultimately the repulsive interactions dominate the attractive ones. In the last described regime the probe penetrates the sample, leading to elastic and then inelastic deformations. Under normal ambient conditions the sample surfaces are frequently covered by a thin layer of adsorbed water. The same holds of course for the cantilever probes. The presence of liquid thin films or even only of a sufficiently high humidity manifests itself in the formation of a liquid capillary between probe and sample. The meniscus causes huge attractive interactions usually dominating all interactions of interest mentioned above. The problem is not only that capillaries cause large "background forces", a more serious consequence is that the overall loading force exerted by the probe on the sample is greatly increased. This limits the obtained lateral resolution in contact-mode and sometimes even leads to destruction of the sample surface. Additionally, liquid menisci are sources for pronounced hysteresis effects in the force curve.

5.2.2 Operation Modes

AFM can be operated either in the *contact mode* where repulsive columbic forces dominate or in *non-contact mode* where van der Waals forces dominate.

5.2.2.1 Contact Mode

Since the force microscope is equipped with a feedback loop, it is convenient to keep the actual cantilever deflection constant by suitably adapting the probe-sample separation continuously while scanning. Thus, the working distance is increased if the local force exerted on the cantilever becomes temporarily relatively high, and it is decreased if the force falls below a preselected value. The resulting mode is called the constant-force mode which is one of the most important modes in which a force microscope can be operated.

It is most instructive to discuss image formation in the contact mode with the help of Fig. 5. The feedback value for an operation in the constant-force or constant-height mode is chosen within the regime of overall repulsive interaction. This means the probe exerts a certain loading force on the sample surface. In order to keeps this loading force either locally absolutely constant or constant in average during scanning, the probe has to follow the atomic or nanoscale corrugation of the sample surface.

Typical loading forces are of the order of 10^{-8} - 10^{-7} N. It is important to mention that this force is experimentally determined and composed of a long-range attractive interaction between probe and sample and a short-range repulsive interaction between the outermost probe atoms and the sample surface. Note that, if the force is set to a value which represents a net repulsive interaction -N, the corresponding repulsive force exerted by atoms at the probe apex on the sample is much higher than the setpoint value.

Contact mode is not suitable for imaging either weakly bound or soft materials, because the tip can damage or move some surface features of the sample, hence resulting in images with lower resolution.

5.2.2.2 Non-contact Mode

Non-contact mode operation simply consists of lifting the probe up to a certain distance from the sample to measure the long range interaction in as a static force. However, this is a seldom exception. Non-contact force microscopy usually involves a sinusoidal excitation of the cantilever with a frequency close to its main resonant frequency. The non-contact mode of operation involving an oscillating cantilever is frequently also called the *dynamic* or *AC mode*. Here, the resonant frequency or the amplitude of the vibrating cantilever is continuously monitored by the system and kept constant through the feedback circuit. The scanner motion at each probe location is used to create the topographic data set. The amplitude image is created from changes in the amplitude at each probe location, while phase data is obtained from the phase lag between the AC driven input and the cantilever oscillation output at each probe location.

The cantilever is usually driven into oscillation in one of the following methods: Either by using the acoustic mode where a piezoelectric transducer, which produces high frequency acoustic vibrations, is

attached to the cantilever holder as shown in Figure 6, or by using the magnetic mode where an AC magnetic field is applied to a cantilever that is coated with a magnetic material.

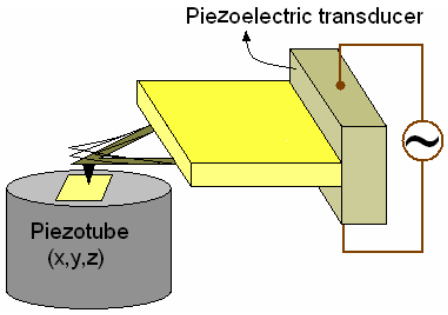

Figure 6: A sketch illustrating the acoustic mode for cantilever oscillation

5.2.3 AFM Resolution

The concept of resolution in AFM is different from radiation based microscopies because AFM imaging is a three dimensional imaging technique. The ability to distinguish two separate points on an image is the standard by which lateral resolution is usually defined. There is clearly an important distinction between images resolved by wave optics and scanning probe techniques. The former is limited by diffraction, the latter primarily by apical probe geometry as well as sample geometry.

One of the most important factors influencing the resolution which may be achieved with an AFM is the sharpness of the scanning tip. The first tips used by the inventors of the AFM were made by gluing diamond onto pieces of aluminum foil. Commercially fabricated probes are now universally used. The best tips may have a radius of curvature of only around 5 nm. The need for sharp tips is normally explained in terms of tip convolution. This term is often used to group together any influence which the tip has on the image, like broadening does.

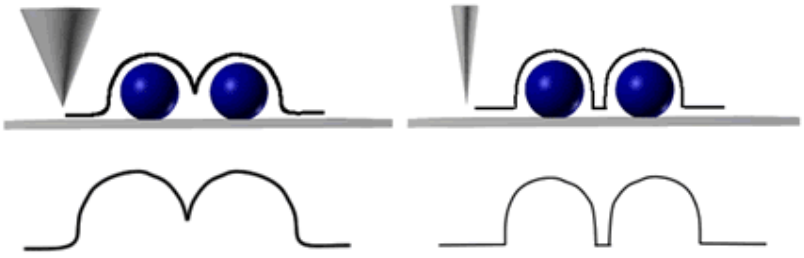

Figure 7: Broader tip with less resolution (left) and Sharp tip with better resolution.

Tip broadening becomes a problem when the radius of curvature of the tip is comparable with, or greater than, the size of the feature being imaged. Figure 7 illustrates this problem; as the tip scans over the specimen, the sides of the tip make contact before the apex, and the microscope begins to respond to

the feature. This is known as tip convolution. In general, the sharper the probe is, the higher the resolution of the AFM image can be.

5.3 Scanning Electron Microscopy (SEM)

The scanning electron microscope (SEM) is used for imaging surfaces of materials with the aid of signals derived from the interaction between probe electrons and a specimen. Every electron microscope must of course have a source of electrons, which is called its illumination system. The illuminating electrons are produced by the electron gun. The electron itself gun consists of three parts, the filament, the Wehnelt cylinder, and the anode. Alternative names for the filament are cathode or emitter. Basically there two categories of electron emitters are used in SEM. The first category is thermoionic emitters, and in most SEMs these are either tungsten filaments or crystals of Lanthanum hexaboride (LaB6). The second category is the field emission gun which uses a sharp tipped tungsten crystal.

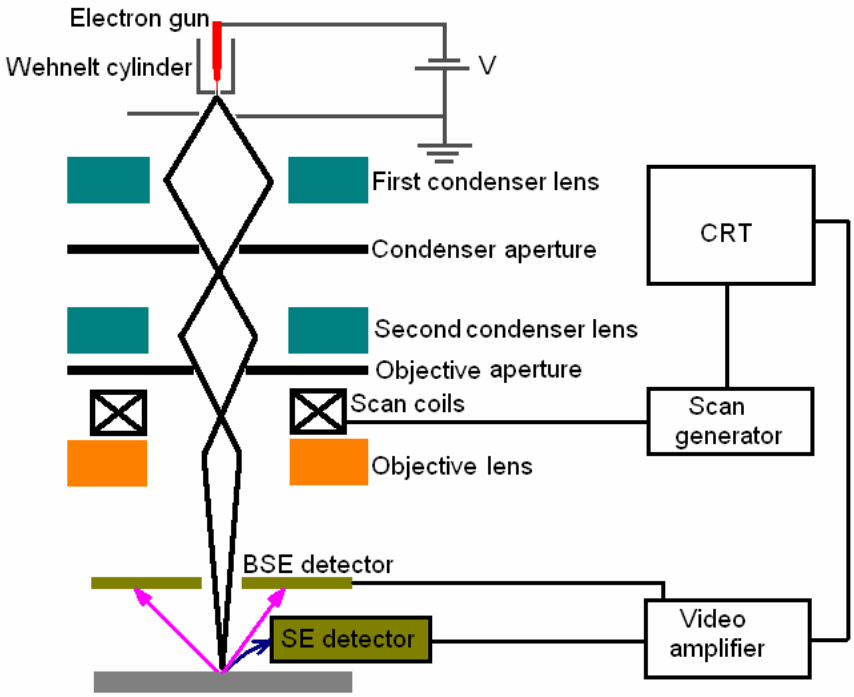

Figure 8: Sketch of a SEM

The emitted electrons are subsequently accelerated with a defined acceleration voltage between 1 kV to 30 kV and some times extends up to 60 kV. Fig. 1 shows a schematic of the scanning electron microscope and the path of the incident electron beam. Two or three condenser lenses in conjunction with a condenser aperture are used to condense and demagnify the electron source to a focused spot (probe) at the specimen surface, where it may have a diameter of as little as 2-10 nm. A set of scanning coils are used to scan the specimen moving the incident beam across it. The objective lens can focus the

scanning electron beam onto any desired place on the specimen. Due to the reaction of the specimen with the incident electron beam electrons are emitted from the specimen surfaceand then collected and counted by a detector. At the same time, the spot of cathode ray tube (CRT) is scanned across a display, while the brightness of the spot is modulated by the amplified current from the detector.

5.3.1 Electron – Specimen Interactions

A number of changes are induced by the interaction of the primary electrons with the atoms contained in a thick sample. Upon contacting the surface of the specimen most of the beam is not immediately bounced off in the way that light photons might be bounced off in a light dissecting microscope. Rather the energized electrons penetrate into the sample for some distance before they encounter an atomic particle with which they collide. In doing so the primary electron beam produces what is known as a region of primary excitation. Because of its shape this region is also known as the "tear-drop" zone or interaction volume (see Figure 9). A variety of signals are produced from this zone, and it is the size and shape of this zone that ultimately determines the maximum resolution of a given SEM working with a particular specimen. The various types of signals produced from the interaction of the primary beam with the specimen include secondary electrons, backscattered electrons, Auger electrons, characteristic X-rays, and cathodluminescence. Here, the first four signals will be discussed.

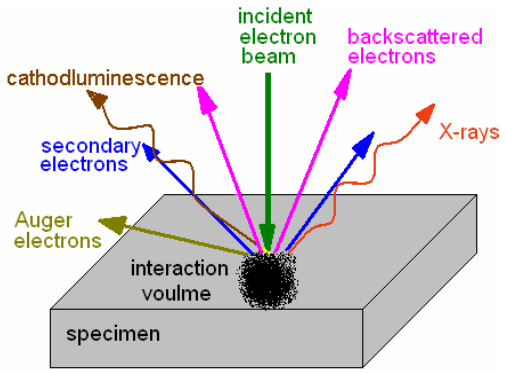

Fig 9: Sketch of Electron-Specimen interaction

5.3.1.1 Secondary Electrons (SE)

The most widely used signal produced by the interaction of the primary electron beam with the sample is the secondary electron emission signal. A secondary electron is produced when an electron from the primary beam collides with an electron from a specimen atom and transfers energy to it. This will help to ionize the atom and in order to re-establish the proper charge ratio. After the ionization event an electron may be emitted. Such electrons are referred to as "secondary" electrons. Secondary electrons themselves can produce several additional secondary electrons. Secondary electrons are different from other electrons as they have an energy of less than 50 eV. This is by far the most common type of image

mode used in modern SEMs. It is most useful when examining surface structure and gives the best resolution image of any of the scanning signals. Depending on the initial size of the primary beam and various other conditions (composition of sample, accelerating voltage, position of specimen relative to the detector) a secondary electron signal can resolve surface structures of 10 nm or smaller. Because secondary electrons are emitted from the specimen in an omni directional manner and possess relatively low energies they must be collected in some way before they are be counted by the secondary electron detector. For this reason the secondary electron detector is surrounded by a positively charged anode or Faraday cup or cage that has a potential change of about 200 V. That way many of the secondary electrons are drawn into the detector.

5.3.1.2 Backscattered Electrons (BSE)

A backscattered electron is defined as one which has undergone a single or multiple scattering events and escapes with an energy of more than 50 eV. Backscattered electrons are produced as the result of elastic collisions with the atoms of the sample and usually retain about 80% of their original energy. The number of backscattered electrons produced increases with increasing atomic number of the specimen. For this reason, a sample that is composed of two or more different elements which differ significantly in their atomic numbers will produce an image that shows a different contrast for the elements despite a uniform topology. Elements that are of a higher atomic number will produce more backscattered electrons and will therefore appear brighter than neighboring elements.

The region of the specimen from which backscattered electrons are produced is considerably larger than it is for secondary electrons. For this reason the resolution of a backscattered electron image is considerably less (1.0 μm) than it is for a secondary electron image (10 nm).

The detector for backscattered electrons is similar to that used in the detection of secondary electrons in that both utilize a scintillator and photomultiplier design. The backscatter however lacks a biased Faraday. Only those electrons that travel in a relatively straight path from the specimen to the detector are contributing to the backscattered image.

5.3.1.3 Characteristic X-rays

Another class of signals produced by the interaction of the primary electron beam with the specimen are characteristic X-rays. When an electron from an inner atomic shell is displaced by colliding with a primary electron, it leaves a vacancy in that electron shell. In order to re-establish the proper balance in its orbitals following an ionization event, an electron from an outer shell of the atom may "fall" into the inner shell and replace the spot vacated by the displaced electron. In doing so the falling electron loses energy and this energy is referred to as X-rays. These characteristic X-rays are usually employed for energy dispersive X-ray analysis.

5.3.1.4 Auger Electrons

Auger electrons are produced when an outer shell electron fills the hole vacated by an inner shell electron that is displaced by a primary or backscattered electron. The excess energy released by this process may be carried away by an Auger electron. Because the energy of these electrons is approximately equal to the difference between the two shells, like in the case of X-rays an Auger electron can be characteristic of the type of element from which it was released and the shell energy of that element. By discriminating between Auger electrons of various energies Auger Electron Spectroscopy (AES) can be performed and a chemical analysis of the specimen surface can be made. Because of their low energies, Auger electrons are emitted only from near the surface. They have an escape depth of between 0.5 nm to 2 nm making their potential spatial resolution especially good and nearly that of the primary beam diameter.

5.3.2 Energy-Dispersive X-ray Analysis (EDX)

EDX is one of the most useful features of SEM analysis. This analytical tool allows simultaneous non-destructive elemental analysis of a sample. If the various elements in the sample are stimulated to emit characteristic X-Rays then these elements may be identified by analysing the emitted radiation. The analysis is carried out by using energy dispersive solid state spectrometer where the signals are collected and sorted according to their energies by a multichannel analyzer, and then are displayed as a spectrum of the detected elements. EDX analysis can be used to perform specific elemental analysis along a certain line with a resolution power of 10 to 100 nm.

5.4 X-ray diffraction (XRD)

XRD has been long used to address all issues related to the crystal structure of solids, such as geometry and lattice constant, identification of unknown material, orientation of single crystals or poly crystals, etc. In this technique X-rays with a wavelength (λ) ranging from 0.7 to 2 Å illuminate a specimen and are diffracted according to the Bragg law:

$$\lambda = 2d \sin\theta \tag{5.5}$$

where d is the spacing between the atomic planes. The intensity of the diffracted X-rays is measured as a function of the diffraction angle 2θ and the specimen orientation. For individual nanoscale solids, diffraction is only of limited utility for both fundamental and practical reasons. The solid's small size interrupts the periodicity of the lattice, blurring diffraction peaks, and also produces a very small scattered signal. The Scherrer formula is mostly used to determine the crystallite size, D:

$$D = K\lambda / B\cos\theta \tag{5.6}$$

where K is Scherrer constant of the order of unity for usual crystal, and B is the full width of height maximum (FWHM). However, one should be in mind that nanoparticles often form twinned structures. Therefore, this formula may give results which are different from the true particles sizes.

5.5 Optical Microscopy

The light microscope is a deceptively simple instrument, being essentially an extension of our eyes. It allows us to magnify small objects, enabling us to see structures that are below the resolving power of human eye (0.1 mm).

Optical microscopy is used to study the fine structure and morphology of objects and images are produced through interaction of light with the objective and specimen. The magnification ranges from 2 x to 2000 x being limited by the nature of the specimen, the objective lens and the wavelength of light.

Resolution – The resolution is related to the numerical aperture of the objective lens and the wavelength passing through the lens. The higher the numerical aperture and the shorter the wavelength, the better the resolution. The numerical aperture of an optical system such as an objective lens is defined by:

$$NA = n \sin \theta \tag{5.7}$$

where n is the index of refraction of the medium in which the lens is working and θ is the half-angle of the maximum cone of light that can enter or exit the lens.

Contrast is related to the illumination system and can be adjusted by changing the intensity of light and the diaphragm/pinhole aperture. Also, chemical stains applied to the specimen can enhance contrast.

Optical light microscopy with magnifying capability from 50 x to 1000 x was used to analyse the structures in bright field as well as dark field.

In the bright field technique vertical illumination is used for the examination of the specimen and under these conditions normal surfaces appear bright, while inclined surfaces appear dark. In the dark field technique the light beam strikes the specimen obliquely so that no specularly reflected light enters the objective a good image quality can be obtained using an annular cone of rays focused in the object plane instead of tilting the illumination.

5.6 UV/VIS Spectroscopy

UV-VIS spectroscopy is useful to characterize the absorption, transmission, and reflectivity of a variety of technologically important materials, coatings, thin films and solutions. When white light passes through or is reflected by a colored substance, a characteristic portion of the mixed wavelengths is

absorbed. The remaining light will then be of the complementary color to the wavelength(s) absorbed. This relationship can be demonstrated by the color wheel shown in Figure 11a. Complementary colors are diametrically opposed to each other, thus, absorption of 420-430 nm light makes a substance appear yellow, and absorption of 500-520 nm light makes it appear red. The UV-VIS spectral range is approximately from 190 to 900 nm. In general specific regions of the electromagnetic spectrum are absorbed by exciting specific types of molecular and atomic motion to higher energy levels. Absorption of microwave radiation is generally due to excitation of molecular rotational motion. Infrared absorption is can be explained by vibrational motions of molecules. Absorption of visible and ultraviolet (UV) radiation is due to excitation of electrons, in both atoms and molecules, to higher energy states. All molecules will undergo electronic excitation following absorption of light.

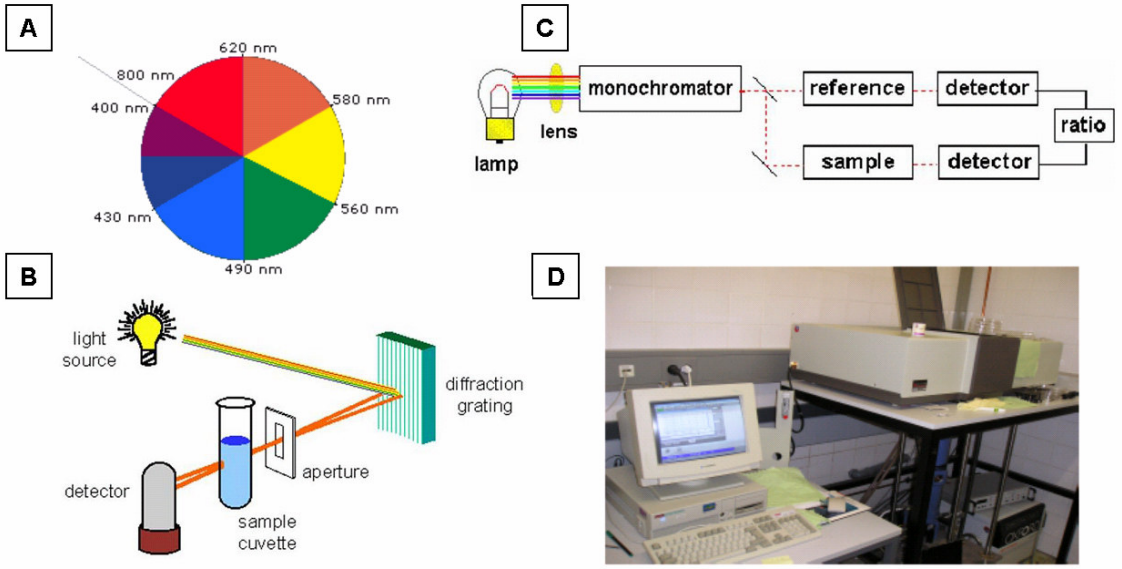

Figure 11: A) color wheel. B) Sketch of a single-beam UV/VIS spectrophotometer. C) Sketch of a dual-beam UV/VIS spectrophotometer. D) Image of the UV/VIS/NIR Spectrometer Lambda900 from Perkin Elmer

There are two types of spectrophotometers: single beam or double beam. In the single beam instrument, seen in Figure 11b, all of the light passes through the sample cell. This was the earliest design, but it is still use in both teaching and industrial labs. In a double-beam instrument, Figure 11c**,** the light is split into two beams before it reaches the sample. One beam is used as the reference; the other beam passes through the sample. Some double-beam instruments have two detectors (photodiodes), thus measuringthe sample and reference beam at the same time. The detector alternates between measuring the sample beam and the reference beam. Both techniques can be seen in fig 1b,c respectively. The instrument measures the intensity of light passing through a sample (I), and compares it to the intensity of light before it passes through the sample (Io). The ratio I / Io are called the transmittance, and are usually expressed as a percentage (%T). The absorbance, A, is based on the transmittance: A = –log (%T).

The UV/VIS Spectrometer, Lambda900 of PERKIN ELMER, was used to measure the plasmon resonance of metallic structures in the visible frequency response, using a single beam. Fig. 11d shows the Image of the facility of UV/VIS/NIR Spectroscopy Lambda 900 from Perkin Elmer. The light from a UV or visible light source passes through a series of slits and a diffraction grating to select only one wavelength. The beam then travels through a reference sample, usually made of glass, and then to a detector, which measures the amount of light that was not absorbed. The sample is then inserted, and the process repeated. Sample sizes that were measured are approximately 1cm by 1cm.

5.7 Spin Coating

Spin coating has been used for several decades for application of thin films. In principle, it consists of a high speed motor with a vacuum plate attached on the top. The spin coater used in this thesis is shown in Figure 12a. A typical process consists of depositing a drop/puddle of a fluid resin onto the center of a substrate and then spinning the substrate at high speed (typically around 3000 rpm) as shown in Figure 12b. Centrifugal acceleration will cause the material to spread to, and eventually off, the edge of the substrate leaving a thin film of resin on the surface. Final film thickness and other properties will depend on the nature of the resin (viscosity, drying rate, solids percent, surface tension, etc.) and the parameters chosen for the spin process itself.

Factors such as maximum rotational speed, acceleration, and fume exhaust play a role in determining the properties of coated films. One of the most important factors in spin coating is repeatability. Subtle variations in the parameters that define the spin process can result in drastic variations of the coated film. The two common methods of dispening are static and dynamic.

Static dispensing (which is used here) is simply deposition a small puddle of fluid on or near the center of the substrate. The volume of fluid can range from 1 to 10 cc depending on the viscosity of the fluid and the size of the substrate to be coated. High viscosity fluids or large substrates usually require a larger amount of fluid. Dynamic dispensing is the process of dispensing while the substrate is rotating at low speed. A speed of about 500 rpm is commonly used during this step of the process. This serves to spread the fluid over the substrate and can result in less waste since it is usually not necessary to deposit as much material as to wet the entire surface of the substrate. This is particularly advantageous method when the fluid or substrate itself has poor wettability and can eliminate voids that may otherwise form.

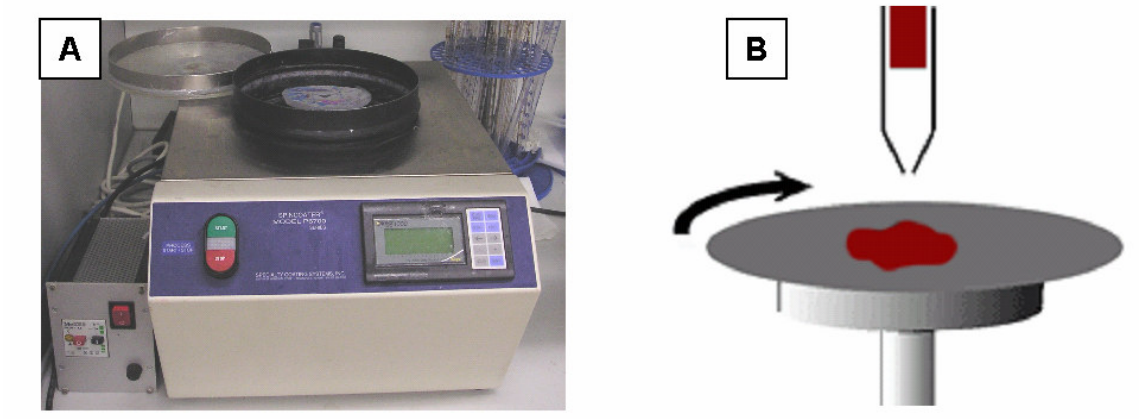

Figure 12: A) Image of the Spain coater B) Sketch of the operating principle

6 Appendix “Patents and Publications”

6.1 Patents

4. **M. Elbahri**, K. Hirmas, F. Faupel, R.Adelung.

   Ordered Pattern by a Controllable Dewtting around a Defect. (Patent is applied, 09.2007)

3. **M.Elbahri**, R. Adelung, DE 10 2006 038 703.1

   Verfahren zur Erzeugung von oxidischen Nanopartikeln aus einem Oxidpartikel bildenden Material.

   International Patent: PCT/DE2007/001444

2. **M. Elbahri**, R. Adelung, D. Paretkar, DE 10 2005 060 407 B3.

   Verfahren zur Herstellung von Nanostrukturen auf einem Substrat.

   International Patent: PCT/DE2006/002066

1. R. Adelung, **M. Elbahri**, S. Jebril, S. Rehders, DE 10 2005 056 879 A1.

   Verfahren zur Erzeugung einer Mehrzahl regelmäßig angeordneter Nanoverbindungen auf einem Substrat.

   International Patent: PCT/DE2006/002068

6.2 Publications

8. V. S. K. Chakravadhanula, **M. Elbahri**, U. Schürmann, H. Greve, H. Takele, V. Zaporojtchenko, and F. Faupel: Equal Intensity Double Plasmon Resonance (EIDPR) of bimetallic quasina nocomposites based on sandwich geometry.

   (Submitted).

7. **M. Elbahri**, D. Paretkar, K. Hirmas, S. Jebril, R. Adelung: Anti-Lotus Effect for Nanostructuring at the Leidenfrost Temperature.

   Advanced Materials, 19, 1262 (2007).

   *a) Inside front cover story of **Advanced Materials** Volume 19, Issue 9, (2007).*

   *b) Discussed by Colin Bain in **Nature Nanotechnology**, News and Views, "Drip painting on a hot canvas" 2, 344 (2007).*

6. **M. Elbahri**, S. K. Rudra, S. Wille, S. Jebril, M. Scharnberg, D. Paretkar, R. Kunz, H. Rui, A. Biswas, R. Adelung: Employing Thin-Film Delamination for the Formation of Shadow Masks for Nanostructure Fabrication.

   Advanced Materials, 18, 1059 (2006).

5. H. Eilers, A. Biswas, T.D. Pounds, M. Grant Norton and **M. Elbahri**: Teflon AF/Ag nanocomposites with tailored optical properties.

   Rapid communication, J. Mater. Res.,21, 2168, (2006).

4. **M. Elbahri**, S. Jebril, S.K. Raudra, D. Chenger, V. Cimalla, O. Ambacher, D. Paretkar, S. Wille, R.Adelung: New approach for nanowires fabrication for integration in sensor applications.

   Nanofair, 1920, ISBN 3-18-091920-5 (2005).

3. R. Adelung, **M. Elbahri**, S. K. Rudra, A. Biswas, S. Jebril, R. Kunz, S. Wille, Michael Scharnberg: Employing thin film failure mechanisms to form templates for nano-electronics.

   MRS Proc. 875 O11.3/B7.3 (2005).

2. A. Biswas, R. Kunz, **M. Elbahri**, R. Adelung, O. C. Aktas, U. Saeed, U. Schürmann, H. Takele, V. Zaporojtchenko, F. Faupel and T. Strunskus: Arrays of wirelike microstructures of Ag with visible wavelength transparent plasmonic response at near-ultraviolet and midinfrared regions.

   Appl. Phys. Lett. 85, 1952 (2004).

1. R. Adelung, O.C. Aktas, J. Franc, A. Biswas, R. Kunz, **M. Elbahri**, J. Kanzow, U. Schürmann, and F. Faupel: Strain controlled growth of nanowires within thin film cracks.

   NATURE MATERIALS, 3, 375 (2004).

7 Appendix "References"

[1] J. Giles, Nature, 441, 265 (2006).

[2] J. Y. Cheng, A. M. Mayes, C. A. Ross, Nature Materials, 3, 823 (2004).

[3] B. D. Gates, Q. Xu, J. C. Love, D. B. Wolfe, G. M. Whitesides, Annu. Rev. Mater. Res. 34, 339 (2004).

[4] Z. Tang and N. A. Kotov, Adv. Mater, 17,951 (2005).

[5] C. P. Poole, Jr., F. J. Owens, Introduction to Nanotechnology, Wiley-VCH, Weinheim, Germany (2003).

[6] G. M. Whitesides, B. Grzybowski, Science, 295, 630 (2002).

[7] E.L. Thomas, Science 286,1307 (1999).

[8] J-W. Park and E.L. Thomas, Polym. Prepr., 43, 360 (2002).

[9] J.D. Hartgerink et al., Science, 294, 1684 (2001).

[10] M.D. Hollingsworth, Science, 295, 2410 (2002).

[11] M.N. Jones and D. Chapman, Micelles, Monolayers and Biomembranes (Wiley-Liss, New York, 1995).

[12] O. Fruchart, C. R. Physique 6 (2005). " Special Issue on self-organization on surfaces"

[13] a)Y. Sun and Y. Xia. Scince,298, 2176 (2002).

b) Z.L. Zhang Nano Lett. 3, 1341 (2003)

c) D.H. Gracias.et al. Science,289, 1170 (2000)

[14] a) C. B. Murray, et al., MRS Bull. 2001, 26, 985.

b) M.-P. Pileni, Adv. Funct. Mater. 2001, 11, 323.

c)W. P. Halperin, Rev. Mod. Phys. 1996, 58, 533;

d)L. N. Lewis, Chem. Rev. 1993, 93, 2693.

e) G. Schön and U. Simon, Colloid Polym. Sci. 1995, 273, 101.

f) R. D. Theys, G. Sosnovsky, Chem. Rev. 1997, 97, 83.

[15] N. A. Kotov, F. C. Meldrum, C. Wu, J. H. Fendler, J. Phys. Chem., 98, 2735 (1994).

[16] N. A. Kotov, Mutilayer Thin Films (Eds: G. Decher, J. B. Schlenoff), Wiley-VCH, Weinheim, Germany (2003)

[17] C. P. Collier, T. Vossmeyer, J. R. Heath, Annu. Rev. Phys. Chem., 49, 371 (1998).

[18] C. B. Murray, C. R. Kagan, M. G. Bawendi, Annu. Rev. Mater. Sci., 30, 545 (2000).

[19] O. Harnack, C. Pacholski, H. Weller, A. Yasuda, J. M. Wessels, Nano Lett., 3, 1097 (2003).

[20] J. C. Love, A. R. Urbach, M. G. Prentiss, G. M. Whitesides, J. Am. Chem. Soc., 125, 12696 (2003).

[21] D. Gourdon, M. Yasa, A. Alig, Y. Li, C. Safinya, J. Israelachvili, Adv. Funct. Mater., 14, 238 (2004).

[22] T. Bigioni, X. Lin, T. Nguyen, E. Corwin, T. Witten and H. Jaeger, Nature Materials 5, 265 (2006).

[23] R. S. Wagner, W. C. Ellis, Appl. Phys. Lett., 4, 89 (1964).

[24] H. Fan, P. Werner, M. Zacharias, Small, 2,700 (2006).

[25] L. Vayssieres, Ph.D. Thesis, Université Pierre et Marie Curie, Paris (1995).

[26] M. Law, J. Goldberger, and P. Yang, Annual Review of Materials Research., 34, 83 (2004).

[27] Y. Wang, T. Herricks, Y. Xia, Nano Lett., 3, 1163 (2003).

[28] R. Duggal, F. Hussain, M. Pasquali, Adv. Mater., 18, 29 (2006).

[29] M. Elbahri, D. Paretkar, K. Hirmas, S. Jebril, R. Adelung. Adv. Mater., 19, 1262 (2007).

[30] A. Kumar, M. Pattarkine, M. Bhadbhade, A. B. Mandale, K. N. Ganesh, S. S. Datar, C. V. Dharmadhikari, M. Sastry, Adv. Mater., 13, 341(2001).

[31] O. Harnack, W. E. Ford, A. Yasuda, J. M. Wessels, Nano Lett., 2, 919 (2002).

[32] E. Braun, Y. Eichen, U. Sivan, G. Ben Yoseph, Nature, 391, 775 (1998).

[33] K. Keren, M. Krueger, R. Gilad, G. Ben Yoseph, U. Sivan, E. Braun, Science, 297, 72 (2002).

[34] W. E. Ford, O. Harnack, A. Yasuda, J. M. Wessels, Adv. Mater., 13, 1793 (2001).

[35] J. Richter, R. Seidel, R. Kirsch, M. Mertig, W. Pompe, J. Plaschke, H. Schackert, Adv. Mater.,12, 507 (2000).

[36] E. Gazit, FEBS J., 274, 317, (2007).

[37] S. Minko, A. Kiriy, G. Gorodyska, M. Stamm, J. Am. Chem. Soc., 124, 10 192 (2002).

[38] A. Greiner, M. Steinhart, j. H. Wendorff, Nachrichten aus der Chemie, 2, 426 (2004).

[39] R. Dersch, M. Steinhart, U. Boudriot, A. Greiner and J.H. Wendorff, Polym. Adv. Technol. 16, 276 (2005).

[40] I. S. Chronakis, Journal of Materials Processing, 167, 283, (2005).

[41] C. R. Martin, Chem. Mater., 8, 1739 (1996).

[42] H. Ringsdorf, B. Schlarb, J. Venzmer, Angew. Chem. Int. Ed., 27, 113 (1988).

[43] M. A. El-Sayed, Acc. Chem. Res., 34, 257 (2001).

[44] F. Kim, J. Song, P. Yang, J. Am. Chem. Soc., 124, 14 316 (2002).

[41] L. Nagle, D. Ryan, S. Cobbe, D. Fitzmaurice, Nano Lett.,3, 51 (2003).

[42] L. Nagle, D. Fitzmaurice, Adv. Mater., 15, 933 (2003).

[47] E. Olson, G.C. Spalding, A.M. Goldman, M.J. Rooks, Appl. Phys. Lett., 65, 2740 (1994).

[48] M. Walther, E. Kaplon, J. Christen, D.M. Hwang, R. Bhat, Appl. Phys. Lett., 60, 521(1992).

[49] R. M. Penner, J. Phys. Chem. B, 106, 3339 (2002).

[50] R. Adelung, O. Cenk Aktas, J. Franc, A. Biswas, R. Kunz, M. Elbahri, J. Kanzow, U. Schürmann, F. Faupel. Nature Materials 3, 375, (2004).

[51] M. Elbahri, S. K. Rudra, S. Wille, S. Jebril, M. Scharnberg, D. Paretkar, R. Kunz, H. Rui, A. Biswas, R. Adelung, Adv.Mater., 18,1059, (2006).

[52] B. E. Alcala, H. Sehitoglu, T. A. Saif, Appl. Phys. Lett., 84,4669 (2004).

[53] The international roadmap for semiconductors, Edition 2006, excutive summary, Internet document: http://www.itrs.net/Links/2006.

[54] M. Switkes, R. R. Kunz, M. Rothschild, R. F. Sinta, M. Yeung, S. Y. J. Baek, Vac. Sci. Technol. B 21, 2794, (2003).

[55] S. Owa, H. Nagasaka, Y. Ishii, O. Hirakawa, T. Yamamoto,; Solid State Technol., 47, 43. (2004).

[56] J. H. Burnett, S. G. Kaplan, J. Microlith. Microfab. Microsys., 3, 68 (2004).

[57] A. M. Goethals, P. D. Bisschop, J. Hermans, R. Jonckheere, F. Van Roey, D.Van den Heuvel, A. Eliat, K. Ronse, J.Photopolym. Sci. Technol., 16, 549 (2003).

[58] J. Mulkens, J. McClay, B. Tirri, Brunotte, M. Mecking, B. H. Jasper, Proc. SPIE-Int. Soc. Opt. Micro., 5040, 753 (2003).

[59] F. Cerrina, S. Bollepalli, M. Khan, H. Solak, W. Li, D. He, Microelectron. Eng., 53, 13 (2000).

[60] R. L. Brainard, J. Cobb, C. A. J. Cutler, Photopolym. Sci.Technol. 16, 401(2003).

[61] V. N. Golovkina, P. F. Nealey, F. Cerrina, J. W. Taylor, H. H. Solak, C. J. J. David, Gobrecht. Vac. Sci. Technol. B, 22, 99 (2004).

[62] A. A. Talin, G. F. Cardinale, T. I. Wallow, P. Dentinger, S. Pathak, D. Chinn, D. R. J. Folk, Vac. Sci. Technol. B, 22, 781(2004).

[63] J. I. Larruquert, R. A. M. Keski-Kuha, Appl. Opt., 41, 5398 (2002).

[64] Li, Y.; Ota, K.; Murakami, K. J. Vac. Sci. Technol. B, 21,127 (2003).

[65] H. G. Craighead and P. M. Mankiewich, J. Appl. Phys, 53, 7186, (1982).

[66] R. F. W. Pease, J. Vac. Sci. Technol. B,10, 278, (1992).

[67] H. I. Smith and M. L. Schattenburg, IBM J. Res, 37, 319, (1993).

[68 D. M. Eigler and E. K. Schweizer, Nature, 344, 524, (1990).

[69] J. A. Stroscio and D. M. Eigler, Science, 254, 1319, (1991).

[70] Y. Xia, J. A. Rogers, K. E. Paul, G. M. Whitesides, Chem. Rev. 1999, 99, 1823.

[71] Y. Xia, G. M. Whitesides, Angew. Chem., Int. Ed. Engl., 37, 550 (1998).

[72] H. J. Ito, Polym. Sci., Part A: Polym. Chem., 41, 3863 (2003).

[73] Y. Xia, G. M. Whitesides, Annu. Rev. Mater. Sci. 28, 153 (1998).

[74] A. Kumar, G. M. Whitesides, Appl. Phys. Lett. 1993, 63 (2002).

[75] S. Y. Chou, P. R. Krauss, P. J. Renstrom, Science, 272, 85 (1996).

[76] H.Schulz, M.Wissen, H. C. Scheer, Microelectron. Eng. 67, 657 (2003).

[77] M. Farhoud, et.al. J. Vac. Sci. Technol. B, 17, 3182, (1999).

[78] J. Rybczynski, et.al, Nano Lett. 4, 2037.(2004).

[79] M. D. Thouless, IBM J. Res. Develop., 38, 367, (1994).

[80] Z. Suo, Encyclopedia of Materials Science and Technology, 2nd ed. (Eds: K. H. J. Buschow, R. W. Cahn, M. C. Flemings, B. Ilschner, E. J. Kramer, S. Mahajan), Elsevier, Oxford, UK (2001).

[81] J. Liang, R. Huang, J.H. Prevost , Z. Suo, International Journal of Solids and Structures 40, 2343((2003).

[82] A. A. Griffith, in „The phenomena of rupture and flow of solids“ Phil. Trans. Roy. Soc., A221, 163 (1920).

[83] G. I. Barenblatt, Adv. Appl. Mech. 7,55 (1962).

[84] M. Elbahri, Diplomarbeit, TU-Clausthal, (2003).

[85] R. S. YEO, C. H. CHENG, Journal of Applied Polymer Science, 32, 5733 (2003).

[86] E. J. Kramer in “ Developments in Polymer fracture” , Edited by E. H. Andrews, Applied Science Publisher, London (1979).

[87] R. P. Kambour, in “ Encyclopedia of Polymer Science and Engineering” , Wiely, New York (1986).

[88] T. A. Osswald and G. Menges: Material Science of Polymers for Engineers, Hanser, Munich (1995).

[89] G. Strobl: The Physics of Polymers, 2nd Edition, Springer, Berlin (1997).

[90] M. j. Doyle, J. Polym. Sci., Polym. Phys. Ed. 13, 2429 (1975).

[91] G. W.Ehrenstein: Polymer-Werkstoffe, Carl Hanser Verlag München Wien,(1999).

[92] M. Barber , J. Donley and J. S. Langer, Phys. Rev. A 40 366 (1989).

[93] B. N. J. Persson and E. Brener Phys. Rev. E. 71 036123 (2005).

[94] H. R. BROWN, Macromolecules. 24, 2752 (1991).

[95] L.O. FAGER and J.L. BASSANI, J. Eng. Mater. Technol. 115, 252 (1993).

[96] S.Y. HOBBS and R.C. BOPP, Polymer, 21, 559 (1980).

[97] H.R. BROWN, J. Mater. Sci. 16, 2329 (1981).

[98] Polymer Fracture: edited by H. H. Kausch, 2nd ed. (Springer-Verlag, New York, 1987).

[99] R. Schirrer and C. Goett, J. Mater. Sci. 16, 2566 (1981).

[100] R. P. Kambour, A. S. Holik, and S. Miller, J. Polym. Sci., Polym. Phys. Ed. 16, 91 (1978).

[101] G. J. Lake and A. G. Thomas, Proc. Roy. Soc. (Lond.), A300, 108 (1967).

[102] Commercial inkjet transparency film, Canson, Annonay, France

[103] Positiv 20, Kontakt Chemie, CRC Industries Deutschland GMBH

[104] J. Brandrup, E.H. Immergut, E.A. Gurlke: Polymer Handbook, IV Edition, John Wiley and Sons, New york, (1999).

[105] H.G. Elias, “Introduction to Polymer Science”, VCH, Weinheim, (1997).

[106] J. Liang, R. Huang, J.H. Pr evost, Z. Suo, International Journal of Solids and Structures, 40, 2343, (2003).

[107] K. A. Shorlin, J. R. de Bruyn, M. Graham, and S. W. Morris, Phys. Rev. E. 61,6950 (2000).

[108] S. Bohn, L. Pauchard, and Y. Couder, Phys. Rev. E. 71, 046214 (2005).

[109] S. Mani and T. M. Saif, App.Phys.Lett. 86, 201903 (2005).

[110] A. Salomon, D. Cahen, S. Lindsay, J. Tomfohr, V. B. Engelkes, and C. D. Frisbie, Adv. Mat. 15, 1881 (2003).

[111] J. Kirk, J. Mater. Chem., 14, 585 (2004).

[112] L. Carrette, K. A. Friedrich and U. Stimming, Fuel Cells, 1, 1 (2001).

[113] R.O'Hayre, S.J. Lee, S.W. Cha, and F. B. Prinz, J. of Power Sources, 109, 483 (2002).

[114] R. Adelung, M. Elbahri, J. Franc, O. C. Aktas, R. Kunz and F. Faupel, 7th International Conference on Nanostructured Materials, June 20, Wiesbaden/Germany (2004).

[115] R. F. Cook, Z. Suo, MRS Buletinl, 27, 45 (2002).

[116] B. Wui, A. Heidelberg, J. j. Boland, nature materials, 4, 525 (2005).

[117] R. F. Cook and Z. Suo, MRS Bulletin, 27, 45 (2002).

[118] M. M. Deshmukh, D. C. Ralph, M. Thomas, and J. Silcox, Appl. Phys. Lett. 75, 1631 (1999).

[119] B. Audoly, B. Roman, and A. Pocheau, Eur. Phys. J. B. 27, 7 (2002).

[120] S. jebril, Ph.D student.

[121] G. M. Whitesides, B. Grzybowski, Science, 295, 2418 (2002).

[122] N. D. Denkov, O. D. Velev, P. A. Kralchevsky, I. B. Ivanov, H. Yoshimura, K. Nagayama,Langmuir, 8, 3183 (1992).

[123] R. D. Deegan, O. Bakajin, T. F. Dupont, G. Huber, S. R. Nagel, T. A. Witten, Nature, 389, 827 (1997).

[124] R. D. Deegan, O. Bakajin, T. F. Dupont, G. Huber, S. R. Nagel, T. A. Witten. Phys. Rev. E, 62, 756(2000).

[125] R. D. Deegan, Phys. Rev. E, 61, 475 (2000).

[126] V. Kurikka, P. Shafi, I. Felner, Y. Mastai, A. Gedanken, A. J. Phys. Chem., 103, 3358 (1999).

[127] P. C. Ohara, W. M. Gelbart, Langmuir, 14, 3418 (1998).

[128] S. L. Tripp, S. V. Pusztay, A. E. Ribbe, A. Wei, J. Am. Chem. Soc., 124, 7914 (2002).

[129] J. Xu, J. Xia, and Z. lin, Angew. Chem, 119, 1892 (2007) and reference therein

[130] S. Nukiyama 1934 J. Soc. Mech. Eng. Japan 31 361 (in Japanese) (Engl. transl. S G Brickley 1960 AERE Trans. No 854)

[131] Z. Tamura, Y. Tanasawa, In 7th Symp. (Int.) on Combustion London: Butterworths Scientific Publications. 509-522 (1959).

[132] K. Christmann, Surface physical chemistry, Steinkopf, Darmstadt, (1991)

[133] Gottfried, B. S., Lee, C. J. & Bell, K. J. 1966 The Leidenfrost phenomenon: film boiling of liquid droplets on a flat plate. Int. J. Heat Mass Transfer, 9, 1167-1187.

[134] Wikipedia, the free encyclopedia

[135] D. Quere , A. Ajdar, Nat. Mater., 5, 429 (2006).

[136] O. Reynolds, Mem. Proc. Manchester Lit. Phil. Soc. 21, 1-2. (1881).

[137] B. S. Kang, & D. H. Lee, Expts. Fluids 29, 380 (2000).

[138] S. Kamnis and S Gu J. Phys. D: Appl. Phys. 38, 3664 (2005).

[139] S. L. Manzello, & J. C. Yang, Int. J, Heat Mass Transfer 45, 3961(2002).

[140] M. Rein Fluid Dynam. Res. 12, 61 (1993).

[141] A. B. El Bediwi, W. J. Kulnis, Y. Luo, D. Woodland, and W. N. Unertl, Mater. Res. Soc. Symp. Proc. 372, 277 (1995).

[142] E. Adachi, A. S. Dimitro, and K. Nagayama, Langmuir 11, 1057 (1995).

[143] F. Parisse and C. Allain, Langmuir 13, 3598 (1996).

[144] M. Maillard, L. Motte, A. T. Ngo, and M. P. Pileni, J. Phys. Chem. B., 104, 11871 (2000).

[145] C. Stowell and B. A. Korgel, Nano Lett., 1, 595 (2001).

[146] M. Maillard, L. Motte, and L. Pileni, Adv. Mater., 13, 200 (2001).

[147] S. M. rowan, I. M. Newton, G. McHale. J. Phys. Chem., 99,13268 (1999).

[148] J. Fukai, H. Ishizuka, Y. Sakai, M. Kaneda, M. Morita, A. Takahara, International Journal of Heat and Mass Transfer, 49, 3561 (2006).

[149] Y. Lin, H. Skaff, T. Emrick, A. D. Dinsmore, and T. P. Russell, Science, 299, 226 (2003).

[150] L. Pauchard, F. Parisse, and C. Allain . PHYSICAL REVIEW E, 59, 3737 (1999).

[151] T. P. Bigioni et al., Nat. Mater,5, 256 (2006).

[152] E. Rabani, D. Reichman, P. Geissler and E. Brus., Nature 426, 271 (2003).

[153] P. C. Ohara and W. M. Gelbart, Langmuir, 14, 3418 (1998).

[154] M. G Velarde, A. Y Rednikov and Y. S Ryazantsev, J. Phys.: Condens. Matter 8, 9233(1996).

[155] R. G. Picknett; R. J. Bexon, Colloid Interface Sci., 61, 336 (1977).

[156] K. S. Birdi; D. T.Vu, A. Winter,. J. Phys. Chem., 93, 3702 (1989)

[157] M. E. R. Shanahan and C. Bourges,. Int. J. Adhes. Adhes., 14, 201(1994).

[158] C. Bourges and M. E. R. Shanahan , Langmuir, 11, 2820 (1995).

[159] X. Fang, B. Li, J. C. Sokolov, M.H. Rafailovich, D. Gewaily, Appl. Phys. Lett., 87,094103 (2005).

[160] Rowan, S. M.; Newton, M. I.; McHale, G. J. Phys. Chem., 99, 13268 (1995).

[161] Yu, H-Z.; Soolaman, D. M.; Rowe, A. W.; Banks, J. T. ChemPhysChem, 5, 1035 (2004).

[162] CRC Handbook of Chemistry and Physics, A Ready-Reference Book of Chemical and Physical Data, 82nd ed.; Lide, D. R., Ed.; CRC Press LLC: Boca Raton, FL, (2001).

[163] Handbook of Chemical Property Estimation Methods, 1st ed.; Lyman, W. J., Reehl, W. F., Rosenblatt, D. H., Eds.; American Chemical Society: Washington, DC, (1990).

[164] A. J. H. McGaughey and C. A. Ward, J. Appl. Phys.,91,6406 (2002).

[165] Everett, D. H.; Whitton, W. I. Faraday Soc. Trans., 48,749 (1952).

[166] P.G. de Gennes, Rev. Mod. Phys. 57, 827 (1985).

[167] T. Cubaud and M. Fermigier , Europhys. Lett., 55, 239 (2001).

[168] A. W.Neumann, R. J. Good, J. Colloid Interface Sci., 38, 341(1972).

[169] Li, D.; Neumann, A. W. Colloid Polym. Sci., 270, 498 (1992).

[170] Raphael, E.; Joanny, J. F. Europhys. Lett., 21, 483 (1993).

[171] Srinivas R. Ranabothu, Cassandra Karnezis, Lenore L. Dai Journal of Colloid and Interface Science, 288, 213 (2005).

[172] S. Yawahare, K. M. Craig, and A. Scherer, Nano letter 6, 271 (2006).

[173] Jun Xu, Jiangfeng Xia, Suck Won Hong, Zhiqun Lin, Feng Qiu, and Yuliang Yang, Phys. Rev. Lett. 96, 066104(2006).

[174] Adachi et al Langmuir,11,1057(1995).

[175] Y. O. Popov, Phys. Rev. E, 71, 036313 (2005).

[176] S. W. Hong et al.,Chem. Mater., 17,6223 (2005).

[177] A. V. Lyushnin, A. A. Golovin, L. M. Pismen, Phys. ReV. E., 65, 021602 (2002).

[178] G. Reiter, A. Sharma, Phys. ReV. Lett., 87, 166103 (2001).

[179] H. Tavana, A.W. Neumann , Advances in Colloid and Interface Science 132,1, (2007).

[180] A. Vrij, Discuss. Faraday Soc. 42, 23 (1966).

[181] F. Brochard and J. Daillant, Can. J. Phys. 68, 1084 (1990).

[182] S. Herminghaus, et al., Science 282, 916 (1998).

[183] S. Herminghaus et al., Langmuir, 14, 965 (1998).

[184] Ruckenstein, E.; Jain, R. K. Faraday Trans., 70, 132 (1974).

[185] Brochard-Wyart, F.; Daillant, J. Can. J. Phys., 68, 1084 (1990).

[186] O. Karthaus, L. Grasjo, N. Maruyama and M. Shimomura, Chaos 9, 308 (1999).

[187] L.T. Lee, C.A.P. Leite and F. Galembeck, Langmuir 20 (2004), pp. 4430–4435.

[188] J. Huang, F. Kim, A.R. Tao, S. Connor and P. Yang, Nature Mater. 4 (2005), pp. 896–900.

[189] A. M. Cazabat, F. Heslot, S. M. Troian, and P. Carles, Nature , 346, 824 (1990).

[190] G. Reiter, Langmuir 9, 1344 (1993).

[191] A. S. Padmakar, Kajari Kargupta, and Ashutosh Sharma, j,chem..phys., 110,1735 (1999).

[192] Israelachvili, J. N. Intermolecular and Surface Forces; Academic Press: San Diego, CA, (1992).

[193] Derjaguin, B.V. and Churaev, N.V., J. Colloid Interface Sci., 49, 249 (1974).

[194] Derjaguin, B.V. and Churaev, N.V., Croat. Chem. Acta, , 50,187 (1977).

[195] J. Israelashvili, Intermolecular and Surfaces Forces (New York: Academic Press, 1985).

[196] N. Samid-Merzel, S. G. Lipson, and D. S. Tannhauser, Phys. Rev. E 57, 2906 (1998).

[197] U. Thiele, M. Mertig, and W. Pompe, Phys. Rev. Lett. 80, 2869 (1998).

[198] A. Sharma, J. Mittal, R. Verma, Langmuir 18, 10213 (2002).

[199] P. G. de Gennes, F. Brochard- Wyart and D. Qúeré, Capillarity and Wetting Phenomena Drops, Bubbles, Pearls, Waves (New York: Springer-Verlag,2002).

[200] J. G. Leidenfrost, De Aquae Communis Nonnullis Qualitatibus Tractatus (Johann Straube, Duisburg, Germany, (1756).

[201] H. Bouasse, Capillarite´ et Phénomènes Superficiels , Delagrave, Paris, (1924).

[202] B. S. Gottfried, C. J. Lee, and K. J. Bell, Int. J. Heat Mass Transf. 9,1167 (1966).

[203] K. J. Baumeister and F. F. Simon, J. Heat Mass Transf. 95, 166 (1973).

[204] L. H. J. Wachters and N. A. J. Westerling, Chem. Eng. Sci. 21, 1047 (1966).

[205] C. T. Avedisian and M. Fatehi, Int. J. Heat Mass Transf. 31, 1587 (1988).

[206] C. T. Avedisian and J. Koplik,. J. Heat Mass Transf. 30, 379 (1987).

[207] Y. M. Qiao and S. Chandra, Proc. R. Soc. London, Ser. A 453, 673(1997).

[208] K.J. Baumeister, Th. D. Hamill, and G. J. Schoessow, 3rd Int. Heat. Transf. Conf., AIChE, 4, 66 (1966).

[209] Y. A. Buevich and V. N. Mankevich, Dokl. Akad. Nauk SSSR, 262, 1373 (1982).

[210] S. Satcunanathan, J. Mech. Eng. Sci. 10, 438 (1968).

[211] S. Kotake, Trans. Jpn. Soc. Mech. Eng., 287, 1145 (1970)

[212] A. L. Biance, C. Clanet and D. Quère`, Phys. Fluids 15, 1632 (2003).

[213] L. Mahadevan and Y. Pomeau, Phys. Fluids 11, 2449(1999).

[214] H. Linke, B. Aleman, L. Melling, M. Taormina, M. Francis, C. Dow-Hygelund, R.P. Taylor, V. Narayanan, A. Stout: Phys. Rev. Lett. 96, 154502 (2006).

[215] B. M. Patel and J. K. Bell AIChE Symp. Ser. 62, 62 (1966).

[216] B. S. Gottfried and K. J. Bell, I&EC Fundamentals 5, 561 (1966).

[217] B. S. Gottfried, C. J. Lee, and K. J. Bell, Int. J. Heat Mass Transf. 9,1167 (1966).

[218] S. Chandra and S. D. Aziz, J. Heat Transfer 115, 999 (1994).

[219] A. V. Ghule, K. Ghule, C. Y. Chen ,W.Y. Chen, S. H. Tzing, H. Chang, and Y. C. Ling J. Mass Spectrom. 39, 1202 (2004).

[220] X. Su, Z. Zhang, Y. Wang and, M.Zhu, J. Phys. D: Appl. Phys. 38, 3934 (2005).

[221] Z. W. Pan, Z. R. Dai and Z. L. Wang, Science, 291, 1947 (2001).

[222] P. Yang, H. Yan, S. Mao, R. Russo, J. Johnson, R. Saykally, N. Morris, J. Pham, R. He, H. Choi, Adv. Funct. Mater., 12, 323 (2002).

[223] W. I. Park, G. Yi,M. Kim, S. L. Pennycook, Adv. Mater, 14, 1841(2002).

[224] Hong Jin Fan, Peter Werner, and Margit Zacharias, Small, 2, 700 (2006).

[225] L. Vayssieres, Adv. Mater., 15, 464 (2003).

[226] B. Cheng and E. T. Samulski, Chem. Commun.,8, 986, (2004).

[227] L. Vayssieres, Adv. Mater., 15, 464 (2003).

[228] B. Liu, C. Zeng, J. Am. Chem. Soc. 125, 4430 (2003).

[229] P. Si, X. Bian, H. Li, Y. Liu, Mater. Lett. 57, 4079 (2003).

[230] K. Sue, K. Kimura, M. Yamamoto, K. Arai, Mater. Lett. 58, 3350 (2004).

[231] C. Pounder, J. Phys. D: Appl. Phys., 5, (1972).

[232] C. Pounder, J. Electrostatics 1, 395 (1975).

[233] C. Pounder, J. Electrostatics 9, 159 (1980).

[234] C. Pounder, J. Phys. D:A ppl. Phys., 14, 1363 (1981).

[235] J. W.Tester, P. A. Webley, H. R. Holgate, Ind. Eng. Chem. Res., 32, 236 (1993).

[236] T. Heim et al., J. Phys.: Condens Matter, 17, 703 (2005).

[237] Y. Huang, X. Duan, Q. Wei, and C. M. Lieber, Science, 291, 630 (2001).

[238] M. Gleiche, L.F. Chi, H. Fuchs, Nature, 403, 6766 (2000).

[239] X. Chen, M. Hirtz, H. Fuchs and L. Chi, Adv.Mater, 17, 2881(2005).

[240] W. Barthlott and C. Neinhuis, Planta 202, 1 (1997).

[241] D. King, C. Yang, S. Chien, L. Grosshandler, Proc.ASME. (National Heat Transfer Confernce, 1997).

[242] J. Bernardin, I. Mudawar. Journal of Heat Transfer 126, 272 (2004).

[243] Pamplin, B. R. Crystal Growth; Pergamon Press: New York, (1975).

[244] Murray C. B.; Kagan, C. R.; Bawendi, M. G. Annu. Rev. Mater. Sci., 30, 545 (2000).

[245] V. K. Lamer, Ind. Eng. Chem., 44, 1270 (1952).

[246] X. Peng, J. Wickham, A. P. Alivisatos, J. Am. Chem. Soc., 120, 5343 (1998).

[247] Y. Xia, P. Yang, Y. Sun, Y.Wu, B. Mayers, B. Gates, Y. Yin, F. Kim, H. Yan, Adv.Mater. 15, 389 (2003).

[248] H. Huixin and T. Nongjian , Adv. Mater. 2, 161-164 (2002).

[249] U. Kreibig and M. Vollmer, Optical Properties of Metal Clusters (Springer, Berlin, 1995).

[250] H. Raether, Surface Plasmons (Springer, Berlin, 1988).

[251] W. L. Barnes, A. Dereux, and T. W. Ebbesen, Nature, 424, 824 (2003).

[252] Ekmel Ozbay, Science,311,189 (2006).

[253] Rashid Zia, Jon A. Schuller, Anu Chandran, and Mark L. Brongersma. Materialstoday 9 ,20(2006).

[254] H. Ditlbacher, J. R. Krenn, G. Schider, A. Leitner, and F. R. Aussenegg, Appl. Phys. Lett. 81, 1762 (2002).

[255] Y. Sun, Y. Yin, B. Gates, B.T. Mayers and Y. Xia, Nano Lett. 2, 165 (2002).

[256] C.S. Ah, S. D. Hong and D. J. Jang, J. Phys. Chem. B, 103, 3073 (1999).

[257] M. Quinten, A. Leitner, J.R. Krenn, and F.R. Aussenegg, Opt. Lett 23, 1331 (1998).

[258] M.L. Brongersma, J.W. Hartmann, and H.A. Atwater, Phys. Rev. B. 62, R16356 (2000).

[259] R. Elghanian, J.J. Storhoff,R . C. Mucic, R .L. Letsinger,and C. A. Mirkin," Science 277, 1078 (1997).

[260] J. Tominaga,C. Mihalcea, D. B¨uchel, H . Fukuda, T. Nakano,N . Atoda, H. Fuji, and T. Kikukawa, Appl.Phys. Lett. 78, 2417 (2001).

[261] S. Nie and S. R. Emory, Science 275, 1102 (1997).

[262] A. Kolmakov, Y. Zhang, G. Chang and M. Moskovits, Adv. Matter., 15,997 (2003).

[263] F. Patolsky and C. M. Lieber, Materials Today, 8 (2005).

[264] T. Hassenkam, K. Moth-Poulsen, N. Stuhr-Hansen, K. Nørgaard, M. S. Kabir, and T. Bjørnholm, Nano Lett. 4, 19 (2004).

[265] F. Favier, E. C. Walter, M. P. Zach, T. Benter, R. M. Penner, Science 293, 2227 (2001).

[266] A. Kolmakov, M. Moskovits, ANNUAL REVIEW OF MATERIALS RESEARCH, 34, 151, (2004).

[267] Q. Wan; Q. H. Li; Y. J. Chen; T. H. Wang; X. L. He; J. P. Li, Appl. Phys. Lett.,84 ,3654 (2004).

[268] B.J. Murray, E.C. Walter, and R.M. Penner, Nano Let., 4, 665 (2004).

[269] D. C. Reynolds; D. C. Look; B. Jogai; C. W. Litton; T. C. Collins; W. Harsch, G. Cantwell, Phys. Rev.B, 57, 12151 (1998).

[270] K. Thonke; T. Gruber; N. Teo_lov; R. Schonfelder; A. Waag; R. Sauer, Physica B, 308, 945 (2001).

[271] P. Yang; H. Yan; S. Mao; R. Russo; J. Johnson; R. J. Saykally; N. Morris; J. Pham;R. He; H. Choi, Adv. Funct. Mater.,12 , 323 (2002).

[272] A. Sekar; S. H. Kim; A. Umar; Y.-B. Hahn, Journal of Crystal Growth, 277, 471 (2005).

[273] Z. X. Zeng; Y. Y. Xi; P. Dong; H. G. Huang; J. Z. Zhou; L. L. Wu; Z. H. Lin, Phys. Chem. Comm.,9 , 63 (2002).

[274] W. I. Park; Y. H. Jun; S. W. Jung; G. C. Yi, Appl. Phys. Lett.,82 , 964 (2003).

[275] X. T. Zand; Y. C. Liu; L. G. Zang; J. Y. Zang; Y. M. Lu; D. Z. Shen; W. Xu;

G. Z. Zong; X. W. Fgan; X. G. Kong, J. Appl. Phys.,92 , 3293 (2002).

[276] J. H. Choy; E. S. Jang; J. H. Won; J. H. Chung; J. Jang; Y. W. Kim, Adv. Mater.,15 , 1911 (2003).

[277] S. H. Jo; D. Banerjee; Z. F. Ren, Appl. Phys. Lett,85 , 1407 (2004).

[278] S. Y. Li; P. Lin; C. Y. Lee; T. Y. Tseng, Appl. Phys. Lett.,84 , 1540 (2004).

[279] Y. K. Tseng; C. J. Huang; H. M. Cheng; I. N. Lin; K. S. Liu; I. C. Chen, Adv. Funct. Mat.,13, 811 (2003).

[280] The Material Science of Thin Films, M. Ohring; Academic Press, New York (1992).

[281] Thin Film Deposition Principles and Practice, ed. D.L. Smith; McGraw Hill, New York (1995).

Acknowledgment

My deep gratitude is to each person who contributed through his support, experience and friendship to this work.

In particular, I would like to thank**,** Prof. Rainer Adelung and Prof. Franz Faupel for giving me the opportunity to work on a new "nano" field, allowing me to perform an interesting research "Fracture Approach", encouraging my own research "Drop Approach". Furthermore, ***I am very thankful*** for their affiance, solidarity and support which I will never ever forget.

Hearty thanks, to all "former" students who did their master thesis with me;

M.Sc. Shiva Kumar Rudra , M.Sc. Said Jebril, M.Sc. Dadichi Paritker, M.Sc., Huang rui, and

M.Sc. Khaled Hirmas for the nice time, jokes, and hard working.

Many thanks, to my office mates; Dipl.-Phys. Tomislav, M.Sc. Muhammad Qasim Shaikh and "fresh" Dr. Michael Scharnberg for terrific silent atmosphere "basket ball" in the office. Especial, hearty thank to Dr. Abijit Biswas, the one who introduce me to the optical properties of nanomaterials.

Many thanks, to my colleagues ; Dr. Rainer Kunz, Dipl.-Ing.; Henrye Greve, M. Sc. Haile Takele, Dr. Ulrich Schürmann, Dr. Jörn Kanzow, Dipl.-Ing. Alexander Bartsch, Dipl.-Ing. Christian Pochstein, M. Sc. Amit Kulkarni, for their help, friendship and relaxing times, with especial thank to Dipl.-Ing Jan Kruse and M. Sc Venkata Sai Kiran for their support by sketch drawing and to our secretary stuff; Beata Minten and Christiane Otte-Hüls

I would like to thank, Dr. Klaus Rätzke Dr. Vladimir Zaporojtchenko and Dr. Thomas Strunskus for the fruitful discussions and their continuous support. Particular thanks to Dr. Strunskus for reading the manuscript, and Dr. Rätzke for helping by word.

Hearty thanks, to my smoke mate Dipl.-Ing. Stefan Rehders for his friendship, support and the help by all technical problem contributions to the researches. Dipl.-Ing. Rainer Kloth for fast computer problem solving.

Special thanks, to Dr. Dirk Lukas (PVA) for his scientifically discussion my Patents and his friendship and cooperation.

Hearty thanks, to Sam Buschhorn for checking the English of my thesis.

My wife and my Bilal "***love you***" and

My deep love and gratitude is given to my family and folk in Palestine.